Alfred-Wegener-Institut

Helmholtz-Zentrum für Polar- und Meeresforschung

Forschungsstelle Potsdam

Towards seasonal prediction: Stratosphere-troposphere coupling in the atmospheric model ICON-NWP

Dissertation

zur Erlangung des akademischen Grades

„doctor rerum naturalium“ (Dr. rer. nat.)

in der Wissenschaftsdisziplin „Klimaphysik“

eingereicht an der Mathematisch-Naturwissenschaftlichen Fakultät

der Universität Potsdam

von Raphael H. Köhler

Potsdam, den 19. August 2020

Raphael H. Köhler
Towards seasonal prediction: Stratosphere-troposphere coupling in the atmospheric model ICON-NWP
Dissertation, December 18, 2020
Gutachter: Prof. Dr. Markus Rex, Prof. Dr. Stefan Brönnimann and Prof. Dr. Klaus Dethloff
Betreuer/innen: Prof. Dr. Markus Rex, apl. Prof. Dr. Frank Spahn and Dr. Dörthe Handorf

Published online on the
Publication Server of the University of Potsdam:
https://doi.org/10.25932/publishup-48723
https://nbn-resolving.org/urn:nbn:de:kobv:517-opus4-487231

Abstract

Stratospheric variability is one of the main potential sources for sub-seasonal to seasonal predictability in mid-latitudes in winter. Stratospheric pathways play an important role for long-range teleconnections between tropical phenomena, such as the quasi-biennial oscillation (QBO) and El Niño-Southern Oscillation (ENSO), and the mid-latitudes on the one hand, and linkages between Arctic climate change and the mid-latitudes on the other hand. In order to move forward in the field of extratropical seasonal predictions, it is essential that an atmospheric model is able to realistically simulate the stratospheric circulation and variability. The numerical weather prediction (NWP) configuration of the ICOsahedral Non-hydrostatic atmosphere model ICON is currently being used by the German Meteorological Service for the regular weather forecast, and is intended to produce seasonal predictions in future. This thesis represents the first extensive evaluation of Northern Hemisphere stratospheric winter circulation in ICON-NWP by analysing a large set of seasonal ensemble experiments.

An ICON control climatology simulated with a default setup is able to reproduce the basic behaviour of the stratospheric polar vortex. However, stratospheric westerlies are significantly too weak and major stratospheric warmings too frequent, especially in January. The weak stratospheric polar vortex in ICON is furthermore connected to a mean sea level pressure (MSLP) bias pattern resembling the negative phase of the Arctic Oscillation (AO). Since a good representation of the drag exerted by gravity waves is crucial for a realistic simulation of the stratosphere, three sensitivity experiments with reduced gravity wave drag are performed. Both a reduction of the non-orographic and orographic gravity wave drag respectively, lead to a strengthening of the stratospheric vortex and thus a bias reduction in winter, in particular in January. However, the effect of the non-orographic gravity wave drag on the stratosphere is stronger. A third experiment, combining a reduced orographic and non-orographic drag, exhibits the largest stratospheric bias reductions. The analysis of stratosphere-troposphere coupling based on an index of the Northern Annular Mode demonstrates that ICON realistically represents downward coupling. This coupling is intensified and more realistic in experiments with a reduced gravity wave drag, in particular with reduced non-orographic drag. Tropospheric circulation is also affected by the reduced gravity wave drag, especially in January, when the strongly improved stratospheric circulation reduces biases in the MSLP patterns. Moreover, a retuning of the subgrid-scale orography parameterisations leads to a significant error reduction in the MSLP in all months. In conclusion, the combination of these adjusted parameterisations is recommended as a current optimal setup for seasonal simulations with ICON.

Additionally, this thesis discusses further possible influences on the stratospheric polar vortex, including the influence of tropical phenomena, such as QBO and ENSO, as well as

the influence of a rapidly warming Arctic. ICON does not simulate the quasi-oscillatory behaviour of the QBO and favours weak easterlies in the tropical stratosphere. A comparison with a reanalysis composite of the easterly QBO phase reveals, that the shift towards the easterly QBO in ICON further weakens the stratospheric polar vortex. On the other hand, the stratospheric reaction to ENSO events in ICON is realistic. ICON and the reanalysis exhibit a weakened stratospheric vortex in warm ENSO years. Furthermore, in particular in winter, warm ENSO events favour the negative phase of the Arctic Oscillation, whereas cold events favour the positive phase. The ICON simulations also suggest a significant effect of ENSO on the Atlantic-European sector in late winter. To investigate the influence of Arctic climate change on mid-latitude circulation changes, two differing approaches with transient and fixed sea ice conditions are chosen. Neither ICON approach exhibits the mid-latitude tropospheric negative Arctic Oscillation circulation response to amplified Arctic warming, as it is discussed on the basis of observational evidence. Nevertheless, adding a new model to the current and active discussion on Arctic-midlatitude linkages, further contributes to the understanding of divergent conclusions between model and observational studies.

Kurzfassung

Die stratosphärische Variabilität ist eine der wichtigsten potentiellen Quellen für die Vorhersagbarkeit der atmosphärischen Zirkulation in den mittleren Breiten im Winter auf der Zeitskala von Wochen bis zu Jahreszeiten. Stratosphärische Prozesse spielen eine grundlegende Rolle für die Fernverbindungen (Telekonnektionen) zwischen tropischen Klimaphänomenen, wie der quasi-zweijährigen Schwingung (QBO) oder „El Niño-Südliche Oszillation“ (ENSO), und den mittleren Breiten, sowie den Telekonnektionen zwischen arktischen Klimaänderungen und der atmosphärischen Zirkulation in den mittleren Breiten. Die Fähigkeit eines atmosphärischen Modells, die stratosphärische Zirkulation und deren Variabilität realistisch zu simulieren, ist deshalb von grundlegender Bedeutung, um die Jahreszeitenvorhersage in den mittleren Breiten deutlich zu verbessern. Das nichthydrostatische Atmosphärenmodell ICON (ICOsahedral Non-hydrostatic atmosphere model) wird gegenwärtig beim Deutschen Wetterdienst (DWD) in der numerischen Wettervorhersagekonfiguration (ICON-NWP) für die Wettervorhersage genutzt, und soll zukünftig auch für Jahreszeitenvorhersagen benutzt werden. Darauf basierend, präsentiert die vorliegende Arbeit eine Vielzahl von saisonalen Ensembleexperimenten mit ICON-NWP und liefert damit die erste umfassende Bewertung der stratosphärischen Winterzirkulation der nördlichen Hemisphäre in ICON-NWP.

Die Klimatologie eines ICON-Modelllaufs im Standardsetup reproduziert die grundlegenden Eigenschaften des stratosphärischen Polarwirbels. Allerdings sind die stratosphärischen Westwinde deutlich schwächer als in den Beobachtungen, und starke Stratosphärenerwärmungen treten insbesondere im Januar zu häufig auf. Zudem ist der schwache stratosphärische Polarwirbel in ICON mit einem typischen Fehler-Muster des Bodenluftdrucks verknüpft,

welches der negativen Phase der Arktischen Oszillation (AO) ähnelt. Da eine gute Darstellung des von Schwerewellen ausgeübten Widerstands für eine realistische Simulation der Stratosphäre entscheidend ist, werden drei Sensitivitätsexperimente mit reduziertem Schwerewellenwiderstand durchgeführt. Sowohl eine Verringerung des nicht-orographischen, als auch eine Verringerung des orographischen Schwerewellenwiderstands führen jeweils zu einer Verstärkung des stratosphärischen Wirbels und damit zu einer Verringerung des Fehlers im Winter, insbesondere im Januar. Die Wirkung des nicht-orographischen Schwerewellenwiderstands auf die Stratosphäre ist hierbei jedoch stärker. Ein drittes Experiment, welches den reduzierten orographischen und nicht-orographischen Widerstand kombiniert, zeigt die größten Verbesserungen in der Stratosphäre. Die auf dem Index des „Northern Annular Mode“ basierende Analyse der Stratosphären-Troposphären-Kopplung zeigt, dass ICON die nach unten gerichtete Kopplung zwischen der Stratosphäre und Troposphäre realistisch darstellt. Diese Kopplung wird in Experimenten mit einem reduzierten Schwerewellenwiderstand verstärkt und realistischer dargestellt, dies gilt insbesondere für den reduzierten nicht-orographischen Widerstand. Auch die troposphärische Zirkulation wird durch den reduzierten Schwerewellenwiderstand beeinflusst, vor allem im Januar, wenn die stark verbesserte stratosphärische Zirkulation den Fehler in den Bodenluftdruckfeldern reduziert. Darüber hinaus führt ein Tuning der Parameterisierung der subgrid-skaligen orographischen Schwerewellen zu einer signifikanten Fehlerreduktion des Bodenluftdrucks in allen Monaten. Die Kombination all dieser angepassten Parametrisierungen wird als derzeit optimales Setup für Jahreszeiten-Simulationen mit ICON vorgeschlagen.

Darüber hinaus werden in dieser Arbeit weitere mögliche Einflussfaktoren auf den stratosphärischen Polarwirbel diskutiert, darunter der Einfluss tropischer Phänomene, wie QBO und ENSO, sowie der Einfluss einer sich rasch erwärmenden Arktis. Das quasi-oszillierende Verhalten der QBO wird durch ICON nicht simuliert, sodass schwache Ostwinde in der tropischen Stratosphäre dominieren. Ein Vergleich mit einem Reanalyse-Komposit der östlichen QBO-Phase zeigt, dass die Verschiebung in Richtung der östlichen QBO in ICON den stratosphärischen Polarwirbel weiter abschwächt. Die stratosphärische Reaktion auf ENSO-Ereignisse in ICON ist jedoch realistisch. ICON und Reanalysedaten zeigen einen abgeschwächten Stratosphärenwirbel in warmen ENSO-Jahren. Darüber hinaus begünstigen insbesondere im Winter warme ENSO-Ereignisse die negative Phase der Arktischen Oszillation, während kalte Ereignisse die positive Phase begünstigen. Die ICON-Simulationen deuten auch auf einen signifikanten Effekt von ENSO auf den atlantisch-europäischen Sektor im Spätwinter hin. Um den Einfluss des arktischen Klimawandels auf Änderungen der Zirkulation in mittleren Breiten zu untersuchen, werden zwei unterschiedliche Ansätze mit transienten und festen Meereisgrenzen gewählt. Keiner der beiden ICON-Ansätze zeigt eine Tendenz zur negativen Phase der Arktische Oszillation als Reaktion auf die verstärkte Erwärmung der Arktis, wie sie in der Literatur anhand von Beobachtungsdaten häufig diskutiert wird. Jedoch wird somit der aktuellen und aktiven Diskussion zu den Auswirkungen des arktischen Klimawandels auf die Zirkulation der mittleren Breiten ein neues Modell hinzugefügt.

Contents

1 Introduction

1.1 Motivation: Seasonal prediction

One of the largest achievements of atmospheric sciences has been the development of numerical models to predict and understand atmospheric processes. Since Bjerknes (1904) developed one of the first scientific approaches of a mathematical model of atmospheric dynamics, the development of sophisticated atmosphere and earth-system models proceeded with the progress in high performance computing during the past decades. This progress led to a strong decrease of prediction errors in atmospheric dynamics. The idealized idea of weather and climate models is based on the differentiation of the types of predictability: on the one hand there is the predictability dependent on the initial values, and on the other predictability dependent on the boundary forcing (World Meteorological Organization, 1975). Weather prediction is a classic example of the first type, as the prediction quality is highly dependent on the quality of the initial data. Errors in the initial state will grow in time until the prediction is no better than a sophisticated guess (Lorenz, 1975). Based on the uncertainty of the initial state, modern weather predictions use a large ensemble approach to give an indication of the range of possible future states of the atmosphere. Useful forecasts now reach up to 10 days into the future (Bauer et al., 2015). Climate forecasts, however, are less dependent on the initial state, as the influence of the forcing on the mean state will outweigh memory of the initial state. Thus, climate forecast spreads are mainly caused by uncertainties in the boundary data and difficulties in separating internal variability from the actual signals. Both, weather predictions and climate forecasts furthermore suffer from inaccuracies in the physical parameterisation packages and numerical schemes of the models themselves (Palmer et al., 2005).

Whereas the time scale of weather predictions lies within multiple days, the time scale of climate forecasts covers multiple years. In between there is a large gap: sub-seasonal to seasonal predictions with time scales from multiple weeks to months. Seasonal prediction combines a large accumulation of initial errors with the uncertainties in feedback processes that also play a crucial role in constraining climate forecasts (Palmer and Anderson, 1994; Doblas-Reyes et al., 2013). Therefore, progress in the field of seasonal prediction is slow and it relies mainly on the memory effects of different climate processes. Most atmospheric models used for seasonal predictions make use of the lower boundary forcing, which evolves on a slower time scale than the synoptic patterns. Common examples are ocean temperatures, soil moisture, snow cover or sea ice concentration. Therefore, the development of coupled general circulation models (CGCMs) has been proved to be highly beneficial for the seasonal prediction. By simulating coupled feedbacks between the atmosphere, ocean, land and

cryosphere, these models can make use of the different response time scales to increase seasonal predictability. This particularly accounts for the Tropics, where the internal chaotic variability is smaller and memory processes can dominate the seasonal weather patterns (Palmer and Anderson, 1994). A prominent example for the success of seasonal predictions in low latitudes is El Niño-Southern Oscillation (ENSO), an irregularly periodic variation in winds and sea surface temperatures (SSTs) over the tropical Pacific. Already in the nineties, statistical as well as coupled atmosphere-ocean models outperformed persistence in predicting typical indices of ENSO on lead times of 6 to 12 month (Latif et al., 1998). A strong observational network and more advanced coupled models helped to boost the skill of seasonal ENSO predictions and made it the most predictable climate mode (Tang et al., 2018). Furthermore, the tropical Pacific phenomenon ENSO is connected to multiple regions around the world via so called teleconnections (e.g. Trenberth and Shea, 1987; Mann and Park, 1994; Enfield and Mestas-Nuñez, 1999; Mann et al., 2000). The good prediction quality of the tropical Pacific phenomenon therefore positively affects model predictions outside the Tropics. Brands (2017) showed that in particular the teleconnection patterns in the tropics and the Pacific area are robust, whereas the teleconnections in the extratropics are not. However, there is strong evidence that the stratospheric polar vortex is influenced by ENSO (e.g. Camp and Tung, 2007; Garfinkel and Hartmann, 2007; Free and Seidel, 2009; Manzini, 2009).

Seasonal prediction for mid and high latitudes is less straight forward, as the internal chaotic variability is large and synoptic weather patterns vary on short time scales. Whereas North America benefits from seasonal predictability arising from ENSO teleconnections, there are less predictors for Europe (Doblas-Reyes, 2010). Besides predictability arising from the lower boundaries, such as soil humidity, snow cover or SSTs, the stratosphere is one of the main potential sources for sub-seasonal to seasonal predictability in mid-latitudes (Butler et al., 2019), especially in late winter. This potential is based on the interactions between planetary and synoptic scales on time scales of some days to multiple weeks. Baldwin and Dunkerton (1999; 2001) demonstrated that stratospheric geopotential anomalies can propagate into to the troposphere with a lag of up to 60 days. The downward coupling is especially strong for weak vortex events during major stratospheric warmings (MSWs). Already the knowledge of such an event can help to improve sub-seasonal to seasonal predictability. An accurate prediction of such anomalous stratospheric vortex events, could help to improve seasonal predictability in mid-latitudes on time scales greater than 60 days (Domeisen et al., 2015). Consequently, accurate predictions of stratospheric variability and improved understanding of stratosphere-troposphere coupling would be highly beneficial for seasonal prediction in mid-latitudes. Furthermore, errors in stratospheric simulations can feed into the stratosphere and cause errors in the simulation of tropospheric dynamics. Models often struggle to capture variability and strength of the highly variable stratospheric polar vortex. Therefore, the evaluation and improvement of stratospheric model behaviour is essential to achieve further progress in the field of seasonal predictability in mid-latitudes.

A further potential predictor for mid-latitude weather patterns is Arctic sea ice. Arctic sea ice loss is strongly connected to the recent rapid warming of the Arctic troposphere (Screen and Simmonds, 2010). This near-surface Arctic warming is happening at approximately

double the pace compared to lower latitudes, a phenomenon named Arctic amplification (e.g. Serreze et al., 2009; Alexeev et al., 2012; Cowtan and Way, 2014). Different studies argue that the Arctic amplification leads to a wavier jet stream, resulting in an increase of extreme weather situations and even cold spells in winter (e.g. Francis and Vavrus, 2012; Cohen et al., 2014; Romanowsky et al., 2019). A dynamical stratospheric pathway plays a major role in connecting the Arctic amplification to changes in mid-latitude weather and climate via troposphere-stratosphere coupling (Kim et al., 2014; Nakamura et al., 2016; Jaiser et al., 2016). The physical background for this linkage will be discussed in Section 2.3.3. Yet, there is an active discussion on how strong this linkage is compared to the internal variability of the climate system, and the community argues for more coordinated modelling studies to better understand the climate response to Arctic climate change (Overland et al., 2016; Cohen et al., 2020).

1.2 The new atmosphere model ICON

This work is based on seasonal experiments with the ICOsahedral Non-hydrostatic atmosphere model ICON. The model has been developed jointly by the German Weather Service (DWD) and the Max Planck Institute for Meteorology (MPI-M), and is the central piece of the new unified model approach in Germany (Bonaventura, 2004; Zängl et al., 2015). ICON provides, inter alia, local mass conservation, a flexible grid nesting option and a non-hydrostatic dynamical core formulated on an a icosahedral grid. It currently exists in two main configurations: one for numerical weather predictions by DWD (hereafter ICON-NWP), which has been operational since 2015, and one for climate simulations by MPI-M (ICON-A). Both configurations share the same dynamical core, but differ in their physical packages. The dynamical core has been tested (Zängl et al., 2015), the ICON-NWP forecasts are constantly verified by DWD and ICON-A has been described (Giorgetta et al., 2018) and evaluated (Crueger et al., 2018), but there is no extensive study on the evaluation of Northern Hemisphere (NH) stratospheric winter circulation in ICON. There is some evidence that the stratospheric westerlies in winter are underestimated in ICON-A (Crueger et al., 2018; Borchert et al., 2019). In addition, ICON-NWP is currently mainly used for numerical weather prediction with time scales of up to 14 days. Therefore, running seasonal experiments with ICON-NWP and evaluating the performance is of great importance for planned future seasonal applications of ICON-NWP. A short model description of ICON is given in Section 3.1.

1.3 Research questions

Based on these scientific needs, this thesis addresses four main research questions (RQs), which are presented in a consecutive order, but can also be assessed individually. The

common ground for all RQs is the overarching long term goal of improved seasonal predictability by an improved understanding of stratosphere-troposphere coupling. Therefore, RQ1 assesses the current ICON setup, RQ2 deals with improving this ICON setup, RQ3 and RQ4 investigate further mechanisms that can strongly influence the NH circulation on seasonal time scales, i.e. the quasi-biennial oscillation, ENSO and Arctic amplification. The focus of this thesis is on the stratospheric circulation of the Northern Hemisphere only, as studies see potential for improved seasonal predictions based on an accurate simulation of the highly variable northern polar vortex (Domeisen et al., 2020). The motivation for each RQ will shortly be discussed in the following. Before the results based on the four RQs will be assessed and discussed in the Chapters 4 and 5, the theoretical background is given in Chapter 2. Furthermore, the atmosphere model ICON, the reanalysis data and the applied methods are described in Chapter 3.

RQ1 Is ICON able to simulate the stratospheric vortex realistically?

Due to the fact that the stratospheric polar vortex of the Northern Hemisphere is highly variable in winter, models often struggle to capture its variability and strength (Butchart et al., 2011; Charlton-Perez et al., 2013; Seviour et al., 2016). Yet the strong influence of the stratosphere on tropospheric circulation on seasonal time scales could play a crucial role in the progress of seasonal predictability in mid-latitudes. Thus, for seasonal experiments it is very important that stratospheric dynamics and variability are simulated realistically. As ICON-NWP is not commonly used for seasonal simulations, the first research question is, if ICON is actually able to realistically simulate the stratospheric polar vortex. Therefore, in Section 4.1.2 seasonal ICON experiments with a default setup are analysed.

RQ2 What is the influence of the gravity wave drag parameterisations in ICON?

The strength and variability of the stratospheric polar vortex are determined by the nonlinear interactions of the vortex with the total amount of horizontal momentum transported vertically from the troposphere. This momentum is transported to the stratosphere by large-scale Rossby waves and meso-scale gravity waves. Due to their scale, gravity waves are not resolved and therefore parameterised in ICON. However, these parameterisations are connected to a large amount of uncertainty and are potentially resolution dependent (Fritts and Alexander, 2003). The gravity wave drag parameterisations can be used to fine-tune stratospheric behaviour (e.g. Polichtchouk et al., 2018b). Section 4.2 focuses on the influence of the gravity wave drag in ICON and how the stratospheric circulation can be improved by adjusting these parameterisations. The physical background on gravity waves is given in Section 2.2.2. The results of Section 4.2 are strongly based on the paper "Improved Stratospheric Circulation Due to Changes in the Gravity Wave Drag Parameterisations in ICON-NWP" by Köhler et al., which is currently under review at the Journal of Advances in Modeling Earth Systems (JAMES).

RQ3 How do tropical phenomena influence the stratospheric vortex?

Besides gravity waves vertically propagating into the stratosphere and thus influencing the polar vortex, also tropical phenomena play a large role in modulating the stratospheric polar vortex. This especially accounts for ENSO and the quasi-biennial oscillation (QBO), which have been proved to influence the stratospheric polar vortex by modulating the propagation of planetary waves (e.g. Holton and Tan, 1980; Labitzke, 1987; Camp and Tung, 2007; Garfinkel and Hartmann, 2007; Free and Seidel, 2009; Manzini, 2009; Anstey and Shepherd, 2014). Consequently, an analysis of stratospheric polar vortex dynamics and variability without assessing the influence from tropical phenomena is incomplete and can induce biases in the simulation of the polar vortex itself. Furthermore different studies have shown, that the tropical phenomena ENSO and QBO can play a role in improving extratropical predictive skill on seasonal time scales (e.g. Brönnimann, 2007; Boer and Hamilton, 2008; Ineson and Scaife, 2009). The influence of these phenomena on the stratospheric circulation in ICON is discussed in Section 4.3.

RQ4 Does ICON show a stratospheric pathway for Arctic-midlatitude linkages?

Arctic-midlatitude linkages are still a complex and controversial topic connected to a considerable amount of uncertainty (Overland et al., 2015). While there is some observational evidence for a stratospheric pathway linking Arctic amplification to mid-latitude weather changes, model studies exhibit more ambiguous results (Cohen et al., 2020). With the goal of reducing some of the uncertainties obscuring the impacts of a rapidly warming and melting Arctic on weather patterns in mid-latitudes, the community urges for more coordinated observational and model studies (e.g. Overland et al., 2015; Francis, 2017). Therefore, in Section 4.4 it is investigated whether ICON shows a stratospheric pathway for Arctic-midlatitude linkages and how it is influenced by the gravity wave drag.

2 Theoretical background

2.1 Fundamentals of atmospheric circulation

The Earth's climate is governed by a complex interplay of its four main spheres, namely the lithosphere, biosphere, hydrosphere and the atmosphere. As part of the hydrosphere, the cryosphere plays a crucial role in high latitudes and glacial areas. This thesis mainly focuses on the atmosphere, which is the gaseous layer surrounding the Earth. Furthermore this work will focus on the influence of the hydrosphere on the atmosphere, in particular the influence of the Pacific Ocean (RQ3) and of Arctic sea ice (RQ4). The upper lithosphere and the biosphere are part of the model simulations in this thesis, but are not investigated explicitly. Before the experimental setup, data and methods are explained in Chapter 3, this section lays the physical foundation of atmospheric circulation.

2.1.1 Primitive equations

The atmospheric circulation can be described by the fluid and thermodynamic primitive equations. Besides the atmosphere, these equations are applicable for the ocean and are comprised of five coupled equations that are based on the conservation of momentum, mass and energy. For an atmosphere containing humidity, the set of equations is extended by the tracer transport for water vapour. The choice of the coordinate system is dependent on the application of the equations. The Cartesian system is useful for theoretical considerations, whereas the spherical system is used for numerical predictions. The three momentum equations are most conveniently represented in vector form in Cartesian coordinates:

$$\frac{D\mathbf{v}}{Dt} = \underbrace{-2\boldsymbol{\Omega}\times\mathbf{v}}_{i} \underbrace{-\frac{1}{\rho}\boldsymbol{\nabla}p}_{ii} + \underbrace{\mathbf{g}}_{iii} + \underbrace{\mathbf{F}_r}_{iv}, \tag{2.1}$$

where $\mathbf{v}$ is the three dimensional velocity, $\boldsymbol{\Omega}$ is the angular velocity of the Earth, ρ is the density, p is pressure, $\mathbf{g}$ is the gravitational acceleration and $\mathbf{F}_r$ is the frictional force. Equation 2.1 states that the acceleration following the relative motion in the rotating frame equals the sum of the Coriolis force (i), the pressure gradient force (ii), the effective gravity (iii) and friction (iv). The total derivative is given by the Euler operator:

$$\frac{D}{Dt} = \frac{\partial}{\partial t} + u\frac{\partial}{\partial x} + v\frac{\partial}{\partial y} + w\frac{\partial}{\partial z} = \frac{\partial}{\partial t} + \mathbf{v}\cdot\boldsymbol{\nabla}. \tag{2.2}$$

The equation of continuity is derived from the conservation of mass. It equates the increase in mass in a hypothetical fluid volume with the net flow of mass into the volume. Here, it is presented in the mass divergence form using the partial derivative:

$$\frac{\partial \rho}{\partial t} + \boldsymbol{\nabla} \cdot (\rho \mathbf{v}) = 0. \tag{2.3}$$

In order to incorporate the thermal energy into the equation system, it is made use of the first law of thermodynamics (conservation of energy):

$$c_p \frac{DT}{Dt} - \frac{1}{\rho} \frac{Dp}{Dt} = \dot{Q}, \tag{2.4}$$

where c_p is the specific heat at constant pressure, T is the temperature and $\dot{Q}$ is the diabatic heating rate. Equation 2.4 is a simple form of a prognostic equation relating to the rate of change of temperature of an air parcel moving through the atmosphere. The second term on the left represents a conversion between thermal and mechanical energy, thereby enabling the solar heat energy to drive the motions of the atmosphere.

Associated with the five primitive equations (2.1, 2.3 and 2.4) are five unknown variables: the components of **v**, p and T. Furthermore, ρ is also considered to be unknown, but is related to p and T via the equation of state for an ideal gas:

$$p = \rho R T, \tag{2.5}$$

with the gas constant for dry air $R = 287 Jkg^{-1}K^{-1}$. The ideal gas equation relates temperature, pressure and density of a system in thermodynamic equilibrium and is necessary for the closure of the equation system.

The rotational components of the velocity field can be described with the help of the relative vorticity $\zeta = \nabla \times \mathbf{v}$. The distribution of the relative vorticity is used as a diagnostic for weather analysis, as regions of positive ζ are associated with cyclonic storms in the Northern Hemisphere. By adding the planetary vorticity f to the relative vorticity and thus accounting for planetary rotation, the absolute vorticity $\eta = \zeta + f$ is obtained. The potential vorticity PV describes the ratio of the absolute vorticity of the air parcel to the depth of the vortex. PV must be conserved following the motion in adiabatic, frictionless flow. It is given as

$$PV = \frac{1}{\rho} \eta \nabla \theta, \tag{2.6}$$

where θ is the potential Temperature, which describes the temperature a sample of air would have if it were compressed adiabatically to standard pressure p_0. It is defined as

$$\theta = T(\frac{p_0}{p})^{\frac{R}{c_p}}, \tag{2.7}$$

where $c_p = 1004 Jkg^{-1}K^{-1}$ is the specific heat capacity at a constant pressure.

2.1.2 The global energy budget

The global energy budget of the Earth is controlled by solar radiation. Over long time scales, the Earth's atmosphere is in thermal equilibrium. Thus, the net energy gained from the sun must also vanish. The basis for thermal emission is described by Planck's law. To maintain the thermal equilibrium, a blackbody that absorbs radiant energy must also emit it. Planck derived a relationship between the spectrum of emitted intensity B_λ and the body's temperature T:

$$B_\lambda(T) = \frac{2hc^2}{\lambda^5(e^{\frac{hc}{K\lambda T}} - 1)}, \tag{2.8}$$

with the wavelength λ, the Planck constant h, the speed of light c and the Boltzmann constant K. The derivative of equation 2.8 by λ delivers Wien's displacement law, which gives the wavelength of maximum intensity λ_m:

$$\lambda_m = \frac{2897}{T}(\mu m). \tag{2.9}$$

Furthermore, the Stefan-Boltzmann law states, that the total flux emitted by a blackbody is proportional to its temperature:

$$E = \sigma T^4, \tag{2.10}$$

where E is the irradiance and σ is the Stefan-Boltzmann constant. From equations (2.9) and (2.10) it is clear, that the higher the temperature of a body, the more energy is emitted, including a shift of its emission spectrum to shorter wavelengths. With an approximate average temperature of 6000 K for the Sun and 288 K for the Earth, the wavelengths of maximum intensity of emission differ largely: solar shortwave radiation with a maximum at 0.48 μm and the Earth's longwave radiation with a maximum at 10 μm. This difference in the maximum wavelengths is crucial for the understanding of Earth's energy balance. Based on equation 2.10, the blackbody temperature of the Earth is given by:

$$T = \left(\frac{(1-A)S_0}{4\sigma}\right)^{\frac{1}{4}}, \tag{2.11}$$

with the incoming solar flux density S_0 and the albedo A. With an estimated flux density of $S_0 = 1361$ Wm^{-2} (Kopp and Lean, 2011) and an albedo of $A = 0.29$ (Stephens et al., 2015), the equivalent blackbody temperature of the Earth is 255 K. This is more than 30 K cooler than the actual measured global mean surface temperature of 288 K. This discrepancy originates from the different ways the atmosphere processes shortwave and longwave radiation. Whereas the atmosphere is nearly transparent for shortwave radiation from the sun, it is rather opaque to the longwave radiation from the Earth. By absorbing and thereby "trapping" parts of the longwave radiation, the atmosphere has a strong warming effect. This is known as the greenhouse effect, which is controlled by the longwave opacity of atmospheric constituents. Besides the primary absorber water vapour, also carbon dioxide, ozone, nitrous oxide, aerosols and halo carbons are radiatively active at wavelengths of longwave radiation. Thus, an increase of carbon dioxide triggers atmospheric warming, and is a large contributor to global warming.

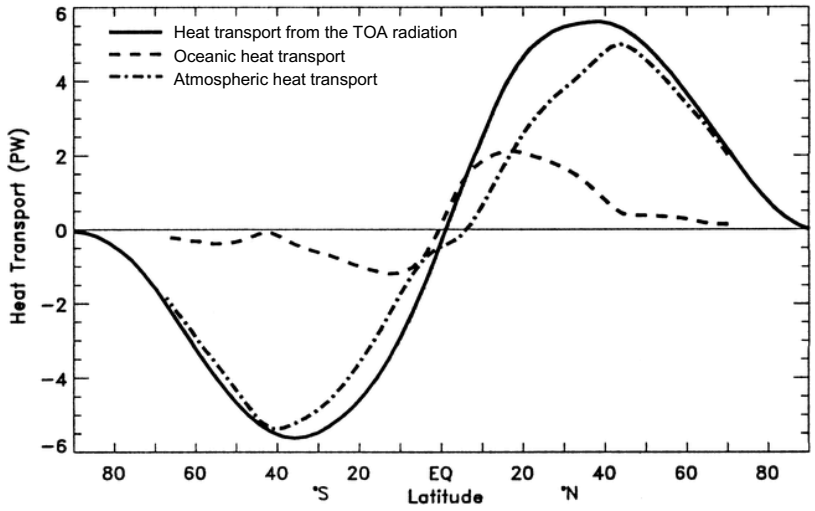

Fig. 2.1.: Required total heat transport from the top-of-the-atmosphere (TOA) radiation (solid) and derived estimates of the oceanic (dashed) and atmospheric meridional heat transport (dash-dotted). Positive (negative) values denote northward (southward) heat transport. Figure is adapted from Trenberth and Caron (2001).

The mechanisms described above can explain the global mean temperature, but not the global circulation patterns. To understand the drivers of atmospheric dynamic, it is necessary to analyse the latitudinal distribution of heating rates from incoming solar radiation. The net radiation is defined by the difference between the shortwave radiation absorbed by the Earth-atmosphere system and the longwave radiation emitted to space. In the global mean, net radiation is zero for thermal equilibrium. Locally, this is usually not the case. The geometry of the Earth and its orientation to the Sun, as well as albedo effects lead to a surplus of net radiation in low latitudes and a deficit of net radiation in high latitudes. This nonuniform heating of the Earth-atmosphere system drives the general circulation, atmospheric and oceanic poleward meridional transport is responsible to balance this disparity. The resulting general circulation is maintained against frictional dissipation by a conversion of potential energy to kinetic energy. The potential energy is a consequence of atmospheric expansion (compression) due to radiative heating (cooling). In lower latitudes, the Coriolis force is small or zero. Here, a more thermally direct circulation is forced by the geographical distribution of atmospheric heating, resulting in the meridional Hadley and zonal Walker circulation. In high latitudes, the meridional transport is modified strongly by the Coriolis force due to the Earth's rotation, thereby forming the strong westerlies in the mid-latitudes. The net radiation differences between high and low latitudes are particularly large in the respective winter sphere, as polar night causes a large energy deficit at the poles. This effect leads to an intensification of the westerlies in winter. The time mean circulation is almost circumpolar at mid and high latitudes and therefore possesses only a small meridional component to transfer heat between the equator and the poles. Hence, the meridional temperature gradient increases until the zonally symmetric circulation becomes unstable. This process of baroclinic instability is responsible for the development of synoptic systems

in the mid-latitudes. The subsequent formation of synoptic troughs and ridges controls a large amount of the meridional heat transport. The estimated meridional heat transports of atmosphere and ocean are displayed in Figure 2.1. The mid-latitude region between the Hadley cell and the polar cell is characterised by a maximum of atmospheric heat transport. This maximum at approximately 45°N is caused by baroclinic instabilities.

2.1.3 Baroclinic instability

Baroclinic instability plays a very important role in extratropical weather and climate, as it is understood to be the primary dynamic mechanistic cause for synoptic-scale, mid-latitude storms. Large-scale motion is dominated by a balance between the Coriolis acceleration and the pressure gradient force, the so called geostrophic wind. It is derived from a scale analysis of the horizontal momentum equation 2.1 for large-scale atmospheric motions and is given by:

$$\mathbf{v}_g = \frac{1}{\rho f}\mathbf{k} \times \boldsymbol{\nabla}_h p, \tag{2.12}$$

with the geostrophic wind vector $\mathbf{v}_g$, the Coriolis parameter f, a vertically directed unit vector $\mathbf{k}$ and the horizontal component of the nabla operator ∇_h.

The available potential energy of synoptic systems is proportional to the meridional temperature gradient. Baroclinicity is present, when the surfaces of constant pressure and constant density are not parallel. Consequently, the temperature varies along isobaric surfaces. In a baroclinic atmosphere the geostrophic wind generally has vertical shear. This shear is related to the horizontal temperature gradient by the thermal wind equation:

$$\mathbf{v}_T = \frac{\partial \mathbf{v}_g}{\partial z} = \frac{g}{fT}\mathbf{k} \times \boldsymbol{\nabla}_h T. \tag{2.13}$$

The first condition for baroclinic instability is vertical wind shear, so that $^{\partial \mathbf{v}_g}/_{\partial z} \neq 0$. Moreover, the thermal wind $\mathbf{v}_T$ needs to exceed a critical value $|v_T|_c$ (≈ 4 m/s) and at the same time the wavelength L of the disturbance must be sufficiently large (≈ 3000 km). Is this the case, the disturbance can grow by gaining kinetic energy at the expense of the available potential energy. Yet, not all baroclinic disturbances will grow as there are two stabilising effects: Short wavelengths are stabilised by vertical temperature stratification (static stability), whereas large wavelengths are stabilised by the β-effect, which is tied to the spherical shape of the Earth. Figure 2.2 shows a schematic illustration of these processes. The dominant wavelength L_{dom} describes the wavelength that becomes unstable first. For average atmospheric parameters, this parameter is estimated to be 3000 km, which is in the synoptic scale.

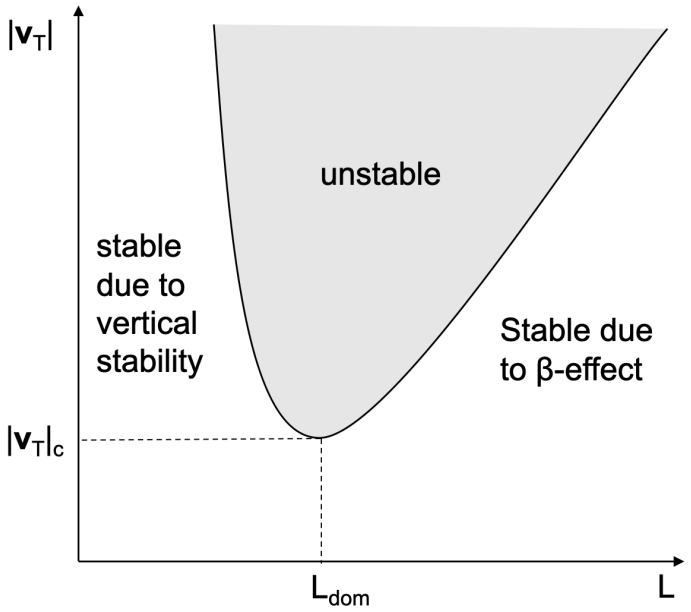

Fig. 2.2.: Schematic illustration of the baroclinic instability criteria as a function of the wavelength L and the absolute thermal wind $|v_T|$ (based on Etling, 2008). Vertical stability for short waves and the β-effect for long waves act as stabilisers.

2.1.4 Vertical structure of the atmosphere

The atmosphere can be vertically divided into the troposphere, stratosphere, mesosphere and thermosphere based on the mean vertical temperature profile. The layers are separated by the tropopause, stratopause and mesopause, indicating a change in the temperature gradient as shown in Figure 2.3, alongside the vertical profiles of the temperature and the ozone mixing ratio. These profiles represent the standard model for the mean mid-latitude atmosphere. However, in reality a single vertical profile varies with season, latitude and on a synoptical time scale, and can therefore strongly differ from the displayed profiles.

The troposphere is the lowest layer of the Earth's atmosphere. It is associated with most of the synoptic-scale activity and is also referred to as the weather layer. The troposphere contains approximately 99% of the atmospheric water vapour and 85% of the atmospheric mass (Holton, 2004). The tropopause as the upper boundary is located at approximately 8 km altitude in high latitudes in winter and reaches up to 18 km in the equatorial area. This difference is caused by the energy surplus of the low latitudes, which allows for air with more latent heat to reach higher altitudes. On average, the temperature in the troposphere decreases nearly linearly with height until reaching its minimum in the tropopause. The average lapse rate is 6.5 K/km.

The stratosphere stretches from the tropopause to the mesopause, i.e. from a temperature minimum to a maximum. A neutral lapse rate in the lower stratosphere is followed by a positive rate in the mid and upper stratosphere. This temperature increase with height can be

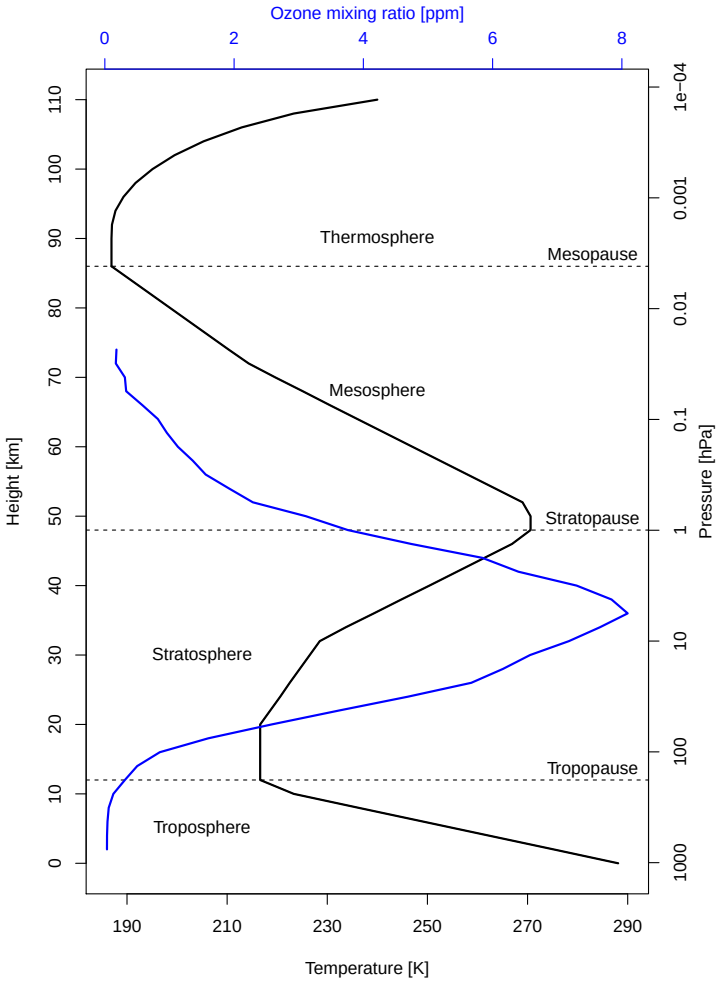

Fig. 2.3.: Vertical mid-latitude temperature and ozone profile based on US Standard Atmosphere (1976) and Krueger and Minzner (1976). The temperature in Kelvin is denoted by the black line, the ozone mixing ratio in parts per million by the blue line.

explained by the presence of ozone (cf. Fig. 2.3). The stratosphere contains approximately 90% of the atmospheric ozone with a maximum mixing ratio at 35 km. Ozone absorbs the highly energetic ultraviolet solar radiation and thereby heats the surrounding air. The altitude of the maxima of temperature and ozone diverge, as large parts of the UV light are already absorbed before they reach the ozone maximum. The stable stratification of the stratosphere inhibits vertical exchange of air masses. However, slow vertical exchange in the stratosphere is present. This is mainly driven by planetary waves and gravity waves (cf. Section 2.2.2).

Only a very small share of the atmospheric mass is located above the stratopause. The mesosphere is connected to decreasing temperatures with height, as there is less ozone that absorbs ultraviolet radiation. It is therefore dominated by net radiative cooling. The

absolut minimum temperature is reached at approximately 85 km at the mesopause, which is followed by the thermosphere, the last atmospheric layer before the exosphere. The thermosphere is characterised by a strong increase in temperatures with altitude. The ratio of atomic to molecular oxygen is large in the thermosphere and therefore temperatures increase with altitude due to absorption of highly energetic solar radiation. Depending on the level of solar activity, temperatures can reach up to 500 to 2000 K in the upper thermosphere.

2.2 Stratospheric dynamics

In this thesis, the main focus lies on the Northern Hemisphere stratosphere and troposphere as well as on their interaction. This focus is determined by the importance of stratospheric processes for seasonal predictions. Especially in winter, the stratospheric polar vortex can have a strong influence on tropospheric circulation patterns. Therefore, this section will give a closer insight into the processes involved in stratosphere dynamics and stratosphere-troposphere coupling.

2.2.1 Circulation patterns

In contrast to the troposphere, the horizontal gradient of heating in the stratosphere is generally weak enough to sustain barotropic stratification. Hence, baroclinic instabilities as described in Section 2.1.3 do not play a major role in the stratosphere, i.e. the circulation is less disturbed compared to the troposphere. An exception to this is the disturbance due to waves that can propagate into the stratosphere from the troposphere. These processes will be described in sections 2.2.2 and 2.2.3. Due to the strong static stability the energy budget of the stratosphere is dominated furthermore by radiative transfer. It is controlled by shortwave heating due to ozone absorption and longwave cooling due to CO_2 emissions into space. Hence, the energy budget of the stratosphere remains closer to radiative equilibrium. However, radiative equilibrium would imply a zonal circulation without any vertical or meridional motion. Nevertheless, both can be observed and are described by the Brewer-Dobson circulation. In the following, the fast primary circulation is analysed before describing the slow secondary Brewer-Dobson circulation. Whereas the primary circulation contains most of the kinetic energy and inertia of a flow, the secondary circulation is a weak circulation superposed on the primary circulation by the physical constraints of the system (e.g. Holton, 2004).

Primary circulation

Figure 2.4 shows the seasonal mean geopotential height in the mid stratosphere (10 hPa $\approx$ 35 km) for a climatology from 1979 - 2017 derived from ERA-Interim reanalysis. Further

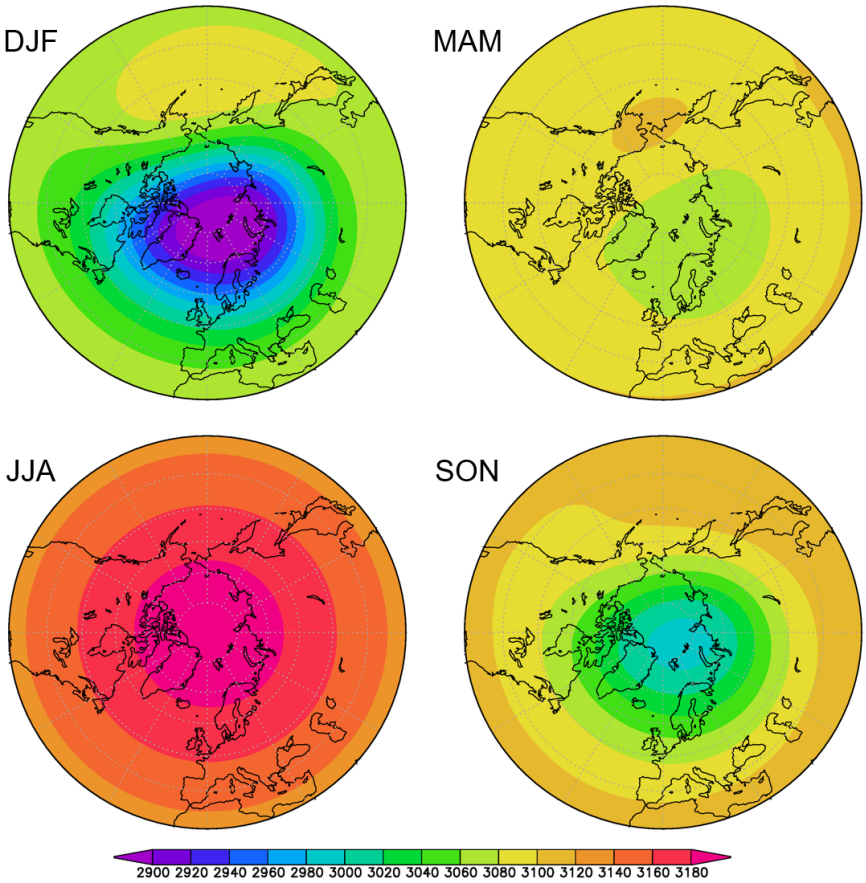

Fig. 2.4.: Seasonal mean geopotential height in 10 hPa for ERA-Interim reanalysis climatology from 1979-2017. Further details on the ERA-Interim reanalysis are given in Section 3.2. Polar stereographic view 30°-90°. The geopotential height is given in decameters (dam) for the meteorological seasons winter (DJF), spring (MAM), summer (JJA) and autumn (SON).

details on the reanalysis are given in Section 3.2. The geopotential height is calculated by dividing the geopotential by the Earth's gravitational acceleration $g = 9.80665\,m/s^{-2}$ and given in decametres (dam). Due to the constant insolation of the layers below in summer (JJA), a very stable high pressure system develops over the North Pole. In contrast to this, the lack of insolation in winter leads to a strong cooling of the air masses below and a strong low pressure system is formed in high latitudes. Surface friction is negligible in the stratosphere, so that the wind can be described by the balance between the Coriolis force and the pressure gradient force via the geostrophic wind equation 2.12. The vertical change of the geostrophic wind can be described with the thermal wind equation 2.13. The geostrophic wind flow is parallel to the isobars, resulting in a circumpolar easterly flow in summer and a strong westerly flow in winter. The zonal mean wind directions change from westerly to easterly in May and vice versa in September. The westerlies form the stratospheric polar vortex, which isolates the very cold air within. The winterly vortex is climatologically shifted towards Eurasia and a weak high pressure system develops over the Aleutian Islands. The Aleutian

high is forced primarily by an anticyclonic potential vorticity increase in the stratosphere and is often linked to the onset of a polar vortex disturbance (Colucci and Ehrmann, 2018). However, the mechanisms leading to the formation, evolution, and decay of the Aleutian high are not well understood. Although the zonally symmetric circulation is dominant in the stratosphere, meridional and vertical motion also exists. This secondary circulation will be described in the following section. Furthermore, planetary and gravity waves have the power to force the motion out of geostrophic balance (cf. Section 2.2.2).

Brewer-Dobson circulation

As the magnitude of the secondary circulation is weak compared to the zonal circulation, the nature of the ageostrophic flow can be revealed by the distribution of long lived tracers. Brewer (1949) and Dobson (1956) first discovered the meridional overturning circulation from balloon observations of trace species. The distributions of nitrous oxide (N_2O) and methane (CH_4) imply upwelling into the stratosphere in the tropics. This is caused by an overshooting of high reaching tropical cumulus clouds. Continuity forces a downwelling in middle and high latitudes. As the air entering the stratosphere passes trough the very high and cold tropical tropopause, nearly all of the water vapour is "freeze-dried". This also explains why so little water vapour is found above the tropopause. After a slow poleward transport of air, downwelling occurs in high latitudes, thereby allowing for stratospheric air intrusions into the troposphere.

This transport mechanism is very important for the understanding of the latitudinal distribution of ozone. Although the chemical source region of ozone is in the tropics, significant number densities of ozone are found at high latitudes. This poleward transport of ozone is caused by the Brewer-Dobson circulation.

2.2.2 Atmospheric waves

A wave can be defined as a form or a state of disturbance advancing with a finite velocity through a medium, thereby transmitting energy from one medium to the next (Mohanakumar, 2008). Waves are a very important atmospheric phenomena, as they allow for a communication of different, perhaps distant, parts of the atmosphere. Major wave influences occur in the stratosphere and mesosphere because of decreasing density and increasing wave amplitudes with altitude. Stratospheric circulation anomalies are caused mainly by wave forcing form the dense troposphere. Here, two types of waves that play an important role for the variability of the stratospheric polar vortex are described, namely meso-scale gravity waves and large-scale Rossby waves.

Gravity waves

Atmospheric gravity waves can only exist when the atmosphere is stably stratified. A fluid parcel which is displaced vertically can then undergo buoyancy oscillations. As buoyancy is the restoring force for gravity waves, the term "buoyancy waves" would be more accurate. However, in this thesis the more commonly used term "gravity wave" is chosen. In the atmosphere, gravity waves are able to propagate horizontally and vertically, as there is no upper boundary of the medium. These waves are referred to as internal in contrast to the external gravity waves, that are surface waves reaching their maximum amplitudes at the boundary of the fluid, e.g. shallow-water gravity waves. Internal gravity waves exist over a wide range of horizontal scales and typically have time scales short enough to ignore rotation, heat transfer and friction. For inertia-gravity waves with horizontal wavelengths of hundreds of kilometers, the Earth's rotation becomes a second restoring force besides the buoyancy. By considering small wave disturbances about a basic state of rest and thus neglecting the effects of Earth's rotation, the gravity wave dispersion relation can be derived as

$$\hat{\omega}^2 = \frac{N^2(k^2 + l^2)}{m^2 + \frac{1}{4H^2}}, \tag{2.14}$$

where the intrinsic frequency $\hat{\omega}$ is the frequency relative to the mean wind, N is the Brunt–Väisälä or buoyancy frequency, (k,l,m) are the wave number components and H is the scale height. The dispersion relation relates the wave frequency to the wave numbers (wave's spatial characteristics) and to the background atmosphere properties N.

Gravity waves are usually categorised by their source of origin, which can be orography or synoptic systems such as convection, jets or fronts. Since the horizontal scales of short gravity waves are smaller than current grid spacings in global weather and climate prediction models, these waves cannot be represented explicitly and must be parametrised. These parameterisations are of importance for the strato- and mesosphere, as the gravity waves amplitude will grow as the inverse square of the density. With exponential amplitude growth, the gravity waves will have grown so large that they become unstable and break, thereby altering the atmospheric flow by depositing stored momentum and energy. The drag exerted by the gravity waves is called gravity wave drag. It can be described by

$$\nabla \cdot \mathbf{F} = -\frac{k(\overline{u} - c)^3}{2HN}, \tag{2.15}$$

where k is the horizontal wave number, $\overline{u}$ is the zonally averaged wind and c is the phase speed of the gravity wave. Equation 2.15 can produce positive or negative acceleration of the zonal wind, depending on the sign of $\overline{u} - c$.

Rossby waves

Rossby or planetary waves have horizontal scales of thousands of kilometers and time scales of multiple days. They are strongly connected to the weather patterns in mid-latitudes. Rossby waves develop due to large-scale variations in potential vorticity and are mainly

caused by topography, temperature contrasts and synoptic cyclones. The latitude dependent Coriolis effect is the restoring force. An air parcel that has been deflected, rotates and is thereby moved back to the latitude of origin. This initiates an oscillation around the equilibrium latitude. The phase speed c of a Rossby wave can be derived by linearising the vorticity equation and is given by

$$c = u_0 - \frac{\beta L^2}{4\pi^2}, \tag{2.16}$$

where u_0 is the mean zonal flow, $\beta = \frac{\partial f}{\partial y}$ is the Rossby parameter with the Coriolis parameter f and L is the wavelength (e.g Etling, 2008).

Furthermore, planetary waves are the most important waves for transport from the troposphere to the stratosphere. Charney and Drazin (1961) developed a criterion for the vertical propagation of planetary waves into the stratosphere depending on the phase velocity c of the wave and the velocity of the zonally averaged zonal wind $\overline{u}$:

$$0 < \overline{u} - c < u_c = \beta \left(k^2 + l^2 + \frac{f^2}{4N^2H^2} \right)^{-1}, \tag{2.17}$$

where u_c is the critical zonal wind, which is defined by the variation of the Coriolis parameter with latitude β, the zonal wave number k, the meridional wave number l, the Coriolis parameter f, the Brunt–Väisälä frequency N and the scale height H. According to the Charney-Drazin criterion, the phase speed of a wave should be smaller than the average zonal wind in order to enable propagation into the stratosphere. Given a stationary orographically excited wave, the phase velocity can be set to zero. In this case, the criterion states that planetary waves can only propagate vertically in west wind regimes. This explains the stable and symmetric high pressure system in the stratosphere in summer, when the easterly circulation prevails. Hence, the stratospheric circulation in summer is determined by solar radiation. In winter, however, dynamic processes also play a role, because the vertical propagation of waves is supported by the westerly circulation. This explains the asymmetry of the stratospheric polar vortex as well as the strong disturbances that can occur in winter (cf. Section 2.2.3). Furthermore, there is a critical zonal wind, that hinders vertical wave propagation for in strong westerlies. The vertical propagation also depends on the wave number, whereby only wave numbers between one and three propagate into the stratosphere, as large zonal wave numbers k are inhibited from propagating into strong background winds (cf. Equation 2.17). The zonal wave number is defined as $k = (2\pi R_E cos\phi)/\lambda$, with the Earth's radius R_E, the latitude ϕ and the wavelength λ. In the stratosphere, wave numbers one and two are dominant, while wave number three hardly occurs. The resulting high variability of the winter stratosphere can be a challenging feature for atmospheric models.

2.2.3 Sudden stratospheric warmings

Sudden stratospheric warmings are caused by a rapid amplification of planetary waves propagating upward from the troposphere into the stratosphere. These strong wave pulses

are usually associated with a anomalously large waves in the troposphere (e.g. blocking activity). Wave breaking in the stratosphere is caused by a wave amplitude increase with decreasing density and/or interaction with a critical layer. Planetary wave breaking theory is based on Matsuno (1971): An initial anomalously intense planetary wave may propagate into the stratopause region and by depositing westward momentum on the mean flow, the westerly circulation around the polar vortex can be decelerated or even disrupted. The lower boundary of the resulting westward wind pocket then serves as a focal area for further interactions between planetary waves and the mean flow. This critical layer descends toward the lower stratosphere in time (e.g. Baldwin and Dunkerton, 2001). The meridionalisation of the stratospheric circulation is connected to a strong warming in the high latitudes, sometimes increasing the temperature of the polar stratosphere by as much as 30–40 K in a few days. Besides planetary waves, gravity waves and their interaction with the mean flow also play a large role in the evolution of stratospheric warmings. A filtering of gravity waves by the anomalous easterly flow induces strong mesospheric cooling during stratospheric warmings (Holton, 1983). Based on a model study of a major stratospheric warming event, Limpasuvan et al. (2012) demonstrate the strong interplay between gravity wave and planetary wave forcing during this event.

When the first stratospheric warmings were measured in Berlin in January and February 1952, it was initially not certain whether this was a technical error (Labitzke, 2013). Richard Scherhag, however, trusted the radiosonde measurements and was the first to document a sudden warming in the stratosphere. Scherhag also recognised that the warming slowly propagates downwards. The warming, initially known as the "Berlin phenomenon", is nowadays mostly referred to as a sudden stratospheric warming and can be divided into the following classifications:

Major stratospheric warmings (MSWs) occur from December to March, but in particular in January or February and are hence also referred to as major midwinter warmings. The polar region is heated so that the temperature gradient between 60 ° N and the pole is reversed. In addition, the zonal mean circulation at 60°N reverses at an altitude of 10 hPa, so that instead of the common westerly winds, easterly winds dominate. The polar vortex can either be shifted and replaced by the Alëuten high pressure system (wave 1 pattern) or split (wave 2 pattern). On average MSWs occur 6.5 times per decade (e.g. Butler et al., 2017).

Minor stratospheric warmings are also characterised by a reversal of of the temperature gradient between 60°N and the pole. However, there is no reversal of the zonal wind. These warmings are more frequent than MSWs, but have weaker effects.

Final warmings mark the transition from the cold, winter polar vortex to the high pressure system centred above the pole in summer. They occur every spring (March - May) with variable intensities.

2.2.4 Quasi-biennial oscillation

The quasi-biennial oscillation (QBO) is a quasi-periodic oscillation in the mean zonal winds of the equatorial stratosphere (Baldwin et al., 2001). It is characterised by a pattern of easterly and westerly wind regimes that alternate at intervals between 22 and 34 months, or on average 27 months. The QBO phase can be defined as easterly (QBO-E) or westerly (QBO-W) according to the sign of the zonal mean zonal wind in the lower stratosphere, e.g. in 50 hPa. The pattern occurs between 100 hPa and 2 hPa. The different regimes propagate downward in time with a rate of about 1 km/month. The amplitudes of the different regimes are rather constant above 50 hPa, below they start to decrease rapidly. The easterly regime has a stronger amplitude with easterlies up to 30 m/s, compared to 20 m/s for the westerly regime. The oscillation is symmetric about the equator and has an approximate Gaussian distribution with a latitudinal half-width of about 12°. The QBO is driven by a broad spectrum waves originating from the tropical troposphere, including gravity, inertia-gravity, Kelvin, and Rossby-gravity waves (Baldwin et al., 2001). These waves are produced by convection in the tropical troposphere, ranging from the scale of meso-scale convective complexes to planetary-scale phenomena. They transport easterly and westerly momentum into the stratosphere. Due to the high variety of vertical and horizontal wavelengths and phase speeds, for each wave the vertical profile of the zonal wind determines the critical level at which the momentum is deposited, thus driving the quasi-periodic oscillation of the QBO.

Although confined to the low latitudes, the phase of the QBO has strong impacts on the stratospheric polar vortex via wave coupling. Holton and Tan (1980) showed that the stratospheric polar vortex is on average weaker in the easterly QBO phase. This can be explained by equatorial winds influencing the waveguide for extratropical planetary waves. The surface in the tropics where the zonal mean wind is zero is a critical surface for planetary waves. For the QBO-E phase, the critical surface in the lower stratosphere is shifted towards the NH subtropics, thereby confining the vertical propagation of planetary waves to higher latitudes. Holton and Tan (1980) suggest that this concentrates the wave activity in the NH polar region and thus weakens the stratospheric polar vortex due to increased wave breaking. This is known as the Holton-Tan mechanism.

2.3 Atmospheric Teleconnections

Teleconnections are spatially and temporally large-scale anomalies that are related to each other at large distances. They are a fundamental component of the climate system. The teleconnections are caused by low-frequency variability on intra-seasonal to decadal time scales and manifest in preferred patterns of atmospheric circulation. Due to their long time scales, they are of particular interest for seasonal prediction. Teleconnections are commonly detected with the help of correlation analysis or by principal component analysis, which is also known as Empirical Orthogonal function analysis (cf. Section 3.3.1). Due

to the persistence of teleconnections, the understanding of the governing mechanisms reveals potential for predictability beyond typical weather forecast time scales. In the following, teleconnections that play a large role in this thesis will be discussed, namely the atmospheric Northern Hemisphere annular mode (NAM), including the local manifestation North Atlantic Oscillation (NAO) and its Pacific equivalent the Pacific-North America (PNA) pattern, and the coupled atmosphere-ocean El Niño-Southern Oscillation (ENSO). Further teleconnections, that are out of scope of this thesis, include the Antarctic Oscillation, the East Atlantic pattern, the West Pacific pattern as well as the oceanic Pacific Decadal Oscillation and Atlantic multidecadal Oscillation. The last part of this section will discuss how a rapidly warming Arctic influences the Arctic Oscillation and thus the mid-latitudes (Arctic-midlatitude linkages).

2.3.1 NAM, NAO and PNA

The NAM is a large-scale pattern of climate variability in the Northern Hemisphere and also referred to as the Arctic Oscillation (AO). As depicted in Figure 2.5, the AO is commonly defined by the leading empirical orthogonal function of the wintertime monthly mean sea level pressure anomaly field over the domain poleward of 20°N (Thompson and Wallace, 1998). Whereas the AO commonly refers to the surface pattern, the term NAM is used more generally for describing the pattern throughout the atmosphere. Due to the strong polar symmetric structure of the AO/NAM (cf. Fig. 2.5), in this thesis, a zonally-averaged approach is used to calculate the NAM (cf. Section 3.3.1 and Baldwin and Thompson, 2009). The NAM is a variation in the atmospheric pressure and wind pattern in mid and high northern latitudes and hence an important link between the Arctic and mid-latitudes. In the positive phase, polar pressure is lower than usual and the climatological high pressure systems over the mid-latitude Atlantic and Pacific are strengthened. The larger meridional pressure gradient leads to an intensification of the westerly polar jet stream, which confines colder air across polar regions. The negative phase is connected to a reduced meridional pressure gradient, which supports a weaker and wavier polar jet stream, allowing an easier southward penetration of colder, Arctic air masses. Consequently, the different phases of the NAM are strongly linked to weather and climate anomalies in mid-latitudes.

The North Atlantic Oscillation (NAO) can be viewed as the North Atlantic component of the Arctic Oscillation. The time series of the AO and NAO are highly correlated, however, the NAO has a less zonally symmetric appearance. The NAO describes the mutual strengthening and weakening of the Azores High and the Icelandic Low and is most pronounced during boreal winter. Its surface pattern with the two main centres of action is visualised in Figure 2.5. The NAO is strongly associated with the speed and direction of the westerly winds across the North Atlantic, the heat and moisture transport, as well as the frequency and strength of storms. Therefore alterations of the NAO are strongly connected to weather patterns in Europe: its positive (negative) phase is connected to warm and wet (cold and dry) weather in western and central Europe.

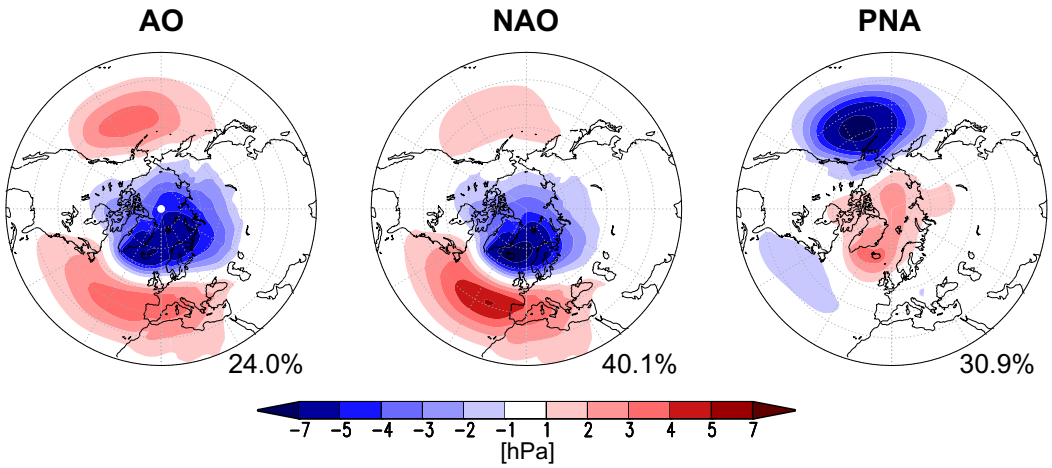

Fig. 2.5.: Loading patterns of the Arctic Oscillation (AO), North Atlantic Oscillation (NAO) and Pacific–North America (PNA) pattern in winter (DJF). The patterns are defined as the leading mode of Empirical Orthogonal Function (EOF) analysis of monthly mean sea level pressure during 1979-2017 period from ERA-Interim reanalysis data (cf. Section 3.2). The EOF analyses have been performed over the area 20°-90°N, 0°-360°W (AO), 20°-90°N, 106°W-30°E, (NAO), 20°-90°N, 120°E-300°E (PNA), respectively. The explained variance is given in the bottom right corner of the respective figure.

The Pacific–North America (PNA) pattern is strongly related to regional climate variation and atmospheric circulation over the North Pacific and across North America. With its main centres of action over the North Pacific, northwestern North America, and the southeastern United States (cf. Fig. 2.5), the PNA links the extratropical AO to the tropical El-Niño Southern Oscillation. Honda and Nakamura (2001) found that the Pacific centre of the AO is much stronger in winters when the PNA-like stationary wave train is very active. Furthermore, there exists a significant anticorrelation between the PNA and NAO indices at daily time scales (Song et al., 2009). The negative phase of the PNA has been connected to an enhanced Atlantic storm track due to increased baroclinicity over eastern North America (Pinto et al., 2011). Moreover, the positive phase of the PNA pattern tends to be associated with Pacific warm ENSO phases, and the negative phase tends to be associated with Pacific cold ENSO phases (cf. Section 2.3.2). The wave train of the PNA pattern emanates from the SST anomaly centre in the tropical central Pacific and propagates to North America (Horel and Wallace, 1981).

2.3.2 El Niño-Southern Oscillation

El Niño-Southern Oscillation (ENSO) is the most prominent and probably best observed interannual variation in the Earth's climate system. The quasi-periodic fluctuation in sea surface temperatures (El Niño) and the air pressure of the overlying atmosphere (Southern Oscillation) across the equatorial Pacific Ocean has a period of 2-7 years. The warm (cold)

phase of ENSO is connected to anomalously warm (cold) temperatures in the central and eastern equatorial Pacific and is known as El Niño (La Niña). El Niño is connected to a weakening of the trade winds, a reduced slope of the thermocline and a reduction in the upwelling of cold water in the eastern Pacific. As warmer equatorial eastern Pacific surface temperatures further reduce the trade winds, these processes initiate a positive feedback loop. The opposite mechanisms account for the La Niña phase.

Beside the direct local effect of ENSO, there is a wide range of teleconnections that are associated with it. This makes ENSO to a major driver for extratropical Northern Hemisphere interannual variability, especially in the Tropics and the Pacific region (Brands, 2017), where ENSO is strongly linked to the PNA pattern. As statistical and dynamical models are able to provide effective predictions of ENSO warm and cold events 6–12 months ahead (Barnston et al., 2012), they are an important contributor to seasonal predictions in these regions. The impacts of ENSO on the North Atlantic–European sector, however, are discussed more controversially. While Brands (2017) states that the European ENSO teleconnections are not robust, Brönnimann (2007) shows, that the effect of El Niño on European climate is statistically significant and climatologically relevant. The El Niño signal is most consistent in late boreal winter and it resembles the negative pattern of the NAO. This signal is potentially produced by downward coupling from the stratosphere (Randel, 2004) and is large enough to be useful for seasonal forecasting (Ineson and Scaife, 2009). Different studies have shown downward propagation of the ENSO signal from the upper stratosphere in January to the lower stratosphere in February and March (e.g. Randel, 2004; Manzini et al., 2006; Garfinkel and Hartmann, 2007; Free and Seidel, 2009; Manzini, 2009). Following Baldwin and Dunkerton (2001), these signals can also propagate into the troposphere by stratosphere-troposphere coupling.

2.3.3 Arctic-midlatitude linkages

The Arctic has developed to one of the hot spots of climate change, as it is warming at about double the rate of the lower latitudes, a phenomena widely known as Arctic Amplification (AA) (e.g. Serreze and Barry, 2011; Dethloff et al., 2019). The knowledge of the underlying processes of AA, however, is still incomplete. AA does not only depend on a number of coupled local feedback mechanisms, such as surface albedo, water vapor, clouds, lapse rate, and Planck feedback processes (Wendisch et al., 2017), but is also largely a function of remote large-scale atmospheric and oceanic dynamical feedback mechanisms. The related horizontal atmospheric and oceanic energy transports between the lower latitudes and the Arctic establish Arctic-midlatitude linkages (e.g Cohen et al., 2014). However, the identification and understanding of tropospheric and stratospheric pathways linking Arctic climate changes to changes in the atmospheric circulation, in particular in mid-latitudes, is still a research challenge (Vavrus, 2018). This challenge arises mainly due to the nonlinear dynamics and hence strong internal variability of the mid-latitude atmospheric circulation, involving the complex interactions between jet stream, transient synoptic systems, the onset

and maintenance of blocking as well as the growth and phasing of planetary waves (e.g Lee et al., 2019).

A sequence of processes leading from Barents Kara Seas (BKS) warm anomalies in late summer and autumn to cold Eurasian temperatures in mid to late winter in the recent decades has been connected to a complex interplay between troposphere and stratosphere (Cohen et al., 2014). This stratospheric pathway is considered robust and will be shortly outlined in the following. Additional heat uptake in sea ice free areas in summer and early autumn and thus delayed refreezing in October and November, leads to additional ocean heat release, in particular to the Arctic boundary layer, in October and November. The related decrease in the vertical static stability is associated with an earlier onset of baroclinic instability, which can force additional planetary waves (Jaiser et al., 2012). Furthermore, additional oceanic moisture release to the Arctic atmosphere has been connected to increased Siberian snow cover and a strengthening of the Siberian High (Wegmann et al., 2015). The increased snow cover in autumn has also been linked to upward-propagating planetary wave pulses (Cohen et al., 2007). Additionally, the persistence of the BKS anomalies into winter act as a diabatic heating source, resulting in direct forcing of planetary waves in November (Honda et al., 2009) and a increased frequency of high-latitude blocking in December and January (e.g. Mori et al., 2014; Kretschmer et al., 2016; Crasemann et al., 2017). The enhanced upward propagation of planetary waves can lead to wave breaking in the polar stratosphere, which in turn weakens the polar vortex (e.g. Kim et al., 2014; Jaiser et al., 2016). The weakening of the stratospheric vortex is connected to an increase of polar stratospheric temperatures in January. The subsequent downward propagation of these stratospheric circulation anomalies leads to a negative NAO/AO-like pattern persisting until February and March (Jaiser et al., 2016). The negative NAO/AO-like pattern has been associated with the "warm Arctic—cold continents" pattern in mid to late winter (Overland et al., 2011).

Whereas the growing evidence for Arctic-midlatitude linkages is mostly based on reanalysis data, the mid-latitudes temperature response to Arctic sea ice loss of model simulations is highly divergent (Cohen et al., 2020). In particular in modelling studies using large ensembles, the atmospheric response to Arctic sea ice loss is small relative to the internal variability, and hence has been attributed to internal variability (e.g. Smith et al., 2017; Ogawa et al., 2018; Blackport et al., 2019). These results have led to doubts on the impact of Arctic amplification and Arctic sea ice loss on remote atmospheric circulation changes. However, during the last years, possible sources for these discrepancies have been identified. They comprise the important role of nonlinear internal atmospheric variability, shortcomings in the experimental design of the model simulations, the impact of the background atmosphere–ocean state, as well as deficiencies in the representation of atmospheric processes in climate models relevant for Arctic–lower latitude linkages (Screen et al., 2018).

The described pathway of Arctic-mid-latitude linkages operates on sub-seasonal to seasonal time scales and strongly depends on the forcing and propagation of planetary waves and their interactions with the smaller-scale synoptic waves and the mean circulation. Due to their time scales they are furthermore of interest for seasonal predictions.

3 Atmospheric model and methods of analysis

3.1 Atmospheric model ICON-NWP

The ICOsahedral Non-hydrostatic atmosphere model in numerical weather prediction mode (ICON-NWP) is part of the unified model approach in Germany. This approach merges all the different scales in time and space in one model. The non-hydrostatic core makes ICON applicable on a wide range of scales from ∼100 km to ∼100 m, as also convective instabilities can be handled. Besides the global NWP configuration, which will be used for this study, ICON exists in a climate mode (ICON-A; Giorgetta et al., 2018), a configuration with Aerosols and Reactive Trace gases (ICON-ART; Rieger et al., 2015) as well as the setups in limited area mode (ICON-LAM) and large eddy mode (ICON-LEM). All configurations of ICON share the same dynamical core (Zängl et al., 2015). This model hierarchy allows for testing of parameterisations from a very small-scale (≈ 100 m) LEM setup to the global scale. This study will focus on seasonal experiments with the global setup of ICON-NWP. The following two sections describe the model itself and our experimental setup.

3.1.1 Model description

In this section, the key features of ICON-NWP will be introduced. A thorough description of the dynamical core is given by (Zängl et al., 2015) and the database reference manual (Reinert et al., 2018). For working with the model the ICON Model Tutorial is very helpful. The tutorial version from April 2019 can be downloaded at `https://code.mpimet.mpg.de/attachments/download/19568/ICON_tutorial_2019.pdf`. The ICON model is distributed under an institutional license. A licence can be obtained in contact to DWD via `contacticon@dwd.de` or by following the information on the public ICON website `https://code.mpimet.mpg.de/projects/iconpublic`.

Icosahedral grid

The most prominent feature of ICON is the icosahedral grid. An icosahedron is projected onto a sphere and consists of 20 equilateral spherical triangles (cf. Fig. 3.1 a). Each edge of these triangles is initially divided into n parts. Connecting the new vertices yields n^2 new spherical triangles within the original triangle. This is followed by k subsequent

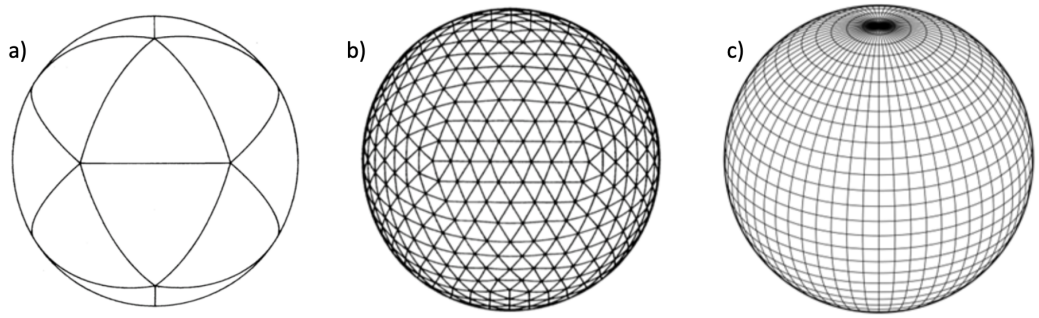

Fig. 3.1.: Illustration of the original icosahedron after projection onto the sphere (a), the global ICON grid in **R2B2** resolution (b) and a traditional regular latitude-longitude grid for comparison (c), adapted from Reinert et al. (2018).

edge bisections. The resolution of the resulting grid is given by **R**n**B**k. For a given model resolution, the total number of grid cells n_c is calculated as:

$$n_c = 20n^2 4^k. \tag{3.1}$$

The average cell area $\overline{\Delta A}$ is a function of the total amount of grid cells n_c and the Earth's radius r_e:

$$\overline{\Delta A} = \frac{4\pi r_e^2}{n_c}, \tag{3.2}$$

with $r_e = 6.371229 \cdot 10^6 m$. The average horizontal grid resolution $\overline{\Delta x}$ is then calculated with the help of equation 3.2 and 3.1:

$$\overline{\Delta x} = \sqrt{\overline{\Delta A}} = \sqrt{\frac{\pi}{5}} \frac{r_e}{n2^k}. \tag{3.3}$$

Table 3.1 lists the above described quantities for commonly used ICON resolutions. In particular, the number of cells and the average grid resolution enable a comparison to the more commonly used Gaussian latitude-longitude grid. This study applies the R2B5 resolution, which corresponds to a grid spacing of 78.9 km. The DWD uses the R3B7 resolution for the operational global weather forecast. This corresponds to an average resolution of 13.2 km.

Whereas scalars are defined at the triangle circumcenters, the wind components are given at the midpoints of the triangle edges and measured orthogonal to the edges. In contrast to a regular grid, ICON does not show singularities at the poles, as the distance between the grid points does not depend so much on the position on the globe (cf. Fig. 3.1 b and c). In addition, it is possible to run global simulations with a static mesh refinement, thereby allowing for 1-way and 2-way nesting. With each nesting level, the resolution in ICON increases by a factor of 2.

Tab. 3.1.: Commonly used ICON resolutions given in the **R**n**B**k notation. The **R2B2** resolution is shown for comparison. Corresponding total number of cells n_c, average cell area $\overline{\Delta A}$ and average grid resolution $\overline{\Delta x}$.

Grid	№ cells n_c	Avg. cell area $\overline{\Delta A}$ [km^2]	Avg. resolution $\overline{\Delta x}$ [km]
R2B2	1280	398516.5	631.3
R2B4	20480	24907.3	157.8
R2B5	81920	6226.8	78.9
R2B6	327680	1556.7	39.5
R2B7	1310720	389.2	19.7
R3B7	2949120	173.0	13.2

Vertical grid

Instead of the common pressure-based vertical coordinates, ICON uses a height based vertical coordinates with Lorenz-type staggering. More specifically, the vertical velocity is defined at half levels and other prognostic variables at full levels. ICON can be run with up to 90 vertical levels. The lowermost level is at 20 m and the uppermost level at 75 km. Based on Leuenberger et al. (2010), ICON employs a smooth level vertical (SLEVE) coordinate, which enables a faster transition to smooth levels in the upper troposphere and lower stratosphere.

Governing equations

As described in Section 2.1.1, the fundamental hydro-thermodynamic equations are based on the physical principles of conservation of momentum, mass and energy. However, due to the compressible non-hydrostatic approach of ICON, the hydro-thermodynamic equations need to be adjusted. The equation system of ICON is based upon the prognostic variables suggested by Gassmann and Herzog (2008). They present equations for a Reynolds averaged model atmosphere comprised of dry air and water in three phases plus precipitating fluxes. Turbulent fluctuations are separated from the mean flow by applying density ρ weighted averaging, where every field ϕ is decomposed into a density weighted mean $\widehat{\phi}$ and a deviation ϕ'' (Hesselberg, 1926):

$$\phi = \widehat{\phi} + \phi'', \tag{3.4}$$

where

$$\widehat{\phi} = \frac{\overline{\rho\phi}}{\overline{\rho}}.$$

$\overline{\phi}$ thereby denotes the classical Reynolds average. The advection term of the momentum equation is reformulated with the so-called Lamb transformation ($\boldsymbol{v}\cdot\nabla\boldsymbol{v} = \boldsymbol{w}\times\boldsymbol{v}+\nabla\frac{1}{2}\boldsymbol{v}^2$). In ICON, the two-dimensional Lamb transformation is used to convert the nonlinear momentum

advection into a vector-invariant form. The basic governing equations of momentum, mass and energy are subsequently given as:

$$\frac{\partial \widehat{v}_n}{\partial t} + \frac{\partial \widehat{K}_h}{\partial n} + (\widehat{\zeta} + f)\widehat{v}_t + \widehat{w}\frac{\partial \widehat{v}_n}{\partial z} = -c_{pd}\widehat{\theta}\frac{\partial \overline{\Pi}}{\partial n} - F(v_n), \tag{3.5}$$

$$\frac{\partial \widehat{w}}{\partial t} + \widehat{\mathbf{v}}_h \cdot \nabla \widehat{w} + \widehat{w}\frac{\partial \widehat{w}}{\partial z} = -c_{pd}\widehat{\theta}\frac{\partial \overline{\Pi}}{\partial z} - g, \tag{3.6}$$

$$\frac{\partial \overline{\rho}}{\partial t} + \nabla \cdot (\overline{\rho}\widehat{\mathbf{v}}) = 0, \tag{3.7}$$

$$c_{pd}\overline{\Pi}\frac{\partial \overline{\rho}\widehat{\theta}}{\partial t} = -c_{pd}\overline{\Pi}\nabla \cdot (\overline{\rho}\widehat{\mathbf{v}}\widehat{\theta}) + \overline{Q}. \tag{3.8}$$

The governing equations include the prognostic variables $\widehat{v}_n$, $\widehat{w}$, $\overline{\rho}$ and $\widehat{\theta}$, which are the horizontal velocity component normal to the triangle edges, the vertical wind component, the density and the potential temperature, respectively. The quantities $\widehat{v}_t$, $\widehat{\mathbf{v}}_h$ and $\widehat{\mathbf{v}}$ denote the reconstructed tangential (t) velocity component, the horizontal (h) and three-dimensional wind vectors, respectively. The further symbols are defined as horizontal kinetic energy $\widehat{K}_h = \frac{1}{2}(v_n^2 + v_t^2)$, vertical vorticity component $\widehat{\zeta} = (\nabla \times \widehat{\mathbf{v}}) \cdot \mathbf{k}$, Coriolis parameter f, specific heat capacity of dry air at constant pressure c_{pd}, turbulent momentum fluxes $F(v_n)$, gravitational acceleration g, diabatic heat-source term $\overline{Q}$ and the Exner function $\overline{\Pi}$. Furthermore, $\partial/\partial t$, $\partial/\partial n$ and $\partial/\partial z$ are the temporal, horizontal and vertical derivatives. The non-dimensional Exner function replaces pressure p as a vertical coordinate. It is defined as:

$$\Pi = \left(\frac{p}{p_0}\right)^{\frac{R}{c_{pd}}}, \tag{3.9}$$

with the standard reference surface pressure p_0 and the ideal gas constant R. Tracer transport can be included in the system by adding the partial mass continuity equation to the set of equations and solving it for each tracer.

Physical parameterisations

Processes that occur on scales too small to be resolved directly are parameterised in atmospheric models. In ICON-NWP, these processes include the radiation schemes for longwave and shortwave radiation, a cloud cover parameterisation, the cloud microphysics packages for the single- and double-moment scheme, a package for mass fluxes due to shallow and deep convection, the turbulent transfer schemes and the land parameterisations, which include the treatment of lakes and sea ice as well as the land-soil model TERRA. These parameterisations are kept constant in the different experiments in this thesis. A detailed description of all parameterisations is given in the ICON tutorial. The physics parameterisations furthermore include the sub-grid scale orographic drag, the non-orographic gravity wave drag and a sea ice parameterisation scheme. These parameterisations will be described in the following. The gravity wave drag parameterisations are adjusted as part of RQ2 and the sea ice parameterisation plays a role in RQ4 (cf. Section 1.3).

Sea ice parameterisation scheme. The sea ice parameterisation scheme used within ICON-NWP is based on Mironov et al. (2012). This scheme accounts for thermodynamic processes only and does not include ice rheology. The horizontal distribution of the ice cover, i.e. the sea ice fraction, in our case is prescribed by the boundary data (cf. Section 3.1.2). When used for weather prediction applications, it is governed by the data assimilation scheme. This scheme calculates the ice surface temperature and thickness by using an integral approach to solve the heat transfer equation on a finite difference grid. It uses an assumed shape of the temperature profile within the ice and the integral heat budget of the ice slab. This integral approach enables the solution of ordinary differential equations (in time) instead of partial differential equations (in depth and time). In the current version, the effect of snow on ice is accounted for implicitly through the surface albedo with respect to solar radiation. The ice thickness H_i is calculated by

$$\frac{dH_i}{dt} = -\Phi_i'(0)\frac{\kappa_i}{\rho_i L_f}\frac{\theta_i - \theta_f}{H_i} - \frac{Q_w}{\rho_i L_f}, \tag{3.10}$$

where $\Phi_i'(0)$ is the scaled temperature gradient at the ice bottom, κ_i is the molecular heat conductivity of ice, ρ_i is the density of ice, L_f is the latent heat of fusion, θ_i is the temperature at the upper surface of the ice, θ_f is the salt water freezing point and Q_w is the heat flux from water to ice. The ice starts to melt, when the heat flux from water to ice exceeds the heat flux within the ice. A mean sea ice thickness distribution from an ICON climatology is given in Figure 4.32 of Section 4.4.

Sub-grid scale orographic drag. Depending on its source, the gravity wave drag can be separated into an orographic and non-orographic part (cf. Section 2.2.2). In ICON, both are part of the slow-physics parameterisations (larger time stepping), but are treated individually. The orographic drag is described in this section and non-orographic drag in the following.

The orographic gravity wave drag is parameterised as part of the sub-grid scale orographic (SSO) drag scheme, which is based on the work of Lott and Miller (1997). It was implemented to increase the surface drag in the model and reduce surface pressure biases ("highs too high, lows too low"). With sufficiently high sub-grid scale orography, low level flow is blocked. This results in a form drag at the mountain flanks and a generation of gravity waves, when the upper part of the low level flow is led over the orography. The non-dimensional height H_n of the sub-grid scale mountain is regarded as the inverse of the Froude number Fr and is defined as:

$$H_n = \mathrm{Fr}^{-1} = \frac{NH}{|U|}, \tag{3.11}$$

with the Brunt-Väisälä frequency N, the maximum height of the mountain H and the wind speed $|U|$. The Brunt-Väisälä frequency is given as

$$N = \sqrt{\frac{g}{\theta}\frac{\partial\theta}{\partial z}}. \tag{3.12}$$

If H_n is large, there is a blocked regime: The vertical motion of the fluid is limited and part of the low level flow goes around the mountain. For a small H_n, the flow goes over the mountain and gravity waves are forced by the vertical motion. The orographic input fields for the SSO scheme originate from the Global Land One-km Base Elevation Project (GLOBE) data set, which has a resolution of approximately 1 km (Hastings et al., 1999). The SSO scheme has four tuning parameters: the critical Froude number (tune_gfrcrit), the low level wake drag constant (tune_gkwake), the gravity wave drag constant (tune_gkdrag) and the critical Richardson number (tune_grcrit). The critical Froude number has a default value of 0.4 and controls the likelihood for low level blocking to occur. A large critical Froude number will lead to more frequent low level blockings, whereas a small critical Froude number will increase the frequency of flow going over the mountain. Hence, a reduction of the critical Froude number will also lead to a reduction in gravity wave excitation. The low level wake and the gravity wave drag constants are directly proportional to the magnitudes of the SSO drag and the orographic gravity wave drag. They have default values of 1.5 and 0.075. And finally, the critical Richardson number is a control parameter for the onset of gravity wave breaking. The default value is 0.25. An increase in this number leads to reduction of the altitude where the gravity waves tend to break and exert drag.

Non-orographic gravity wave drag. As the gravity waves originating from synoptic-scale flow potentially have smaller horizontal and vertical wave lengths than the horizontal and vertical grid mesh size, they need to be parameterised in the model. In addition, these non-orographic gravity waves are known to significantly impact the middle and upper atmosphere and are therefore of great importance for the stratospheric circulation (e.g. Polichtchouk et al., 2018b). The non-orographic gravity wave drag parameterisation in ICON is based on Warner and McIntyre (1996) and Scinocca (2003), and is described in Orr et al. (2010). The parameterisation prescribes vertical fluxes of horizontal momentum at a launch level in the upper troposphere. It considers a statistical mean of all sources of upward propagating gravity waves. The magnitude of the integral of the momentum fluxes over the gravity wave spectrum is assumed to be constant and represented by

$$\rho F(cos\varphi_i, sin\varphi_i)|_{z=z_0} = \rho_0 F_0(cos\varphi_i, sin\varphi_i) = \rho\overline{w'\mathbf{v}'_h}|_{z=z_0} = \rho\overline{w'|\mathbf{v}'_h|}(cos\varphi_i, sin\varphi_i)|_{z=z_0}, \tag{3.13}$$

where ρ is the density of air, z_0 is the launch level, φ_i is the azimuthal angle, which is element of four horizontal directions of horizontal momentum sampled by the scheme, w' and $\mathbf{v}'_h$ are gravity wave borne fluctuations of the vertical and horizontal wind components. The spatial average over one grid cell is denoted as overline. The magnitude $\rho_0 F_0$ is tuneable via the parameter tune_gfluxlaun and is set to a default value of 0.0025 Pa. With the help of the spectral distribution of ρF at the launch level from Equation 3.13 and a given atmospheric state in a grid cell, ρF can be integrated vertically. The drag exerted on the horizontal flow is defined by the vertical divergence of the momentum flux:

$$\left(\frac{\partial \mathbf{v}_h}{\partial t}\right)_{drag} = \left[\frac{\partial (u,v)}{\partial t}\right]_{drag} = -\frac{1}{\rho}\frac{\partial(\overline{\rho F}_{zonal}, \overline{\rho F}_{meridional})}{\partial z}. \tag{3.14}$$

In this case $\overline{(\cdot)}$ denotes the integral over the gravity wave spectrum. The drag becomes non-zero at heights, where the gravity waves typically break.

Both the orographic and non-orographic drag are limited by a height-dependent threshold value to counteract numerical instabilities caused by a too strong increase of the wind magnitude. Furthermore, the involved processes are assumed to be irreversible and therefore provide a source of heat. The related temperature tendency is derived from the Gibbs equation, a thermodynamic equation used for calculating changes in the Gibbs energy of a system as a function of temperature.

3.1.2 Experimental setup

This study employs ICON-NWP in version 2.1.0 as distributed by the DWD with the ICON tutorial 2018. In this work, the model is set up with the horizontal resolution **R2B5**, which corresponds to a grid mesh of approximately 80 km (cf. Table 3.1), and 90 vertical levels up to a height of 75 km. The seasonal experiments in a global setup are initialised with T255 ERA-Interim data on the first of September of the respective year and run for 9 months, thereby including meteorological autumn, winter and spring. The initial data was downloaded with the Meteorological Archival and Retrieval System (MARS, see `https://software.ecmwf.int/wiki/display/UDOC/MARS+user+documentation`). MARS is the main repository for meteorological data at ECMWF. Based on Atmosphere Model Intercomparison Project (AMIP) protocol, this study uses prescribed mid-monthly sea surface temperatures and sea ice concentrations produced by the Program for Climate Model Diagnosis and Intercomparison for the AMIP experiments of CMIP6 (Taylor et al., 2000). The CMIP6 boundary data uses a regular 1° grid (Durack and Taylor, 2018). The main results of this study are not sensitive to the boundary data, as sensitivity experiments with ERA-Interim boundary data show the same features. The initial and boundary data was interpolated to the icosahedral **R2B5** ICON grid using the DWD ICON tools, that are part of the ICON model package. Concerning the volume mixing ratios of CO_2, CH_4, N_2O, CFC-11 and CFC-12, this study uses the historical greenhouse gas concentrations for CMIP6 (Meinshausen et al., 2017), complemented by NOAA/ESRL Global Monitoring Division global and monthly mean data for 2015, 2016 and 2017.

All ICON experiments are generated by simulating periods from September to May for 1979/80 to 2016/17 (38 years), with each experiment consisting of five ensemble members. This leads to a total of 190 single model runs per experiment. The ensemble was generated by shifting the initialisation by ± 6 h and ± 12 h. The different ICON experiments only vary in their gravity wave drag related parameterisations, as shown in Table 3.2. Whereas ICON_{ctl} uses the default settings for the parameterisations of the SSO scheme and the non-orographic gravity wave drag, these parameterisations were adjusted in the sensitivity experiments ICON_{nogwd-}, ICON_{sso-} and ICON_{gwd-} with the goal of more realistically representing the stratospheric dynamics in ICON. The non-orographic gravity wave drag is reduced in ICON_{nogwd-} by decreasing the parameter for the total launch momentum flux in each azimuth (tune_gfluxlaun) by 20% from 0.0025 Pa to 0.002 Pa (0.001 Pa). In ICON_{sso-} the

strength of the SSO scheme is reduced by decreasing the low level wake drag constant (tune_gkwake) and the gravity wave drag constant (tune_gkdrag) by 20% from 1.5 to 1.2 and 0.075 to 0.06 respectively. Furthermore, the critical Froude number (tune_gfrcrit) is increased from 0.4 to 0.5. ICON$_{gwd-}$ combines parameterisations from ICON$_{nogwd-}$ and ICON$_{sso-}$. The physical background of the different parameterisations is given in the previous section.

Tab. 3.2.: Summary of the parameters used for the different ICON experiments in this thesis. The parameter tune_gfluxlaun describes the total launch momentum flux on each azimuth. The parameters tune_gkwake, tune_gkdrag and tune_gfrcrit describe the low level wake drag constant, the gravity wave drag constant, and the critical Froude number respectively and are a part of the SSO scheme.

Experiment	tune_gfluxlaun	tune_gkwake	tune_gkdrag	tune_gfrcrtit
ICON$_{ctl}$	2.5 mPa	1.5	0.075	0.4
ICON$_{nogwd-}$	2.0 mPa	1.5	0.075	0.4
ICON$_{sso-}$	2.5 mPa	1.2	0.060	0.5
ICON$_{gwd-}$	2.0 mPa	1.2	0.060	0.5

3.2 Reanalysis data ERA-Interim

The ERA-Interim reanalysis will be used as a reference product for the seasonal experiments with ICON-NWP. This section will give a short summary on the ERA-Interim reanalysis product, the full description is given by Dee et al. (2011).

Meteorological data is collected around the world from meteorological stations on land, balloons, airplanes, ships, buoys and since 1979 with increasing importance from satellites. This huge amount of observations of atmospheric parameters is very important for the understanding of our current weather and climate. Yet, a comparison of atmospheric models with resolutions around 80 km to very local measurements needs to be treated with caution. Here, the reanalysis comes into play, directly connecting observations with state-of-the-art numerical weather prediction models. Reanalysis products consistently assimilate high quality observational data for the integration of an atmospheric model, thereby merging scattered observations of various kinds into a gridded, physically consistent data set. By integrating the model for the past and assimilating all these measurements, reanalysis products are a realistic representation of the past weather and are able to close observational gaps. However, the quality of the reanalysis is dependent on the quality and amount of observations as well as the quality of the underlying model and data assimilation system. The ERA-Interim reanalysis is produced with a sequential data assimilation scheme, which advances forward in time using 12-hourly analysis cycles. In each cycle, available observations are merged with prior information from a forecast model, thereby estimating

the evolving state of the global atmosphere. The forecast model allows for extrapolating information from locally observed parameters to unobserved parameters in a physically meaningful way.

The ERA-Interim reanalysis is a well tested and commonly used reanalysis product of the European Centre for Medium-range weather forecast (ECMWF). It is based on a 2006 release of the Integrated Forecast System (IFS) and covers the time period from 1st January 1979 to 31st August 2019. The IFS model is run with a spectral resolution of T255, which corresponds to a horizontal resolution of approximately 80 km or 0.5°. There are 60 vertical levels from the surface up to a height of 0.1 hPa. In this study, ERA-Interim data up to a height of 1 hPa for the years 1979 to 2017 is applied. Furthermore, due to capacity reasons, for parts of the analysis a reduced resolution output of 2° and 37 vertical levels is used.

ERA-Interim reanalysis data is made available at `https://apps.ecmwf.int/datasets/data/interim-full-daily`. The reanalysis serves as reference for the ICON model simulations. In addition, the simulations are initialised with ERA-Interim fields on a T255 grid.

3.3 Methods of analysis

This section describes the dynamical and statistical methods used for the analysis of the model and reanalysis data described above. The computational tools used for the analysis of data in this thesis include the scripting language R (`https://www.r-project.org/`), CDO (Climate Data Operators, `https://code.mpimet.mpg.de/projects/cdo/`), and GrADS (Grid Analysis and Display System, `http://cola.gmu.edu/grads/`). Furthermore, this study employed the services of the high performance computers Mistral (DKRZ) and Ollie (AWI). ICON model output is automatically interpolated to a 0.75° regular latitude-longitude grid before further analysis.

3.3.1 NAM index for stratosphere–troposphere coupling

The Northern annular mode (NAM) is the dominant pattern of dynamic variability in the extratropical Northern Hemisphere (cf. Section 2.3.1). This accounts not only for the troposphere, but especially for the stratosphere, where variations in the stratospheric vortex become apparent in the NAM (cf. Section 2.2). Baldwin and Dunkerton (2001) showed that the calculation of the NAM index is a useful method to make stratosphere-troposphere coupling visible. In Baldwin and Thompson (2009), different stratosphere-troposphere coupling indices are discussed: A correct representation of the coupling requires a multi-level index with a high time resolution. This index is supposed to represent spatial patterns in the troposphere that are most strongly coupled with stratospheric variability and should be robust as well as computationally feasible. Taking this into account, the authors favour a methodology based on empirical orthogonal functions (EOFs) of the daily, zonally-averaged

geopotential. Hence, this methodology is used to calculate the NAM index and its calculation is described in the following:

EOF calculation is a method to find the signals within a data set, that explain the most variance under the constraint of orthogonality. It has been shown (e.g. Von Storch and Zwiers, 2001), that the solution of this optimisation problem is given by the eigenvectors of the covariance matrix. The EOFs form the new orthogonal basis, from which the data can be decomposed with respect to the new basis. The NAM index is calculated by means of geopotential height data, which is organised in a data matrix Z, containing n observations in time of the geopotential z_i, which is defined at p spatial points. The seasonal cycle is removed from the data and to ensure equal-area weighting, all fields are pre-weighted by the square root of the cosine of latitude before performing the analysis. Z can be written as a sum of the products of EOFs e_i and principle component (PC) time series y_i:

$$Z = \sum_{i=1}^{r} y_i e_i^T, \tag{3.15}$$

where r is the rank of Z, e_i is a p-vector (spatial pattern) and y_i is a n-vector (time series of centered anomalies). The time series y can also be obtained from the spatial pattern e by projecting the data onto the spatial pattern:

$$y = \frac{ZWe}{e^T We}, \tag{3.16}$$

where W is a p-vector with elements a_i proportional to the area of each grid box.

According to Baldwin and Thompson (2009), the method used to calculate the NAM index in this work is based on daily averaged, zonally averaged geopotential height $\overline{Z}$. The daily zonal mean NAM is given by the PC time series $\overline{y}$ and the EOFs $\overline{e}$ are a function of latitude only.

3.3.2 Stratospheric warmings

For the detection of stratospheric warmings, daily, zonal mean temperature and zonal wind data is used. We focus on major stratospheric warmings (MSWs), as they are the strongest manifestation of stratosphere-troposphere coupling (cf. Section 2.2.3).

In simulations and reanalysis, MSWs are identified by a reversal of zonal mean zonal wind, i.e. form westerly to easterly, at 10 hPa and 60° N, and a simultaneous reversal of the zonal mean temperature gradient between 60° N and 90° N, in order that T(60° N) $<$ T(90° N) (Labitzke, 1981). Two major warmings are separated by at least 20 days of westerlies and, in order to rule out final warmings, events that are not succeeded by at least 10 days of westerlies are not taken into account.

3.3.3 ENSO index and composites

The variability of ENSO can be described by a multitude of atmospheric and oceanic indices. In this thesis, the commonly used monthly mean Niño 3.4 index is chosen. It is described by the SST averaged over the region between 120°W - 170°W and 5° S - 5° N. The long term mean is subtracted and the data is standardised, so that the anomalies are expressed as standard deviations. Months are classified as strong El Niño events (warm ENSO, wENSO) and La Niña events (cold ENSO, cENSO) when this index exceeds one standard deviation. The index was calculated with ERA-Interim and CMIP6 SST data.

The stratospheric and tropospheric ENSO composites are based on the Niño 3.4 index. As the main focus lies on winter (DJF), the composites are generated depending on the Niño 3.4 index in the winter months. This usually coincides with the peaking strength of El Niño events. A winter is described as wENSO, when the index in at least one winter month exceeds one standard deviation. To ensure that the whole winter is influenced by warm ENSO, the other winter months are required to exceed 0.5 standard deviations. The same accounts for cENSO, with -1 and -0.5 standard devaluations, respectively. Independent of the SST data set, with this method 8 winters are classified as wENSO (1982/83, 1986/87, 1991/92, 1994/95, 1997/98, 2002/03, 2009/10, 2015/16) and 6 winters as cENSO (1984/85, 1988/89, 1998/99, 1999/2000, 2007/08, 2010/11). With the ensemble approach of the ICON experiments there are 40 wENSO winters and 30 cENSO winters.

3.3.4 Bias and error estimation

The bias and error calculations in this work are based on the difference of the respective climatologies and not single runs or years. In doing so, it is ensured that model errors are accounted for instead of the internal variability of the model or the climate system.

The root mean square error (RMSE) is a common measure of the error of a model in predicting quantitative data. In our case, this measure is used to evaluate the error of the ICON simulations compared to the ERA-Interim reanalysis. The RMSE is defined as:

$$RMSE = \sqrt{\sum_{i=1}^{n} \frac{(\overline{x_i} - \overline{y_i})^2}{n}}, \tag{3.17}$$

where $\overline{x_i}$ and $\overline{y_i}$ are the monthly mean climatological fields of a variable of the model or the reanalysis. The number of observations n is the ensemble size, which is 5 for all experiments. After calculating the different RMSEs for the experiments, spatial mean RMSEs, e.g. the zonal mean or field mean, are determined.

3.3.5 Statistical significance

The statistical significance is assessed with a two-sided Wilcoxon-test (Bauer, 1972; Hollander et al., 2013). Reference calculations with the Student's t-test showed very comparable results. However, the Wilcoxon-test is non-parametric and therefore is independent of the distribution of the analysed data. The null hypothesis states that there is no relationship between the two variables being studied and thus the results are due to chance. If not denoted otherwise, statistical significance is attributed at a p-value smaller than 0.05. This value indicates strong evidence against the null hypothesis, as there is less than a 5% probability that the null hypothesis is correct. For the comparison of ICON simulation to the reanalysis or different ICON experiments to each other, a two sample test is applied. An exception to this is the one sample test for the analysis of the NAM index.

4 Results

4.1 Evaluation of seasonal experiments with ICON-NWP

This section will evaluate if ICON is able to realistically simulate the stratospheric vortex and its variability (RQ1). Therefore, the default ICON climatology ICON$_{ctl}$ will be analysed. As stated in the research question the main focus lies on the analysis of stratospheric dynamics. Nevertheless, tropospheric circulation patterns and model biases are also of great importance for seasonal predictions. Furthermore, the stratosphere can not be regarded as as stand-alone system, as troposphere and stratosphere are coupled and therefore influence each other. Hence, in the first part of this section, tropospheric circulation in ICON will be discussed, the second part deals with the stratospheric circulation and variability.

4.1.1 Tropospheric circulation

An atmospheric model should be able to reproduce the dominant patterns of extratropical variability in the Northern Hemisphere. Especially a correct representation of the leading pattern is important, as it represents the NAM, which is the strongest pattern of atmospheric variability for the extratropical Northern Hemisphere. As described in Section 3.3.1, the NAM in this thesis is expressed by the first EOF of daily zonally-averaged 1000 hPa surface geopotential calculated over the domain poleward of 20° N. This is displayed in Figure 4.1 (a,c) for the ICON control experiment ICON$_{ctl}$ and the ERA-Interim reanalysis. Furthermore, the first EOF of 500 hPa geopotential is shown (b,d).

The leading pattern of ERA-Interim exhibits the typical features of the NAM, with its centres of action in the Atlantic and Pacific at approximately 40° N and the Arctic centre with a maximum amplitude in the Icelandic region (cf. Fig. 4.1 c). The NAM pattern explains 50% of the variance in the reanalysis. The ICON ensemble is able to realistically represent the surface NAM with its three centres of action and an explained variance of 52.9% (cf. Fig. 4.1 a). The Atlantic and Arctic pattern closely resemble the reanalysis. However, the amplitude of the Pacific centre of action is overestimated in ICON.

The reconstructed leading EOF patterns of daily zonally-averaged 500 hPa geopotential height are similar to NAM surface patterns. With decreasing effects of surface dissipation in the mid troposphere, the centres of action start to expand over the continents. Once more, ICON is able to reproduce the characteristic patterns. The explained variance of 49.6% is

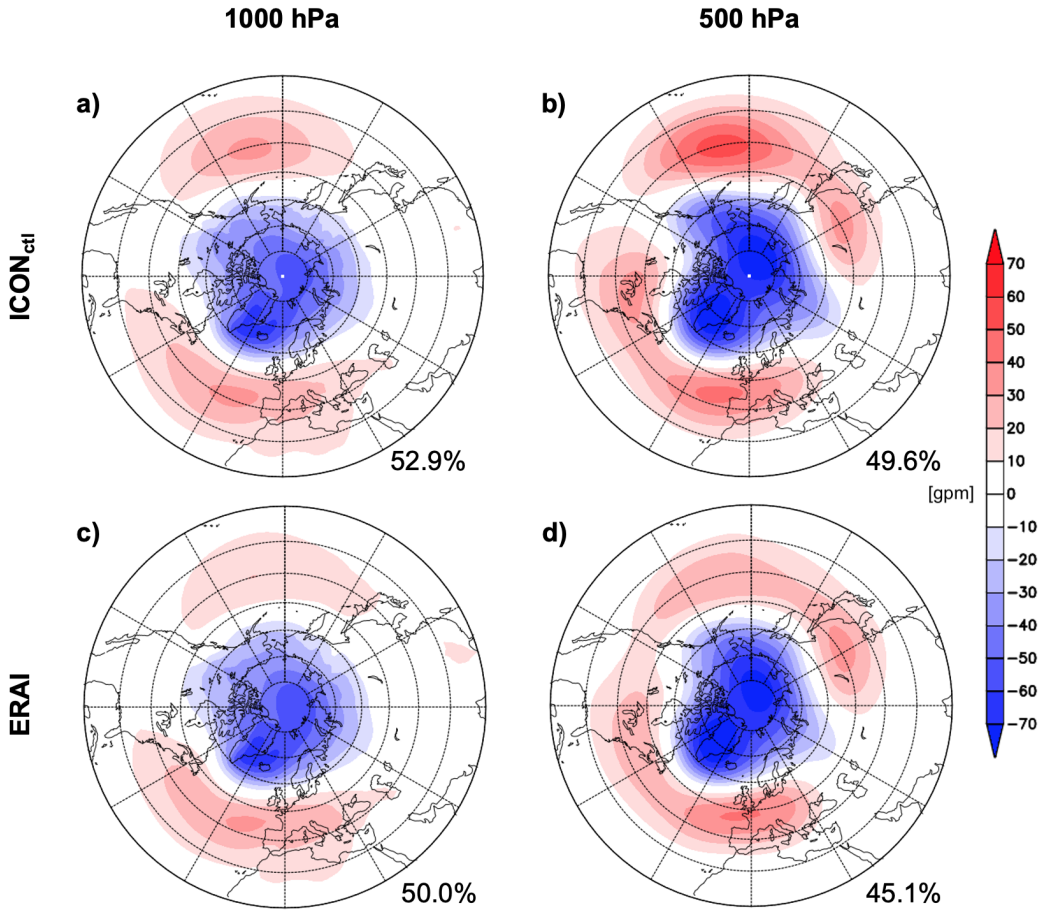

Fig. 4.1.: Reconstructed leading EOF patterns of daily zonally-averaged 1000 hPa (a,c) and 500 hPa (b,d) geopotential height during October-April 1979/80-2016/17 period on a polar stereographic projection showing values north of 20° N. Patterns of ICON$_{ctl}$ ensemble in a and b, patterns of ERA-Interim reanalysis in c and d. The explained variance is given in the bottom right corner of the respective figure.

slightly overestimated compared to 45.1% of ERA-Interim. As in 1000 hPa, the Pacific centre of action is overestimated by ICON, a feature, which is present in all vertical levels of the troposphere.

The EOF patterns 2-5 are also realistically represented in ICON. The second EOF pattern is given exemplary in Figure A.1 of the appendix. The patterns are well represented by ICON, however, the amplitude of the Pacific centre of action seems to be overestimated once more. Due to the zonally-averaged approach, the first 5 EOF pattern are accountable for 96.6% (ERA-Interim) and 96.1% (ICON) of the explained variance and therefore represent the majority of the extratropical variability. The seasonal experiments with ICON are able to reproduce the basic patterns of the zonally-averaged tropospheric variability.

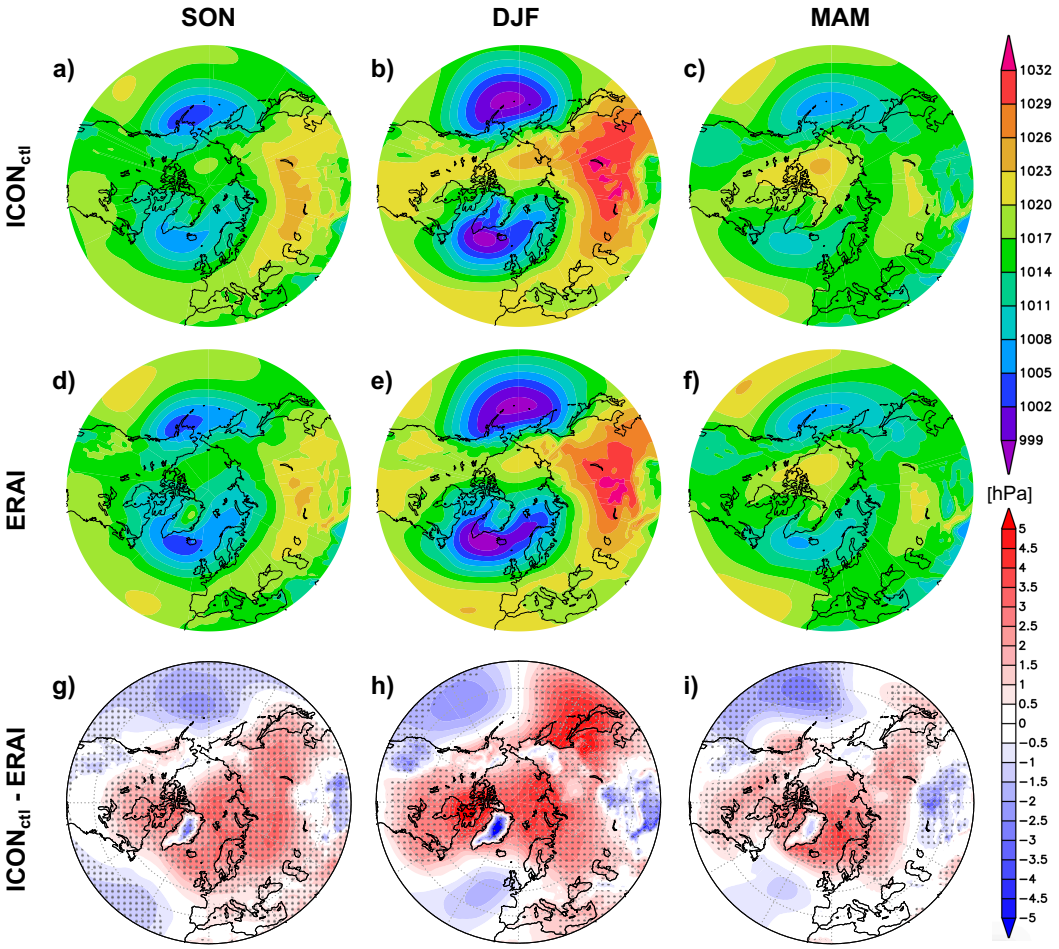

Fig. 4.2.: MSLP patterns in ICON$_{ctl}$ (a-c) and ERA-Interim (d-f) as well as MSLP bias patterns (g-i) for the seasons autumn (SON), winter (DJF) and spring (MAM). Polar stereographic projection showing values north of 30° N. Stippling in the bias patterns indicates statistical significance at the 99% level according to a two-sided Wilcoxon-test.

While the EOF patterns can give insight on the differences of the basic variability patterns, they don't exhibit quantitative model biases. Therefore it is useful to directly compare the model output variables. Figure 4.2 illustrates the mean sea level pressure (MSLP) patterns for ICON (a-c), ERA-Interim (d-f) and difference between both (g-i). The patterns and biases are shown for the simulated seasons autumn, winter and spring as long term mean over the years 1979-2017. As expected, winter exhibits the strongest MSLP contrasts between continental high pressure areas and maritime low pressure areas. This behaviour is successfully reproduced by ICON. The Icelandic and Aleutian low pressure systems are simulated at the right locations, with patterns closely resembling the reanalysis. The same accounts for the pronounced winterly Siberian high pressure system. However, in particular in autumn, the Icelandic low and the Azores high seem to be underestimated in ICON, which is an indication for a weak NAO.

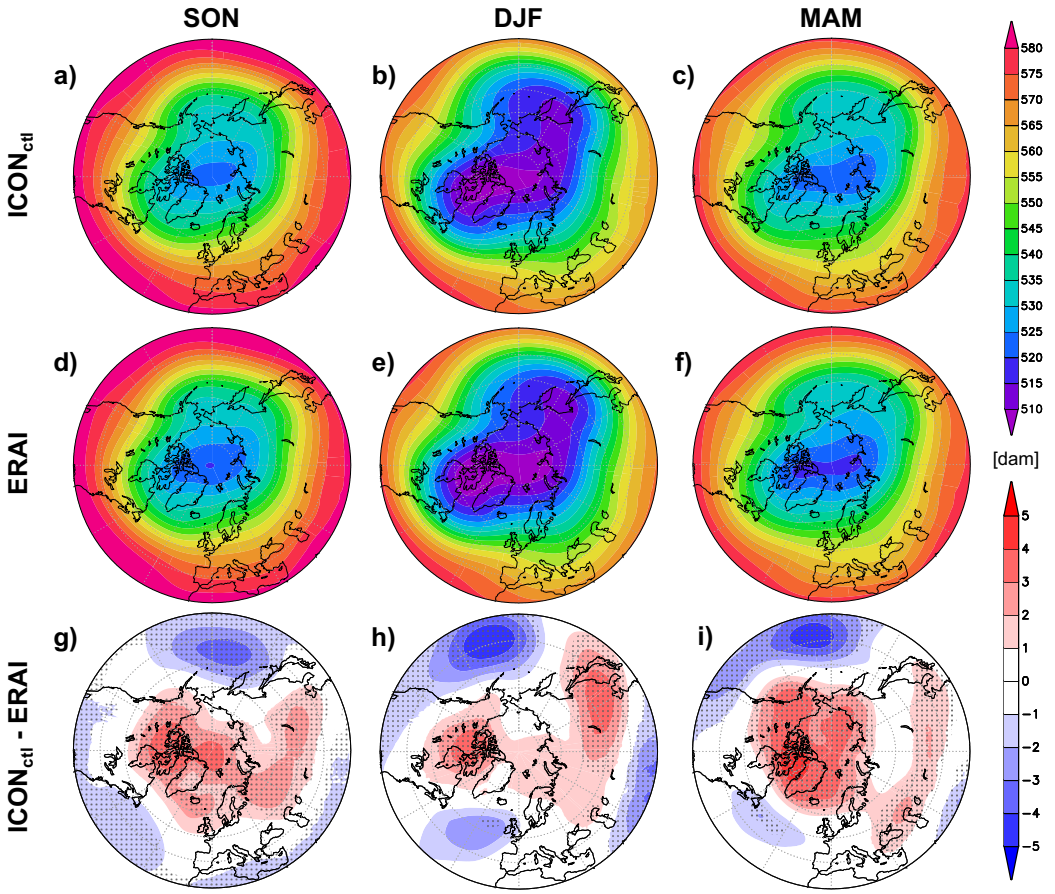

Fig. 4.3.: Geopotential height in 500 hPa in ICON$_{ctl}$ (a-c) as well as the geopotential height in 500 hPa bias (d-f) for the seasons autumn (SON), winter (DJF) and spring (MAM). Polar stereographic projection showing values north of 30° N. Stippling in the bias patterns indicates statistical significance at the 99% level according to a two-sided Wilcoxon-test. The geopotential height is given in decametres (dam).

The actual differences between the ICON simulation and the reanalysis manifest in the bias figures 4.2 (g-i). This pattern is described by high pressure anomalies in the Arctic and low pressure anomalies in lower latitudes. A constant large-scale pattern, which resembles the negative phase of the AO, dominates the ICON bias in all seasons. Both are indicators for a weakened westerlies. In winter the biases are amplified and highly significant. Largest positive biases are visible over the Arctic region and over the Sea of Okhotsk. Negative biases are largest in the eastern North Pacific.

Figure 4.3 depicts ICON absolute values and bias of geopotential height in 500 hPa for the different simulated seasons. The geopotential height pattern is dominated by the tropospheric large-scale polar low pressure system, which has its lowest values in the central Arctic. Compared to the MSLP patterns, a reduction of the orographic influence is visible, as the patterns become more zonally symmetric. Nevertheless, especially in winter, when the polar vortex is strongest, there is still a shift of low geopotential heights towards the

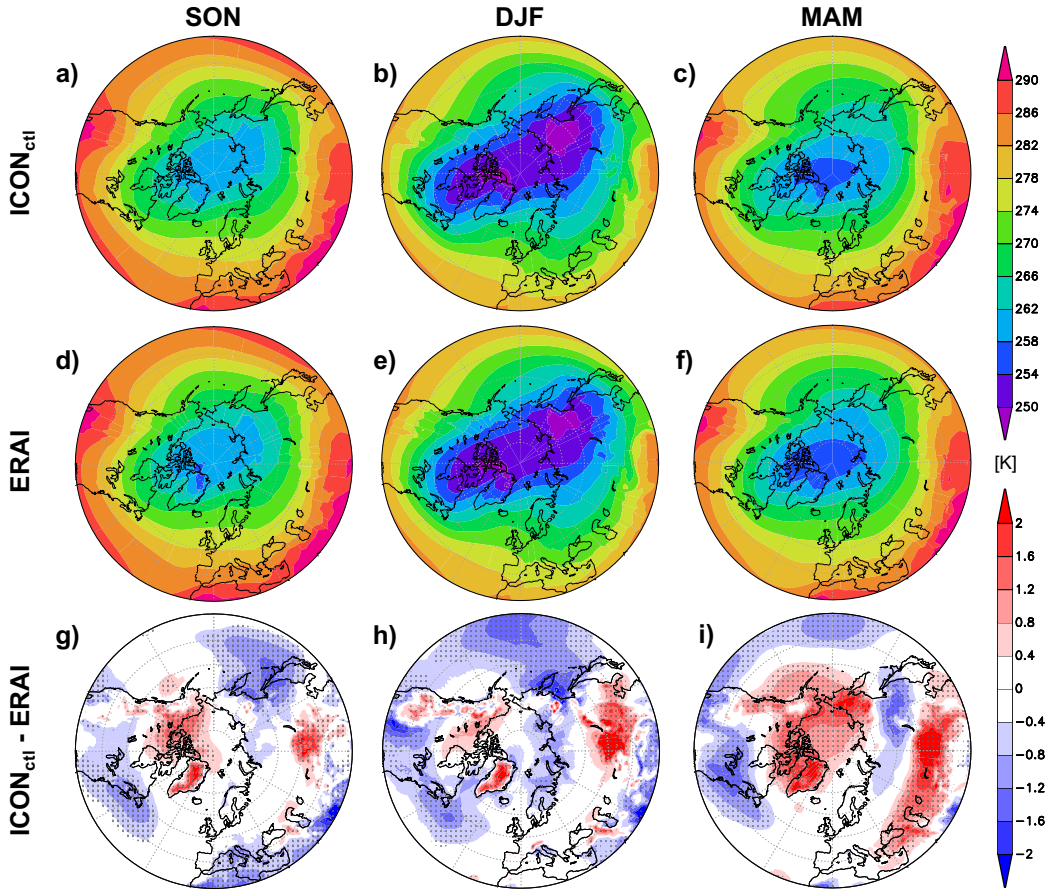

Fig. 4.4.: Temperature in 850 hPa in ICON$_{ctl}$ (a-c) as well as the according bias patterns (d-f) for the seasons autumn (SON), winter (DJF) and spring (MAM). Polar stereographic projection showing values north of 30° N. Stippling in the bias patterns indicates statistical significance at the 99% level according to a two-sided Wilcoxon-test.

oceans. The bias patterns (d-f) are rather uniform over the three seasons and resemble the bias patterns in the MSLP, with positive anomalies in high latitudes and negative anomalies in lower latitudes, especially over the Pacific and Atlantic. However, in 500 hPa the areas of highly significant biases are slightly smaller. Once more there is strong significant bias in the Northern Pacific, which coincides with overestimated Pacific centre of action from the EOF analysis. The positive geopotential height bias in the central Arctic is strongest in spring and, in contrast to the MSLP bias, weakest in winter.

To further investigate tropospheric behaviour in ICON, the temperature patterns in 850 hPa are analysed (cf. Fig. 4.4). The 850 hPa height is commonly chosen for the analysis of temperature fields as it represents near surface conditions, but is less influenced by local topographical features. Furthermore, in contrast to the 2 m temperature, it is a prognostic model variable. The ICON temperature patterns agree well with the simulated pressure patterns. The insolation minimum in winter in the high latitudes creates low tropospheric

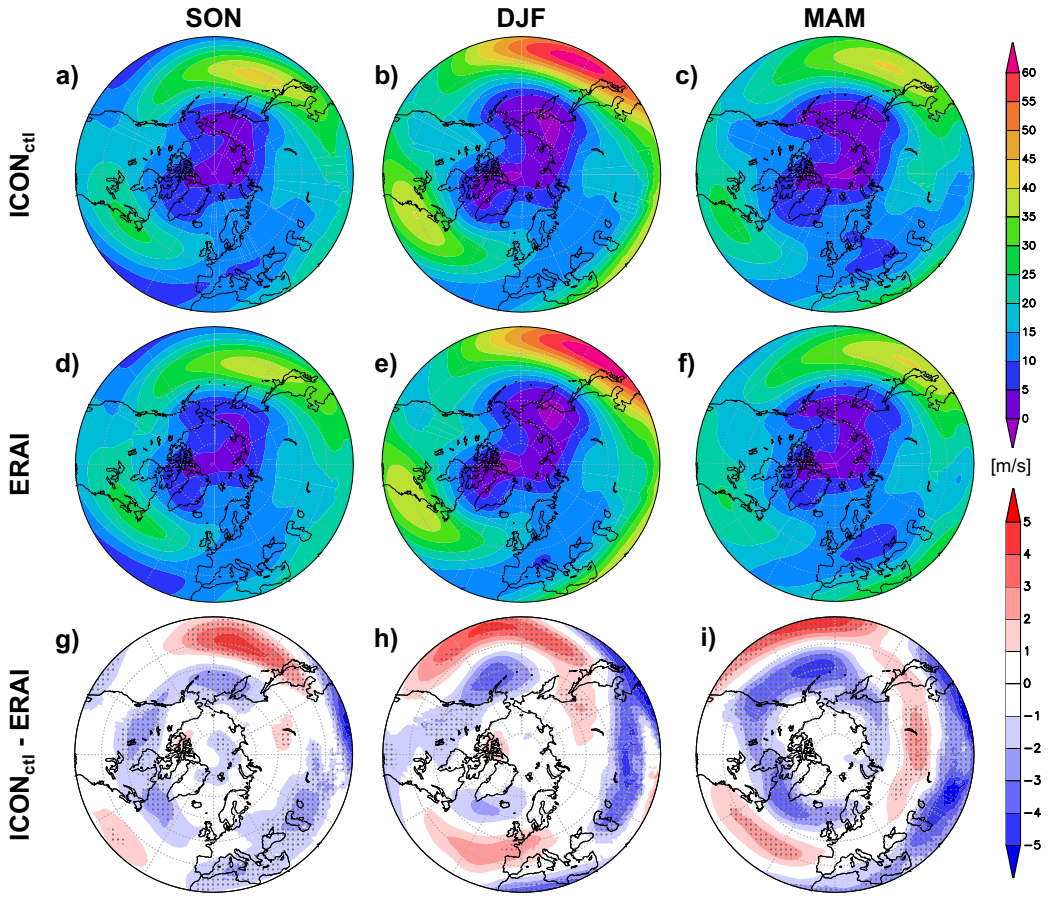

Fig. 4.5.: Zonal wind in 300 hPa in ICON$_{ctl}$ (a-c) as well as the according bias patterns (d-f) for the seasons autumn (SON), winter (DJF) and spring (MAM). Polar stereographic projection showing values north of 30° N. Stippling in the bias patterns indicates statistical significance at the 99% level according to a two-sided Wilcoxon-test.

temperatures in the region of the polar low pressure system. The absolute temperature minima are simulated in the region of the Canadian Archipelago and in eastern Siberia, with mean winter temperatures below 250 K. These basic temperature patterns agree well with the ERA-Interim reanalysis. Nevertheless, there are some significant differences between ICON and the reanalysis (cf. Fig. 4.4 d-f). The significant negative temperature biases in the central and western Pacific are connected to the negative pressure anomalies in the central and eastern Pacific and are a consequence of advection of cold Arctic air masses. Furthermore there is a consistent underestimation of temperatures in eastern North America. Whereas there is no clear temperature bias in the central Arctic in autumn and winter, positive pressure biases in spring are connected to significant positive temperature biases.

The zonal wind in 300 hPa height is commonly used to analyse the strength and position of the jet stream. Figure 4.5 illustrates the ICON 300 hPa zonal wind patterns and biases. The NH large-scale circulation is dominated by westerlies. These are particularly strong in

winter, a feature that ICON reproduces realistically. This large-scale circulation is driven by the differential heating rates from incoming solar radiation between the equator and the poles. Especially polar night creates a strong imbalance, which is compensated for by heat transport from the tropics towards the poles. The Coriolis force deflects poleward winds eastward, thereby initiating the westerly circulation (cf. Section 2.1.2). The actual meridional transport is then mainly a consequence of growing baroclinic instabilities (cf. Section 2.1.3). Strongest westerlies in ERA-Interim and ICON are visible in the western Pacific and Atlantic, with maximum amplitude east of Japan where a merging of the polar jet with the subtropical jet can lead to an intensification of the westerly flow. The bias patterns are similar in the three seasons. The areas of maximum zonal winds are climatologically shifted south-east in ICON. The westerlies circulating around the pole are too weak, which is in line with the weak tropospheric polar low pressure system and thus a consequence of a reduced meridional pressure gradient in ICON. How this reduced pressure gradient is associated with the sub-grid scale orography scheme, will be discussed in Section 4.2.

The basic NH circulation patterns are realistically represented in all three seasons. Biases are largest in winter and spring, in particular in the Arctic and northern Pacific. For most variables and levels the bias over Europe is small or not significant. This comes as no surprise, as it is the main goal of the ICON developers to have realistic weather predictions over Europe. However, the seasonal experiments also show, that biases over Europe do not largely accumulate over a seasonal time scales, which is a promising result for future seasonal predictions.

4.1.2 Stratospheric circulation

The stratospheric polar vortex is the dominant feature of the NH stratosphere in winter (cf. Section 2.2). The zonal mean zonal wind at 60° N in 10 hPa is a good proxy for the strength of the vortex, which is furthermore used for the identification of stratospheric sudden warmings (cf. Section 2.2.3). Figure 4.6 depicts the zonal mean zonal wind at 60° N in 10 hPa for the ERA-Interim climatology and the ICON$_{ctl}$ climatology, which includes five ensemble members. The polar vortex evolution can be separated into three phases: The formation of the vortex in autumn with intensifying westerlies and weak variability (first phase). In the second phase the peaking vortex strength in early winter is connected to intensified vertical propagation of planetary waves and subsequent wave breaking, leading to a more frequently disturbed and variable polar vortex. Depending on the intensity of vertical wave propagation, January can be the month with peak zonal mean zonal winds, but also can be characterised by vortex breakdowns and reversals. The third phase in spring is characterised by declining vortex strength and variability, and, following the final warming, the transition to weak summer easterlies connected to the stratospheric high pressure system in summer.

ICON is able to reproduce the climatological characteristics of the different vortex phases, additionally the standard deviation and extreme values are in a realistic range. Nevertheless, there are some distinct differences: The mean stratospheric polar vortex strength in ICON$_{ctl}$

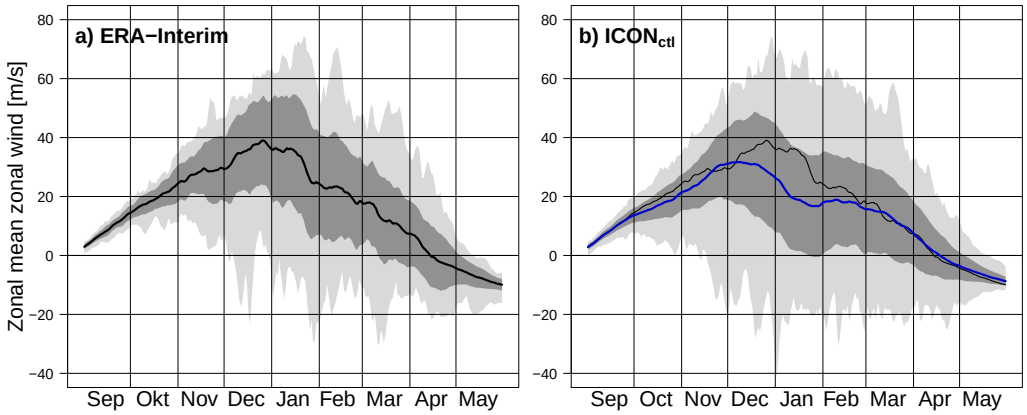

Fig. 4.6.: Zonal mean zonal wind at 10 hPa and 60° N (lines), standard deviation (dark grey shading) and extrema (light grey shading) for 1979/80 - 2016/17 period of ERA-Interim (a) in black and ICON$_{ctl}$ (b) in blue. Positive (negative) values indicate westerly (easterly) circulation.

is underestimated in winter. This especially accounts for January, where the monthly mean zonal mean zonal wind in 10 hPa and 60° N is considerably weaker than in ERA-Interim. Furthermore, the strength of the polar vortex in October and early November is slightly underestimated, whereas the vortex strength is simulated well in spring.

The weak winterly stratospheric vortex is also visible in the polar stereographic projection of the zonal wind in 10 hPa. The monthly mean values from ICON$_{ctl}$ and the biases to ERA-Interim are depicted for the winter months in Figure 4.7. Although the stratospheric polar vortex is climatologically shifted towards Europe, there is constant westerly flow at the 60° N latitude. Thus, the zonal mean zonal wind at 60° is a useful proxy of the strength of the vortex and Figure 4.7 strengthens the impressions gained from Figure 4.6. The polar vortex in ICON is strongest in December and slowly weakens in the course of winter due to increased wave braking. The zonal wind patterns are in agreement with ERA-Interim, however, in particular in January, there are some significant differences in the amplitude. Already in December the vortex strength is underestimated, especially in the outer margins of the vortex. Largest biases are evident in January, where the strength of the entire vortex is underestimated significantly. The easterly circulation above the Pacific, which is caused by the Aleutian high pressure system, is also underestimated in ICON. In February the biases in the area of the polar vortex are reduced, but positive biases in lower latitudes are increased. The weak polar vortex is connected a significant positive temperature bias in high latitudes in December and January, followed by a negative temperature bias in February (not shown).

To avoid biases with a positive and a negative sign cancelling each other out in the monthly mean, it is useful to also investigate the daily evolution of the vortex dynamics. As bias patterns in the stratosphere are usually zonally symmetric, an analysis of a field mean over certain latitudes and longitudes can be reasonable. The stratosphere north of 65° N is always influenced by the polar vortex in winter. Strong westerlies and cold temperatures will dominate in a strong vortex scenario, whereas a weak, shifted or disrupted vortex will

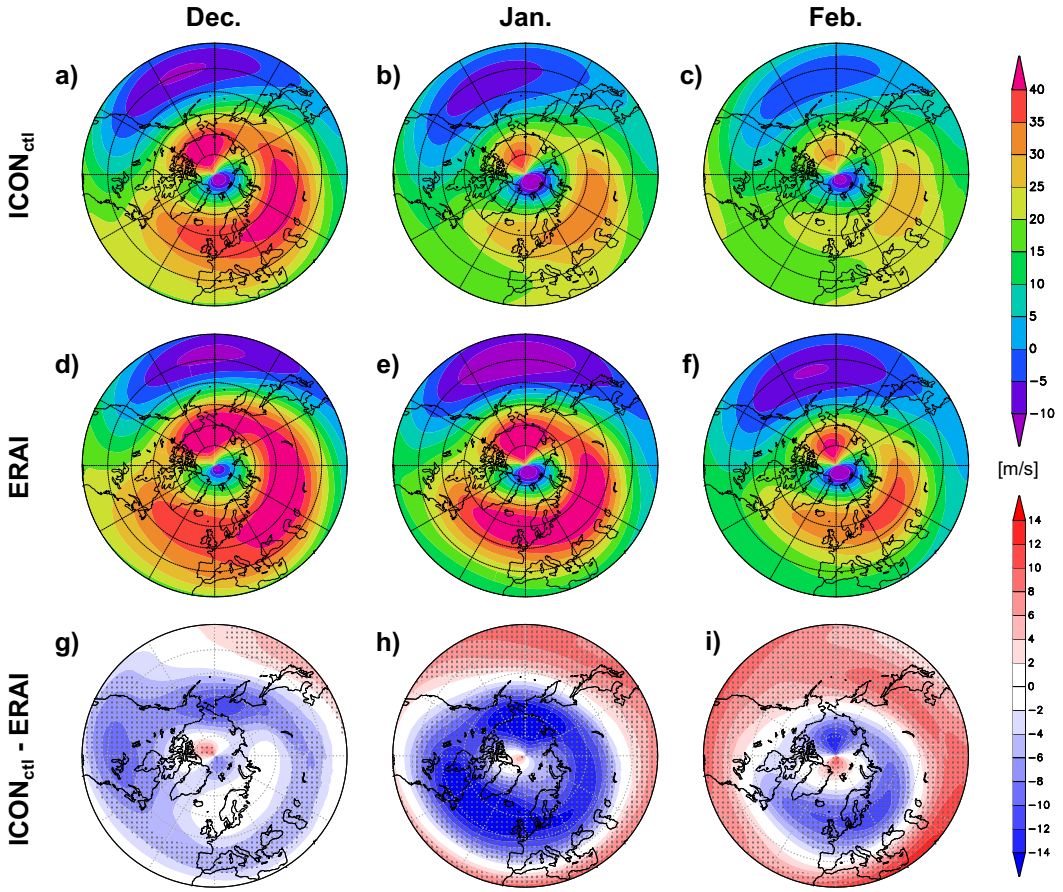

Fig. 4.7.: Zonal wind in 10 hPa in ICON$_{ctl}$ (a-c) as well as the according bias patterns (d-f) for the months December, January and February. Polar stereographic projection showing values north of 30° N. Stippling in the bias patterns indicates statistical significance at the 95% level according to a two-sided Wilcoxon-test.

lead to weaker westerlies or even easterlies and warmer temperatures. Hence, the polar cap mean (PCM) zonal wind or temperature precisely reflect the strength of the vortex. Furthermore, the PCM enables a depiction of the daily evolution over all vertical levels.

The bias for the PCM zonal wind and temperature of ICON compared to ERA-Interim is visible in Figure 4.8. The PCM is defined as the field mean from 65.25° N to 90° N and is strongly influenced by the strength and position of the polar vortex. The mean stratosphere of ICON$_{ctl}$ is dominated by a negative wind bias in the high latitudes, and especially in January this is large and highly significant (cf. Fig. 4.8 a). The strong January bias is preceded by a highly significant and downward propagating negative zonal wind bias in October and November. Contrary to the dominant negative bias in the mid stratosphere, the upper stratosphere is dominated by significant positive wind bias in November, early December, February and March. The temperature bias is less clear, as the PCM temperature already reacts to small changes of the vortex position and is also influenced by radiative effects. The cold bias in the tropopause, for instance, can be explained by an overestimated

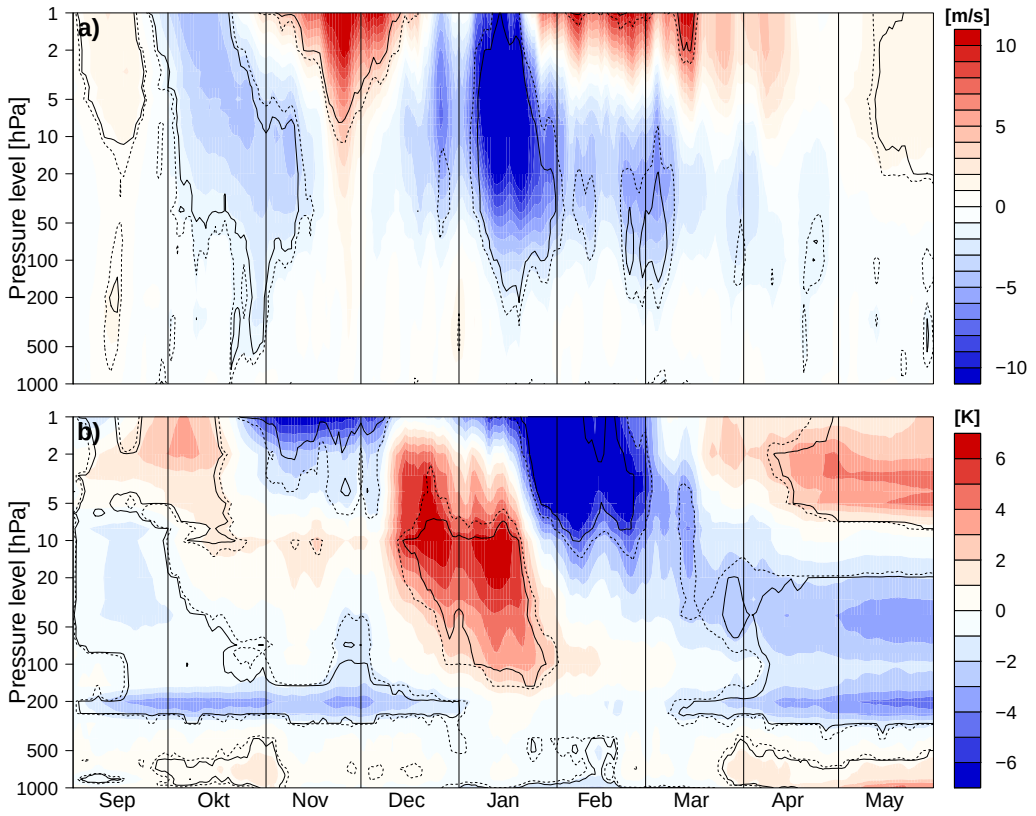

Fig. 4.8.: Time-height cross section of climatological mean zonal wind (a) and temperature (b) differences for the polar cap mean (65.25°N to 90°N). ICON$_{ctl}$ biases to ERA-Interim. Dashed/solid lines indicate statistical significance at the 95/99% level according to a two-sided Wilcoxon-test.

longwave cooling due to an overestimation of water vapour in the tropopause region in this model version. The strongest biases are once again visible in late December and January, when the positive temperature biases are directly linked to the weak vortex. The positive bias pattern has its origins in the upper and mid stratosphere in December and propagates downward to the lower stratosphere in January. It is followed by a negative temperature bias in the upper stratosphere in February. This feature corresponds to a pattern typical for downward propagating signals in the stratosphere. The warm bias in the troposphere in spring was already visible in Figure 4.4 f. The mid and lower stratosphere are dominated by negative temperature bias in spring, whereas the upper stratosphere is dominated by negative temperature bias.

In accordance with the underestimated vortex strength, the frequency of MSWs is overestimated by ICON$_{ctl}$ in all relevant months except for February. However once again, January stands out with on average 4 MSWs per decade compared to 1.58 for the reanalysis (cf. Fig. 4.9). The range of the five ensemble members is given by the grey error bar. January is the only month, where the ensemble range does not meet the reanalysis. All five ensemble member largely overestimate the frequency of MSWs in January. Stratospheric warming

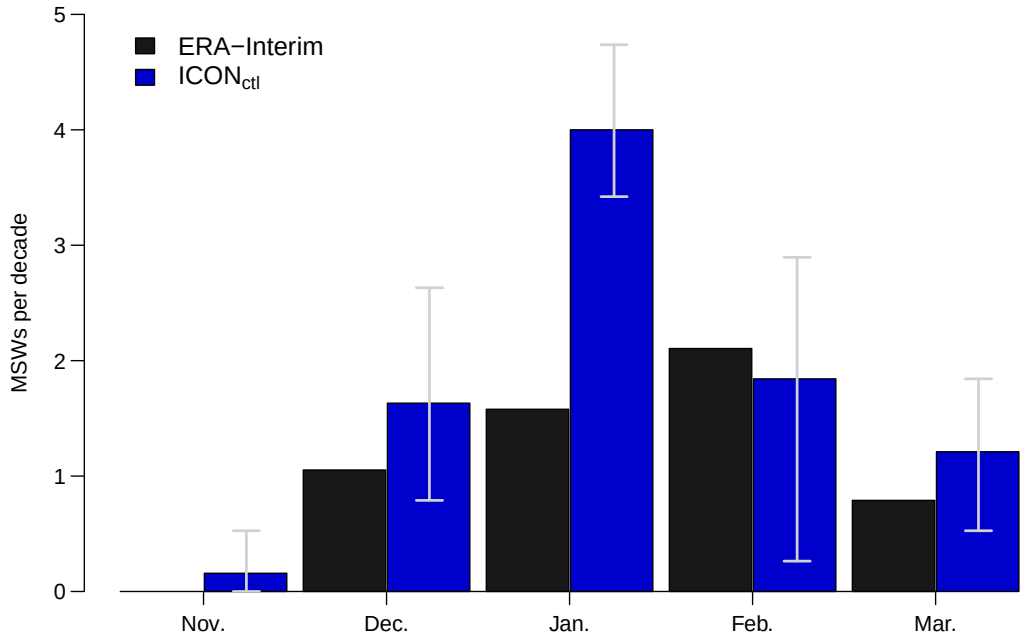

Fig. 4.9.: MSWs per decade and month (November - March) for ERA-Interim (black) and ICON$_{ctl}$ (blue). The spread of the ICON$_{ctl}$ ensemble members is given by the light grey error bar. MSWs are identified by a reversal of the zonal mean zonal wind in 10 hPa and 60°N and a simultaneous reversal of the temperature gradient between 60°N and 90°N (cf. Section 3.3.2).

events are driven by the nonlinear breaking of upward-propagating planetary waves (cf. Section 2.2.3). High vortex breakdown frequencies can be an indicator of an overestimated upward propagation of planetary waves. In addition, MSWs are the strongest manifestation of the stratosphere to troposphere coupling. Different studies have shown that stratospheric warmings precede increased geopotential in the Arctic and negative anomalies in the mid-latitudes, a signal associated with the negative phase of the Arctic oscillation (i.e. Charlton and Polvani, 2007; Cohen and Jones, 2011; Sigmond et al., 2013).

An earlier study has described that the stratospheric polar vortex in ICON-A exhibits similar features to the ones described in this section: Borchert et al. (2019) state that stratospheric winter westerlies are too weak in ICON and suggest a retuning of orographic and non-orographic gravity wave drag parameters. In the following section, the retuning of the mentioned parameters in ICON-NWP will be discussed.

4.2 Effect of gravity wave drag parameterisations

Polichtchouk et al. (2018b) suggest that the non-orographic gravity wave drag is a tuneable parameter for obtaining a more realistic MSW behaviour in models. Moreover, a reduced non-orographic gravity wave drag leads to a reduction in the MSW frequency. Taking into account the results from Section 4.1.2, these hypotheses are tested with the goal of reducing the amount of MSWs, thereby stabilising the winterly stratospheric vortex in ICON-NWP. Therefore, the non-orographic gravity wave drag is reduced by 20% in ICON$_{nogwd-}$. The orographic wave drag, on the other hand, is a tuneable parameter as part of the SSO scheme. With the goal of strengthening the stratospheric polar vortex, the orographic gravity wave drag constant is reduced by 20% in a further experiment named ICON$_{sso-}$. As the seasonal experiments with ICON$_{ctl}$ indicated a MSLP pattern which can be described as "highs too low, lows too high" (cf. Section 4.1.1), not only the gravity wave drag constant is adjusted, but also the low level wake drag constant and the critical Froude number (cf. Table 3.2). As described in Section 3.1.2 the third sensitivity experiment ICON$_{gwd-}$ combines both adjustments to an overall reduced gravity wave drag. All sensitivity experiments are compared to ICON$_{ctl}$ as well as the ERA-Interim reanalysis.

The effects of the adjusted gravity wave drag parameterisations are divided into three sections. In the first part, the direct effects of the adjusted gravity wave drag on the stratosphere will be discussed, the second part will focus on changes in the stratosphere-troposphere coupling and the third part will describe how the tropospheric circulation is influenced directly via the SSO scheme and indirectly via stratosphere-troposphere coupling. The results of this section are based on the paper "Improved Stratospheric Circulation Due to Changes in the Gravity Wave Drag Parameterisations in ICON-NWP" by Köhler et al., which is currently under review at the Journal of Advances in Modeling Earth Systems (JAMES).

4.2.1 Stratospheric effects

The zonal mean zonal wind in 10 hPa and 60° N is a good measure for the strength of the stratospheric polar vortex (cf. Section 4.1.2). Analogous to Figure 4.6, Figure 4.10 exhibits the zonal mean zonal wind as well as its standard deviation and extrema for the three sensitivity experiments ICON$_{nogwd-}$ (a), ICON$_{sso-}$ (b) and ICON$_{gwd-}$ (c). The zonal mean values are also given for ICON$_{ctl}$ and ERA-Interim for comparison. For the standard deviation and extrema of the control experiment and the reanalysis, please refer to Figure 4.6.

The three sensitivity experiments exhibit a realistic evolution of the stratospheric polar vortex, with peaking vortex strength in December and maximum variability in winter. Compared to ICON$_{ctl}$, the sensitivity experiment ICON$_{nogwd-}$ with reduced non-orographic gravity wave drag exhibits a strengthened polar vortex, in particular in January. The impact of reduced SSO forcing (ICON$_{sso-}$) is less pronounced in the stratosphere, but also leads to a moderate strengthening of the polar vortex in January. The experiment with the

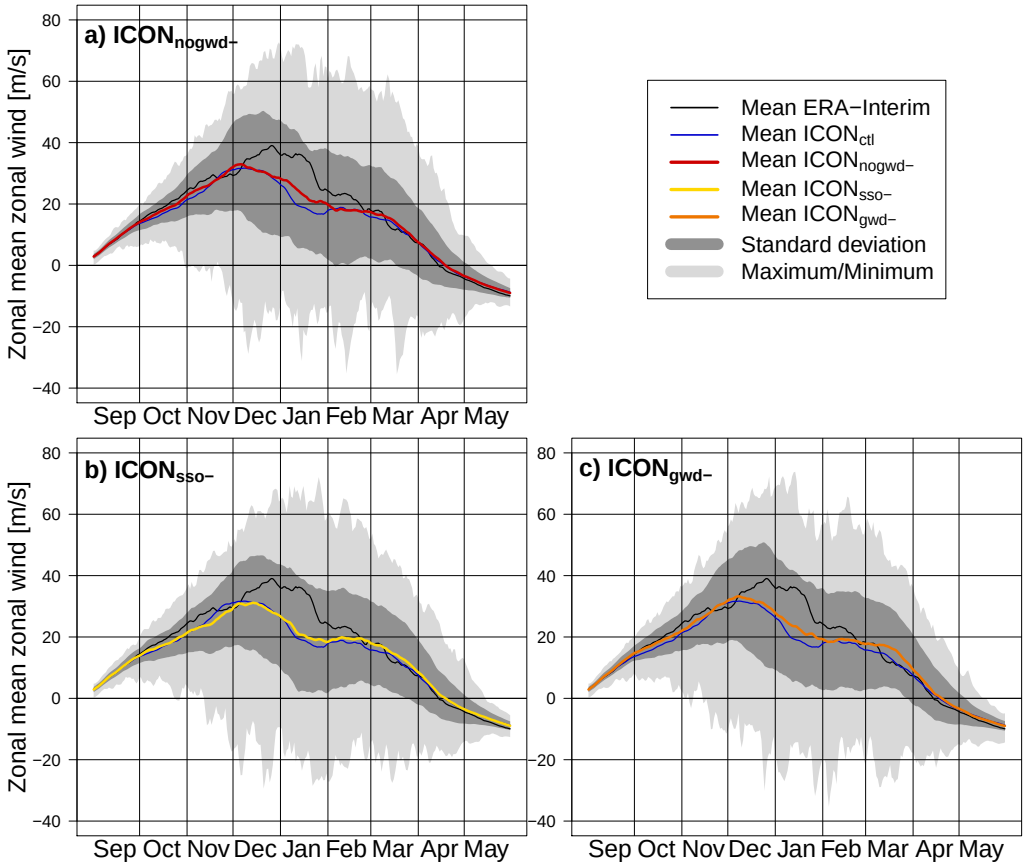

Fig. 4.10.: Zonal mean zonal wind at 10 hPa and 60° N (lines), standard deviation (dark grey shading) and extrema (light grey shading) for ICON$_{nogwd-}$ in red (a), ICON$_{sso-}$ in yellow (b) and ICON$_{gwd-}$ in orange (c). Mean values for ERA-Interim (black) and ICON$_{ctl}$ (blue) are given for comparison. Positive (negative) values indicate westerly (easterly) circulation.

combined adjusted parameterisations ICON$_{gwd-}$ strongly resembles ICON$_{nogwd-}$, suggesting a stronger impact of the non-orographic gravity wave drag on the stratosphere. Nevertheless, all experiments demonstrate that a reduction of gravity wave drag leads to a strengthening of the stratospheric polar vortex in winter. Changes in the drag parameterisations have only marginal effects on the variability and extrema of the stratospheric polar vortex. As the drag reduction leads to a vortex strengthening in winter, the sensitivity experiments match the ERA-Interim reanalysis better than ICON$_{ctl}$.

The direct effect of the altered gravity wave drag parameterisations on the PCM zonal wind is shown in Figure 4.11 by exhibiting significant differences between the sensitivity experiments and the control run. A reduction of the non-orographic gravity wave drag leads to an overall strengthening of the westerly circulation in the high latitudes. This is caused by an intensification of the stratospheric polar vortex. Largest and most significant effects are visible in the upper stratosphere in autumn and the whole stratosphere in January (cf. Fig.

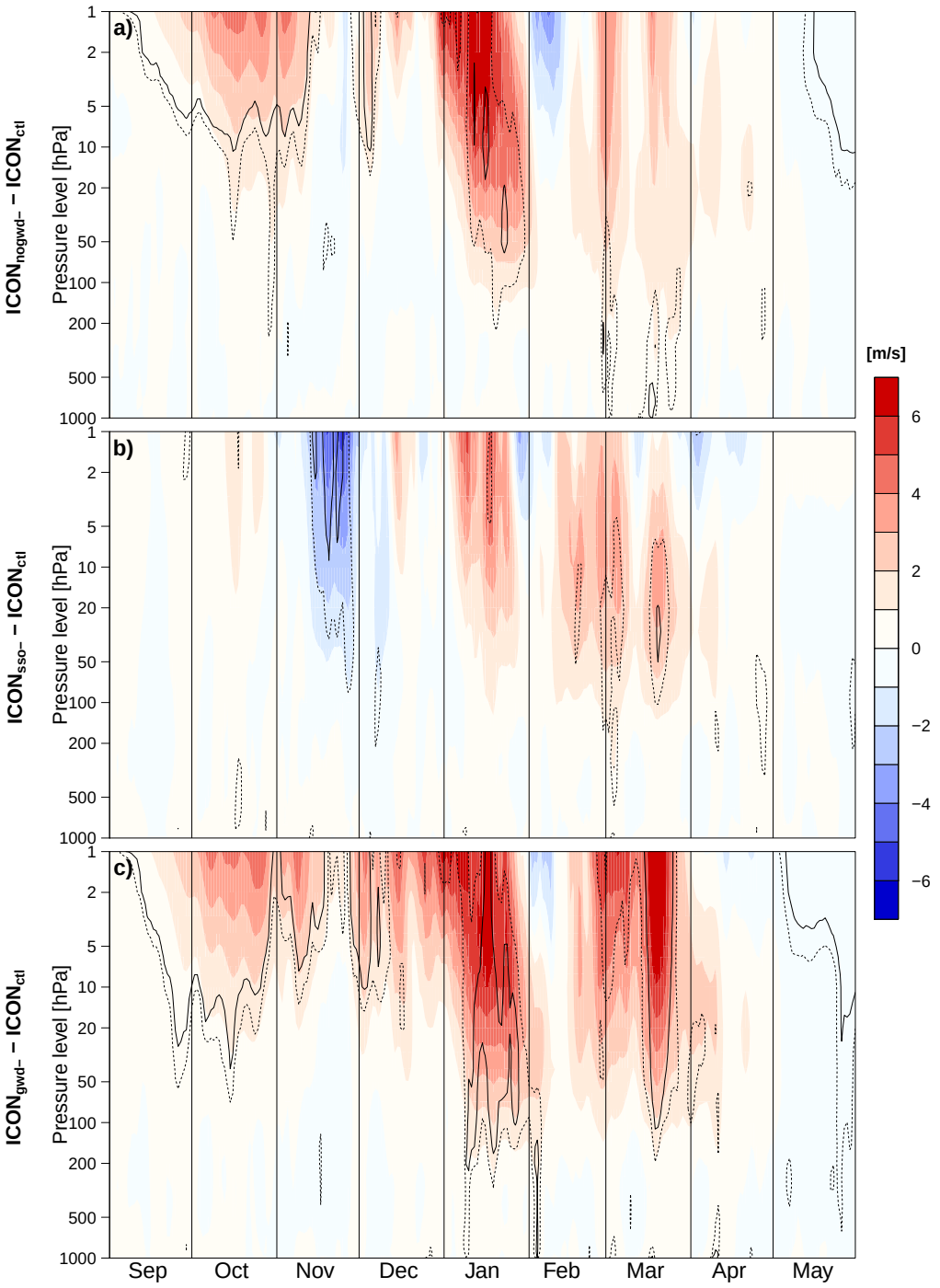

Fig. 4.11.: Time-height cross section of climatological mean zonal wind differences for the polar cap mean (65.25°N to 90°N). ICON$_{nogwd-}$ (a), ICON$_{sso-}$ (b) and ICON$_{gwd-}$ (c) differences to ICON$_{ctl}$. Dashed/solid lines indicate statistical significance at the 95/99% level according to a two-sided Wilcoxon-test.

4.11 a). Except for March, there are no significant tropospheric effects visible in the PCM. The significant strengthening of tropospheric westerlies in March could be connected to downward propagating signals from the stratosphere. The effects of the reduced orographic gravity wave drag from the adjusted SSO scheme are less pronounced and mainly confined to the mid and upper stratosphere (cf. Fig. 4.11 b). A significant weakening of the westerly circulation is visible in November and a weak strengthening in January. An intensification of westerlies in the whole stratosphere is visible in February and March. However, in total the effects from the adjusted SSO scheme on the stratospheric circulation are small. Figure 4.11 c exhibits the effects of the combined reduction of both gravity wave drags. The polar stratosphere is dominated by an intensification of the westerly circulation. This is particularly large and accounts for the whole stratosphere in January and March, whereas it is confined to the upper stratosphere from September to December. The strengthening of the westerly circulation even reaches the troposphere in January and early February. The combined effect is a quasi-additive summation of the effects of two individually adjusted parameterisations. This, however, does not account for November.

All sensitivity experiments exhibit reduced PCM zonal wind biases in the mid stratosphere of the high latitudes (cf. Fig. 4.12). This is caused by intensified westerly circumpolar circulation, as the flow is less disturbed by upward propagating waves. Whereas this effect is clear and highly significant in the experiments with reduced non-orographic wave drag, the stratospheric effects of the reduced SSO forcing is less pronounced. A reduction of the non-orographic gravity wave drag leads to an overall strengthening of the stratospheric westerly circumpolar circulation in the high latitudes of the NH. This effect is highly significant in mid-autumn and January. The combination of both adjusted gravity wave drag parameterisations leads to a strengthening of this effect. Thereby, biases are significantly reduced, especially in January. Nevertheless, the intensification of the zonal wind has negative effects on the bias of the upper stratosphere in November, December and March. Having said this, in total the bias reductions in the mid and lower stratosphere outweigh the bias increase in the upper stratosphere, as the lower stratosphere directly influences the troposphere. The positive effect of the reduced gravity wave drag on the stratospheric circulation of the high latitudes can be further quantified by calculating the polar cap mean RMSE of monthly mean zonal wind data in 10hPa for the different experiments. Compared to ICON$_{ctl}$ the error averaged over the whole simulation period is reduced by 18% in ICON$_{nogwd-}$, 11% in ICON$_{sso-}$ and 19% ICON$_{gwd-}$. In January this effect is strongest, and errors are reduced by 34%, 21% and 38% respectively. A table including the RMSEs for all months and experiments is given in appendix A.1.

Differences between the model and the reanalysis can be assessed more quantitatively with the help of the root-mean-square error (cf. Section 3.3.4). Furthermore, offsetting of biases with opposite signs can be avoided. Figure 4.13 illustrates the zonal mean RMSE of zonal wind in 10 hPa for the months September until May. Whereas the focus so far has been on the polar vortex and the high latitudes, here, effects of the changed gravity wave drag on the lower latitudes of the NH become apparent. It shows that the improved stratospheric circulation in the high latitudes is not at the expense of the simulation quality in the lower latitudes. In autumn, ICON model errors are small. This also accounts for the differences

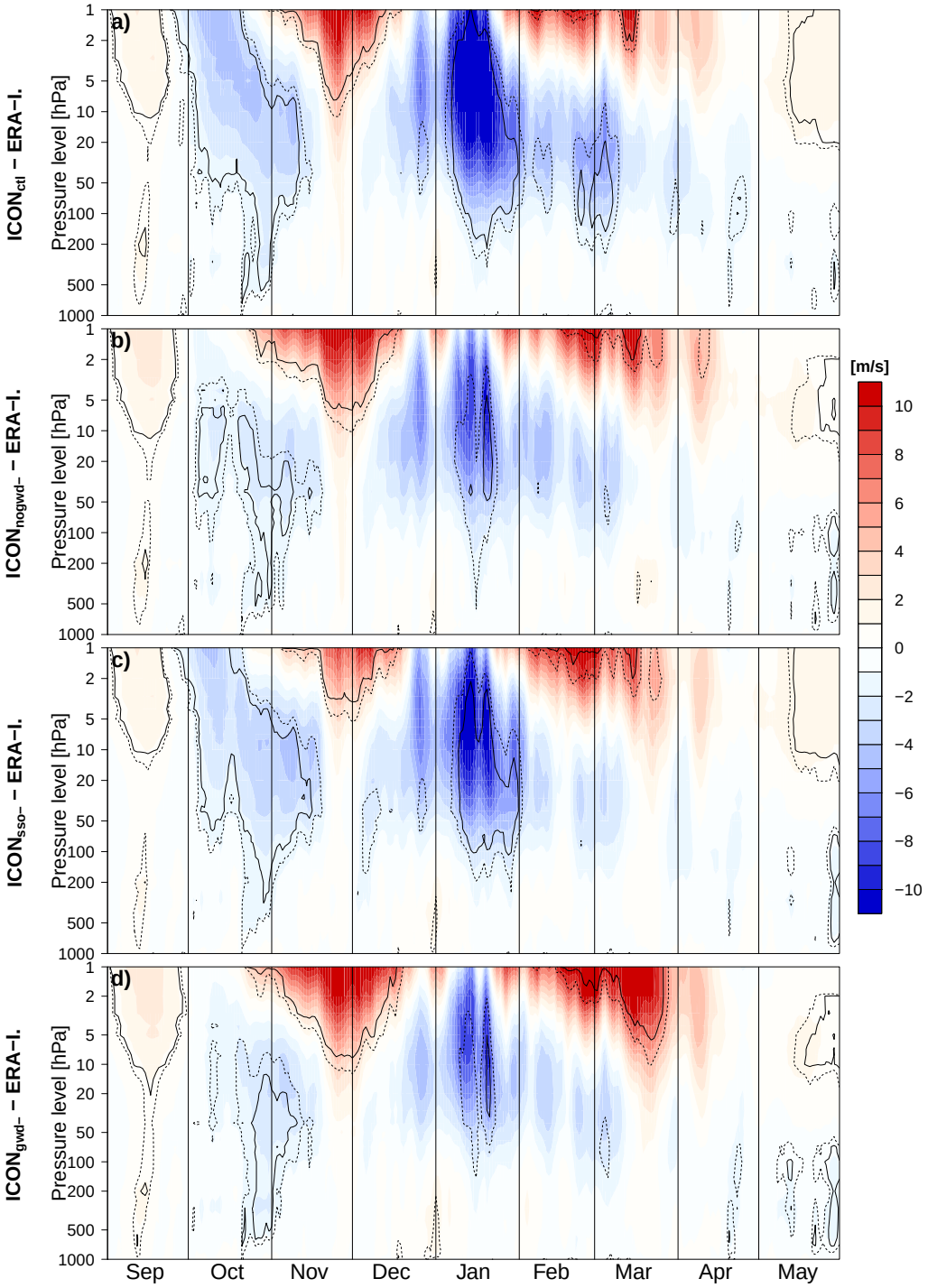

Fig. 4.12.: Time-height cross section of climatological mean zonal wind differences for the polar cap mean (65.25° N to 90° N). ICON$_{ctl}$ (a), ICON$_{nogwd-}$ (b), ICON$_{sso-}$ (c) and ICON$_{gwd-}$ (d) bias to ERA-Interim. Dashed/solid lines indicate statistical significance at the 95/99% level according to a two-sided Wilcoxon-test.

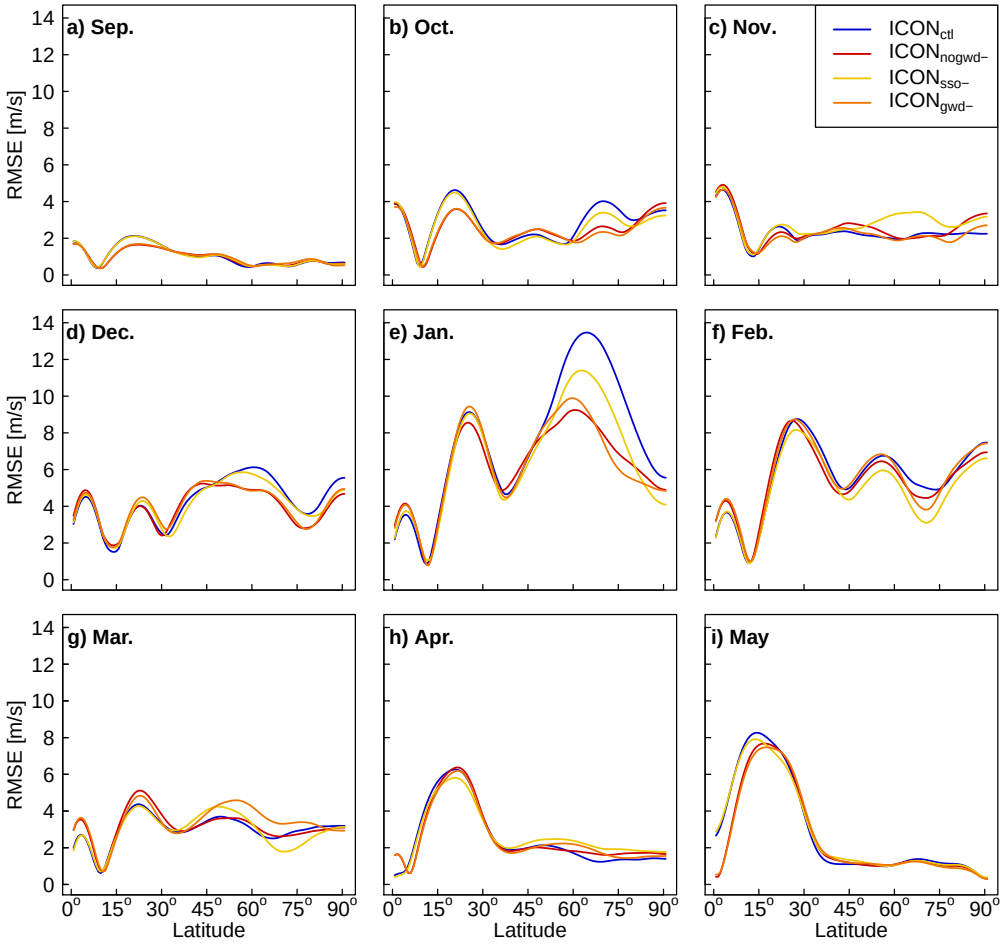

Fig. 4.13.: Zonal mean RMSE of zonal wind in 10 hPa for the months September until May (Latitude-RMSE cross section). The different experiments are denoted by the colours blue (ICON$_{ctl}$), red (ICON$_{nogwd-}$), yellow (ICON$_{sso-}$) and orange (ICON$_{gwd-}$).

between the different model experiments. This is an indication that the gravity wave drag plays a minor role for the stratospheric circulation in autumn. In winter, however, the gravity wave drag becomes more important. Already in December, the gravity wave reduction causes an error reduction in the high latitudes. This accounts in particular for experiments with reduced non-orographic drag (ICON$_{nogwd-}$ and ICON$_{gwd-}$). Once again, January stands out: It is the month with the largest errors in ICON$_{ctl}$, but also the month with the largest error reductions in the sensitivity experiments. The strong RMSE reduction in the sensitivity experiments is caused by a strengthening of the stratospheric polar vortex as a result of reduced gravity wave drag. Thereby the positive effect of the non-orographic gravity wave drag is larger than by the orographic drag. As the stratospheric vortex weakens in spring, also the effect of the gravity wave drag on the stratospheric circulation is reduced. Hence, there are only small differences between the ICON simulations. Whereas RMSEs in the high

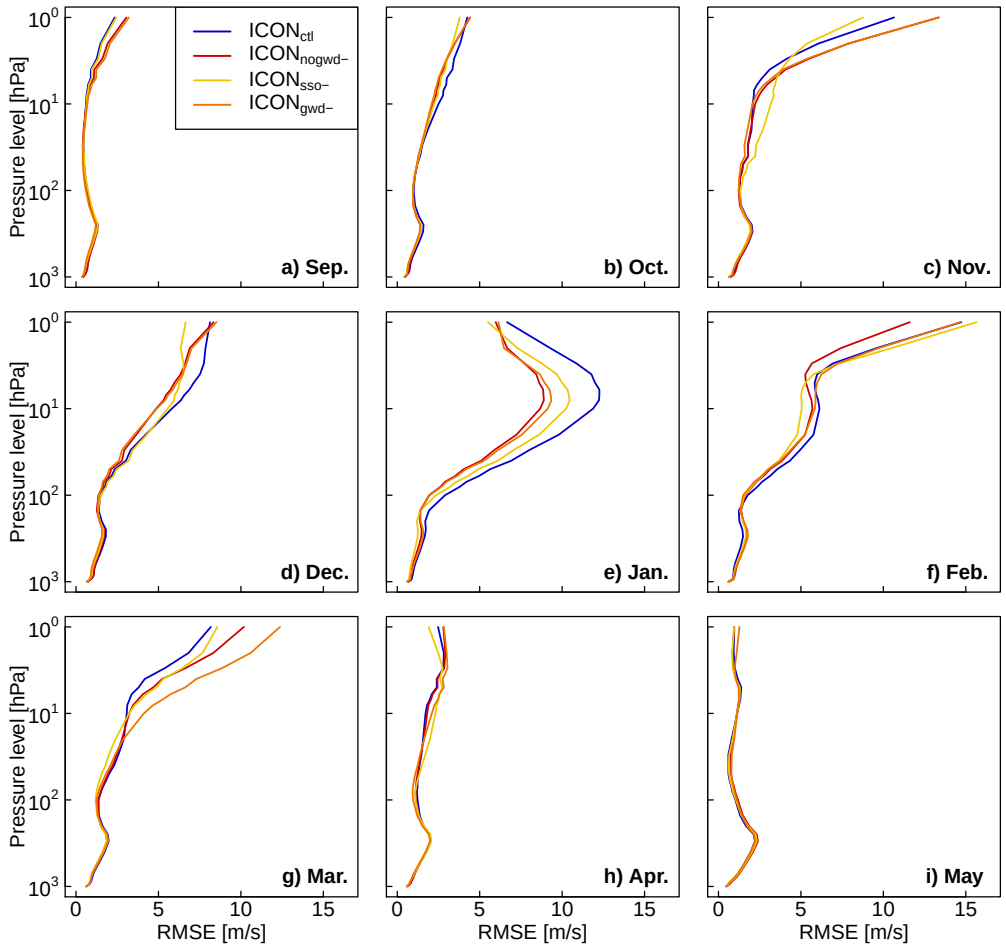

Fig. 4.14.: Field mean (50°-70° N) RMSE of zonal wind for the months September until May (RMSE-height cross section). The different experiments are denoted by the colours blue (ICON$_{ctl}$), red (ICON$_{nogwd-}$), yellow (ICON$_{sso-}$) and orange (ICON$_{gwd-}$). The height is given in pressure coordinates from 1000 hPa to 1 hPa.

latitudes are small, the errors in the lower latitudes increase towards the end of spring. These errors are slightly improved in May due to a reduced non-orographic gravity wave drag.

Whereas Figure 4.13 exhibits the latitudinal distribution of errors, it does not include any information about the vertical distribution of the errors. Therefore, the field mean RMSE in a RMSE-height cross section is visualised in Figure 4.14. The field mean is calculated over the region between 50°-70° N, as it includes the stratospheric polar vortex. The main findings do not change, when this region is shifted (i.e. 40°-60° N and 60°-80° N). In autumn errors are small in all levels, with increasing errors in upper stratosphere in November. Largest errors, but also differences between the ICON experiments, are visible from December to March, with a maximum RMSE reduction in January. This error reduction is clearly present

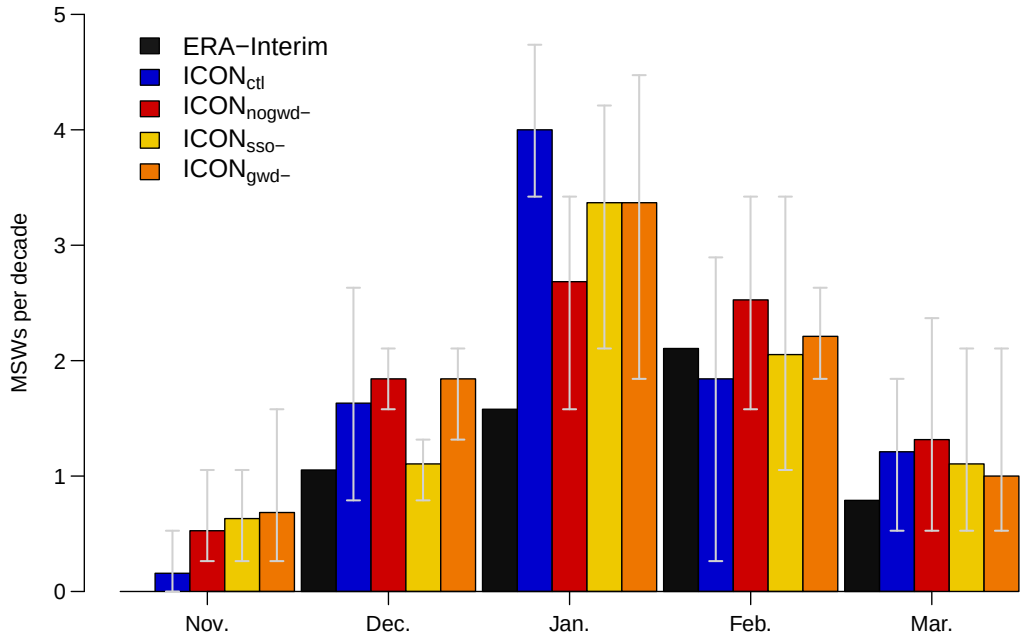

Fig. 4.15.: MSWs per decade and month (November - March) for ERA-Interim (black), ICON$_{ctl}$ (blue), ICON$_{nogwd-}$ (red), ICON$_{sso-}$ (yellow) and ICON$_{gwd-}$ (orange). The spread of the ICON ensemble members is given by the light grey error bar. MSWs are identified by a reversal of the zonal mean zonal wind in 10 hPa and 60°N and a simultaneous reversal of the temperature gradient between 60°N and 90°N (cf. Section 3.3.2).

in all vertical levels of the stratosphere and also in the upper troposphere (cf. Fig. 4.14 e). It seems to originate in the upper stratosphere in December and propagates downward in the course of winter, thereby peaking in the mid stratosphere in January. The upper stratospheric increase of the RMSE in the sensitivity experiments in March does not affect the layers below, due to the fact that the polar vortex is in the declining phase transitioning to the stable summer regime. In April and May RMSEs are small in all levels.

This section has shown, that a reduction of the gravity wave drag leads to an intensified stratospheric polar vortex and an error reduction, in particular in January. Figure 4.9 showed, that in addition the MSW frequency is largely overestimated in January. How this behaviour is influenced by the new parameters, is illustrated analogously in Figure 4.15 for ERA-Interim and the four ICON experiments, including the ensemble spread for the ICON experiments. The according MSW statistics is furthermore given in Table A.1 in the appendix. In contrast to the results from Polichtchouk et al. (2018b), the total amount of MSWs in ICON-NWP does not seem to be affected by changes in the gravity wave drag parameterisations (cf. Table A.1). Having said this, the modification of the non-orographic gravity wave drag used by Polichtchouk et al. (2018b) is a lot larger than in this study. Nevertheless, the non-orographic gravity wave drag in particular, seems to have an impact on the distribution of MSWs. Whereas most MSWs occur in February, followed by January,

December and March in ERA-Interim, ICON$_{ctl}$ and ICON$_{sso-}$ exhibit a strong peak in January. In particular in ICON$_{nogwd-}$ the distribution is more realistic, as less MSWs occur in January. However, keeping in mind, that the statistic of ERA-Interim is based solely on 21 MSWs and therefore needs to be treated with caution. Thus, it makes sense to compare the reanalysis to the ICON ensemble spread. Most ensemble members overestimate the MSW frequency from November to January, whereas the ERA-Interim frequency is met by most ensemble members in February and March. In January the ensemble spread shifts towards the more realistic lower frequencies for all sensitivity experiments.

This section demonstrated, that an adjusted gravity wave drag parameterisation can improve the stratospheric circulation in winter. In doing so, the non-orographic drag has a stronger effect on the stratospheric polar vortex. A reduction in the drag is connected to a reduced depositing of stored momentum and energy to the winterly stratosphere, which leads to an intensification of the winterly westerlies, thereby facilitating a bias and error reduction compared to ERA-Interim. These improvements are particularly strong and significant in January. However, the strength of the stratospheric polar vortex is still underestimated. A further mechanism that could be responsible for this vortex weakness, will be discussed in Section 4.3. Prior to that, in the following sections,it will be discussed how the troposphere is influenced by the adjusted parameters directly and indirectly via stratosphere-troposphere coupling.

4.2.2 Effects on stratosphere-troposphere coupling

Based on Baldwin and Dunkerton (2001), the downward coupling of the stratosphere to the troposphere is investigated by analysing the Northern Annular Mode (NAM), which is also known as the Arctic Oscillation in the troposphere. To achieve this, a NAM index, based on the empirical orthogonal function (EOF) of daily zonal mean geopotential at each pressure level, is calculated. The NAM is represented by the first principle component of this EOF. The physical background information for this method is given in Section 3.3.1. It was suggested by Baldwin and Thompson (2009), as it shows the daily evolution of stratosphere-troposphere coupling most clearly and is robust. In contrast to Baldwin and Dunkerton (2001), weak stratospheric vortex events are not defined by the crossing of a threshold in the 10-hPa annular mode, but by the onset of winterly MSWs, a method also used by Polichtchouk et al. (2018a). MSWs are the strongest manifestation of stratosphere-troposphere coupling and represent a weak stratospheric vortex state. As they are furthermore defined at the same altitude as the threshold criteria, both approaches deliver comparable results. This was tested for the reanalysis as well as the ICON simulations.

A composite of the NAM index for MSW events is shown in Figure 4.16 for ERA-Interim (a) and the different ICON experiments (b-e). MSWs lead to a strong weakening of the NAM in the stratosphere. After the onset in the upper stratosphere, the signal propagates downward and remains present in the lower stratosphere with a lag of up to 60 days. Some of the weak NAM signals also propagate to the troposphere leading to a weakening of the Arctic Oscillation. On average MSWs are preceded and followed by a significantly strengthened

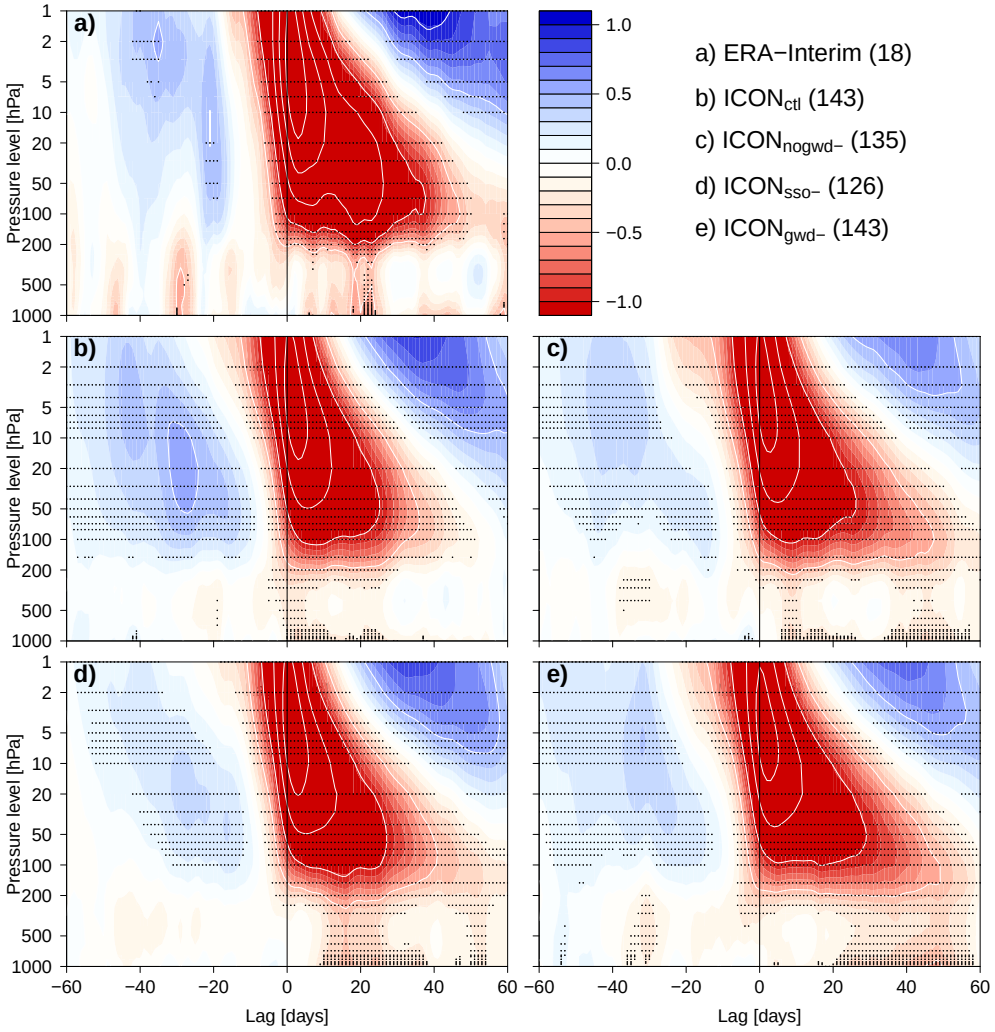

Fig. 4.16.: Composites of time-height development of the NAM for MSWs in winter. The composites are shown for ERA-Interim (a), ICON$_{ctl}$ (b), ICON$_{nogwd-}$ (c), ICON$_{sso-}$ (d) and ICON$_{gwd-}$ (e) respectively. The vertical line marks the day of onset of the MSWs in 10 hPa and the numbers in brackets indicate the total amount of MSWs. The NAM index is non-dimensional. The contour interval for the white contours is 0.5 and stippling indicates difference from 0 at the 95% significance level. Please note that due to common practice negative values (weak NAM) are red and positive values (strong NAM) are blue.

NAM signal in the stratosphere. The described characteristic pattern, including the abrupt onset of the MSW, is reproduced in all ICON experiments. Yet, there are some distinct differences between the gravity wave drag experiments. The downward propagation of weak NAM signals in ICON$_{ctl}$ is rather fast with a stratospheric lag of only up to 50 days. In addition, the troposphere is significantly affected only in the first 30 days after the onset of the MSW. A decrease of gravity wave drag leads to a more persistent MSW signal in the lower stratosphere in all three sensitivity experiments. Furthermore, the influence on the troposphere is also increased, demonstrated by significant weak tropospheric NAM signals with a lag of up to 60 days. Although the reduction in the non-orographic gravity wave drag is not as strong as in Polichtchouk et al. (2018a), their finding of an intensified coupling between stratosphere and troposphere, due to reduced drag is reproduced with ICON. In addition, Figure 4.16 d exemplifies that the same accounts for a reduction of orographic gravity wave drag and thus all sensitivity experiments show that a reduction of gravity wave drag lead to a more persistent and realistic signal in the lower stratosphere and the troposphere.

The coupling is strengthened not only for weak vortex events (MSWs), but also for strong stratospheric vortex events (cf. Fig. 4.17). As there is no fixed definition for strong vortex events (such as MSWs), the NAM index in 10 hPa is used to identify strong vortex events. In accordance with Baldwin and Dunkerton (2001), strong vortex events are defined by the crossing of a threshold of 1.5 in the NAM index. In total there are 23 events with large positive NAM anomalies that exceed this threshold in ERA-Interim, a number which is comparable to the 18 weak vortex events (MSWs). Furthermore, the reanalysis and the four ICON experiments have a similar frequency of events, with 6.1 events per decade in ERA-Interim, 6.2 in ICON$_{ctl}$, 5.5 in ICON$_{nogwd-}$, 5.8 in ICON$_{sso-}$ and 6.3 in ICON$_{gwd-}$. The ERA-Interim strong vortex anomaly pattern is not as well spatially confined as the weak vortex anomaly pattern during MSWs, in particular prior to the onset. Significant strong NAM anomalies in the whole atmospheric column precede the strong NAM anomalies in 10 hPa by up to 30 days. The NAM anomalies are less long-lived in the lower stratosphere with significant anomalies up to 30 days after the onset of the event. Moreover, the coupling to the stratosphere is not as strong, as significant tropospheric anomalies are only visible the first 25 days after the onset of the event. The less long-lasting nature of the strong NAM anomalies can be explained by the fact that these events are an intensification of the climatological mean state (westerly wind regime), whereas MSWs are accompanied by a complete disruption of the climatological state. The different ICON experiments are able to reproduce the basic structure of this pattern. However, the significant regions are more clearly spatially confined, an effect that could be explained by the fact that the composite is based on a larger amount of events due to the ensemble approach. Nonetheless, this effect is not observed for weak NAM events (cf. Fig. 4.16). In ICON, the weak NAM anomalies in the stratosphere 30-60 days prior the strong NAM event and in the upper stratosphere 30-60 after the onset are significant. As for weak vortex events, the coupling between stratosphere and troposphere is also intensified for strong vortex events due to reduced gravity wave drag. This in particular accounts for the experiments with reduced non-orographic gravity wave drag (cf. Figures 4.17 c and e). As a matter of fact, the coupling for these events seems

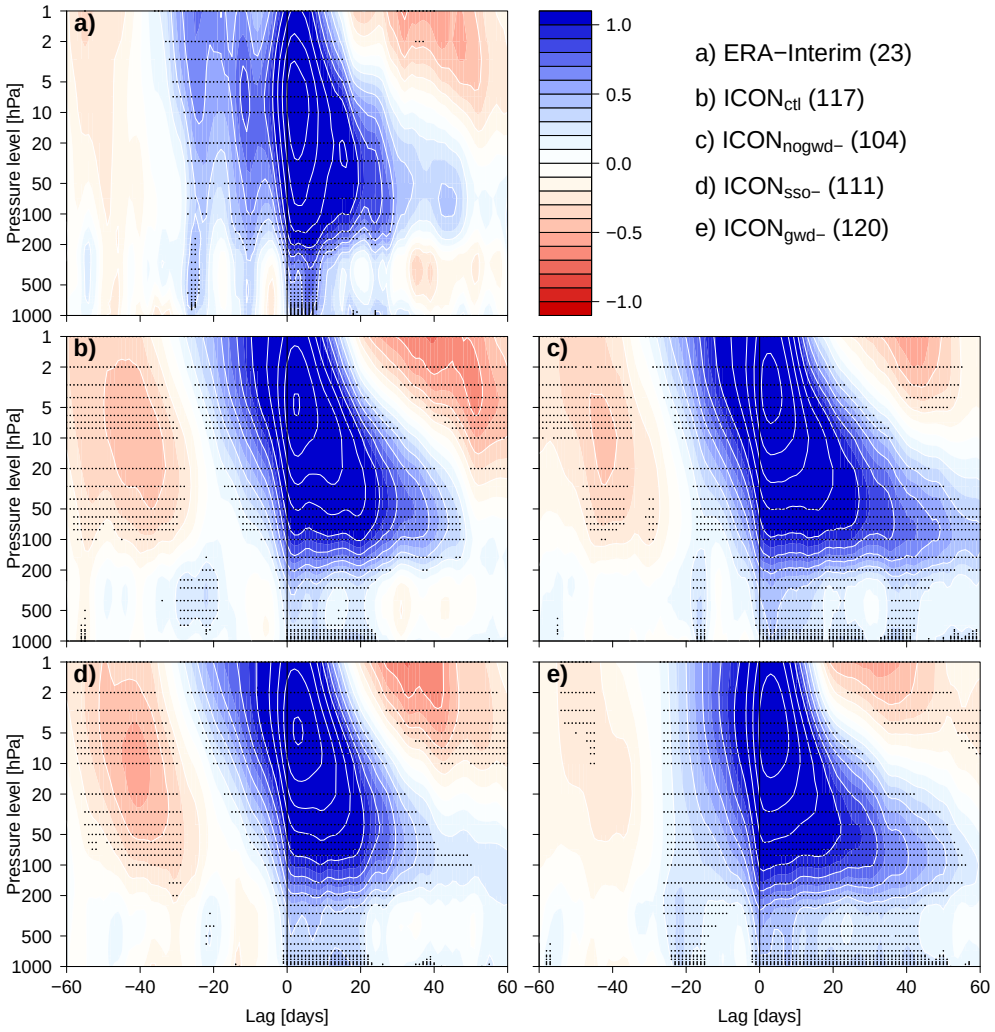

Fig. 4.17.: Composites of time-height development of the NAM for strongly positive stratospheric NAM events, where the NAM index in 10 hPa is larger than 1.5. The composites are shown for ERA-Interim (a), ICON$_{ctl}$ (b), ICON$_{nogwd-}$ (c), ICON$_{sso-}$ (d) and ICON$_{gwd-}$ (e) respectively. The vertical line marks the day of onset of the event and the numbers in brackets indicate the total amount of events. The NAM index is non-dimensional. The contour interval for the white contours is 0.5 and stippling indicates difference from 0 at the 95% significance level. Please note that due to common practice negative values (weak NAM) are red and positive values (strong NAM) are blue.

to be overestimated in ICON$_{nogwd-}$ and ICON$_{gwd-}$ with significant NAM anomalies in the troposphere up to 60 days after the onset of the event. As ICON favours a weak NAM in the troposphere (cf. Section 4.1.1), this overestimated downward coupling of strong NAM events could have a positive effect on the tropospheric pressure patterns. Furthermore, all ICON experiments exhibit a significant strong NAM signal in the troposphere 15-30 days prior to the onset of the event, a signal also visible in the reanalysis.

The presented ICON composites for weak and strong vortex events closely resemble the results from Baldwin and Dunkerton (2001), which is based on National Centers for Environmental Prediction (NCEP) reanalysis data during 1958–1999. Moreover, the NCEP composite for the strong vortex events more closely resembles the well confined ICON pattern than the ERA-Interim pattern.

Figures 4.16 and 4.17 depict the NH reaction to particularly strong and weak stratospheric vortex events. However, a different approach is also of interest: instead of creating a composite of extreme stratospheric events, extreme near surface events in the troposphere are used for figures 4.18 and 4.19. This method allows for the recognition of large-scale patterns that precede or follow strongly negative or positive surface NAM patterns in 1000 hPa. Extreme events are defined by a crossing of the threshold of -2 (weak NAM) and 2 (strong NAM), so that there are 19 events in each case for ERA-Interim.

Figure 4.18 depicts the composites of time-height development of the NAM for strongly negative NAM events in 1000 hPa. A weak surface NAM is connected to high pressure anomalies in high latitudes and low pressure anomalies in lower latitudes and is hence characterised by weakened pressure gradient (cf. Section 4.1.1). The resulting weakened and meandering jet stream is often connected to extreme weather in mid-latitudes. Therefore, the understanding of potential precursor mechanisms are of large interest to the sub-seasonal to seasonal prediction community. Whereas significant NAM anomalies in the troposphere only appear four days prior to the weak NAM event, a weak NAM in the stratosphere precedes these events by up to 17 days (cf. Fig. 4.18 a). The event itself mainly remains in the troposphere, with significant anomalies up to 30 days after the onset of the event. It is furthermore connected to a strengthening of the NAM in the upper stratosphere 10-25 days after the onset of the weak NAM event. Once more, all ICON experiments reproduce these basic features and have a slightly overestimated frequency of weak NAM events, with 5 events per decade in ERA-Interim, 5.6 in ICON$_{ctl}$, 5.9 in ICON$_{nogwd-}$, 5.8 in ICON$_{sso-}$ and 5.6 in ICON$_{gwd-}$. The stratospheric precursor is visible in all four ICON experiments, but is again intensified in the experiments with reduced gravity wave drag. The reduced gravity wave drag furthermore leads to a more long lasting significant weak NAM signal in the troposphere (30-40 days) and an overall more realistic pattern.

Analogously, Figure 4.19 depicts the composites of time-height development of the NAM for strong NAM events. A strong NAM is connected to a more zonal and intensified jet stream, enabling less meridional transport in the mid-latitudes. First significant strong NAM anomalies are visible in the stratosphere up to 50 days prior to the onset of the strong NAM event. This demonstrates, that the stratosphere could play a large role in the prediction of these extreme events on seasonal time scales. The significant strong NAM

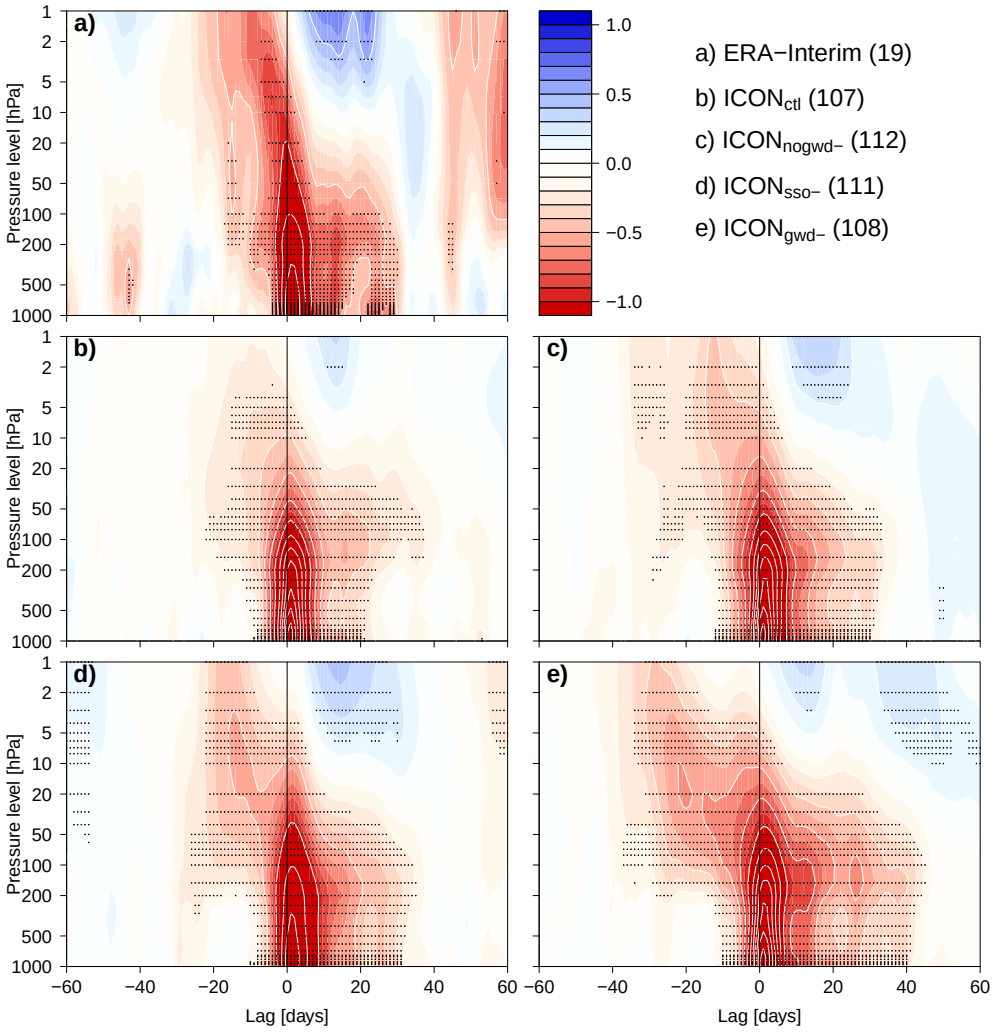

Fig. 4.18.: Composites of time-height development of the NAM for strongly negative tropospheric NAM events, where the NAM index in 1000 hPa is larger than 2. The composites are shown for ERA-Interim (a), ICON$_{ctl}$ (b), ICON$_{nogwd-}$ (c), ICON$_{sso-}$ (d) and ICON$_{gwd-}$ (e) respectively. The vertical line marks the day of onset of the event and the numbers in brackets indicate the total amount of events. The NAM index is non-dimensional. The contour interval for the white contours is 0.5 and stippling indicates difference from 0 at the 95% significance level. Please note that due to common practice negative values (weak NAM) are red and positive values (strong NAM) are blue.

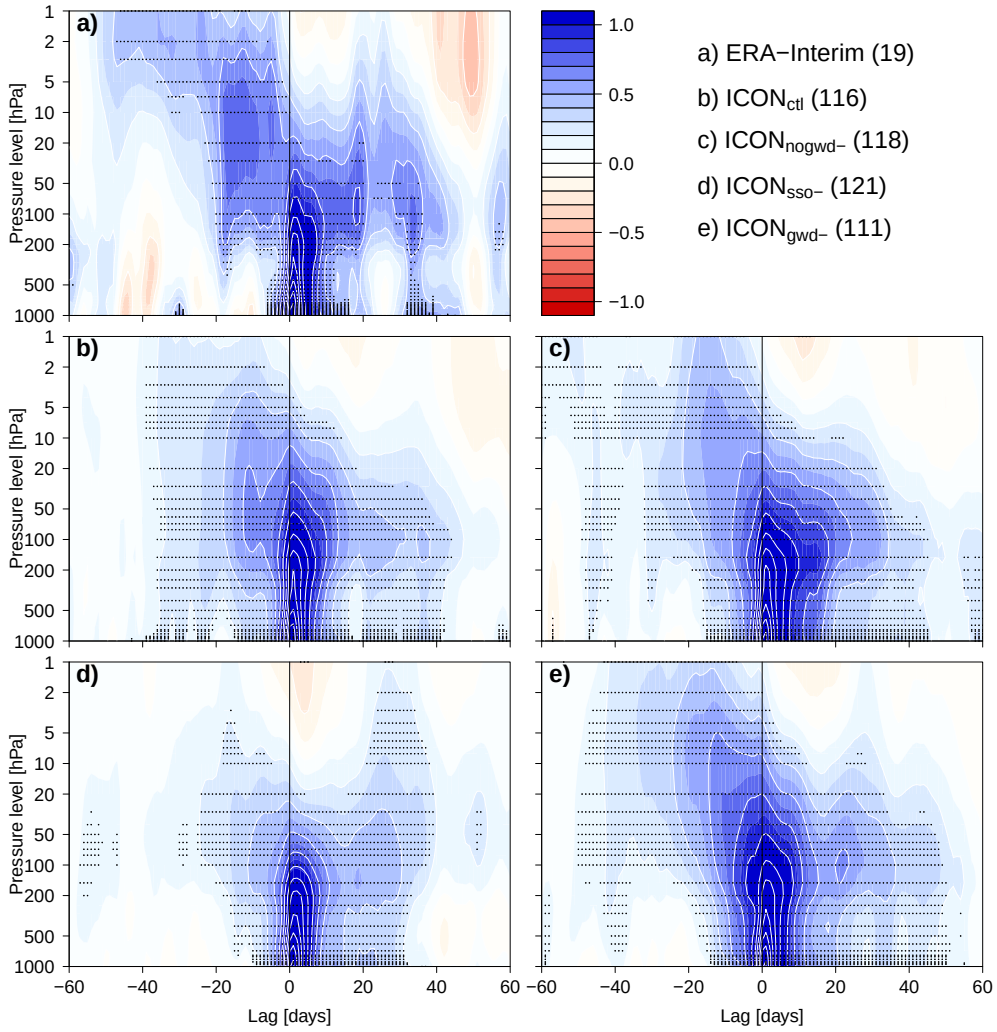

Fig. 4.19.: Composites of time-height development of the NAM for strongly positive tropospheric NAM events, where the NAM index in 1000 hPa is larger than 2. The composites are shown for ERA-Interim (a), ICON$_{ctl}$ (b), ICON$_{nogwd-}$ (c), ICON$_{sso-}$ (d) and ICON$_{gwd-}$ (e) respectively. The vertical line marks the day of onset of the event and the numbers in brackets indicate the total amount of events. The NAM index is non-dimensional. The contour interval for the white contours is 0.5 and stippling indicates difference from 0 at the 95% significance level. Please note that due to common practice negative values (weak NAM) are red and positive values (strong NAM) are blue.

anomalies are present in the troposphere and lower stratosphere for up to 40 days after the onset of the event. All ICON experiments overestimate the frequency of strong NAM events, with 6.1 events per decade in ICON$_{ctl}$, 6.2 in ICON$_{nogwd-}$, 6.4 in ICON$_{sso-}$ and 5.8 in ICON$_{gwd-}$, compared to 5 events per decade in ERA-Interim. Nonetheless, the basic pattern is simulated well by the ICON experiments. A weak intensification of stratosphere-troposphere coupling is only visible in the experiments with reduced non-orographic gravity wave drag (ICON$_{nogwd-}$ and ICON$_{gwd-}$). They exhibit the most realistic behaviour with weak tropospheric precursors and a strong stratospheric precursor. ICON$_{sso-}$ exhibits less precursor behaviour but a stronger upward branch up to 40 days after the event, a feature that also exists in ICON$_{gwd-}$ and ERA-Interim, but is not statistically significant.

This section has shown that a reduction in the gravity wave drag leads to an intensification of stratosphere-troposphere coupling. This especially accounts for a reduction in the non-orographic drag. These results are in accordance with Polichtchouk et al. (2018a). The time-height development of the NAM is suitable to investigate propagation of extreme events, but drawing conclusions on the mean state is less unambiguous. To understand how the mean tropospheric state is influenced by the gravity wave drag parameterisations, MSLP biases and RMSEs of the different drag experiments are investigated in the following section.

4.2.3 Tropospheric effects

The troposphere in ICON$_{ctl}$ suffers from underestimation of the meridional pressure gradient, due to high pressure bias in the Arctic and low pressure bias in lower latitudes (cf. Section 4.1.1). A feature that becomes especially apparent in winter. The opposite bias pattern (highs too high, lows too low) was apparent in the predecessor model COSMO. This led to the hypothesis that in the model there is too little surface drag, causing an underestimation of the cross-isobar flow in the planetary boundary layer (cf. ICON Tutorial, Section 3.1.1). The sub-grid scale orographic drag scheme was implemented to overcome this bias. However, the parameters were not explicitly tested for the different ICON resolutions. The results from Section 4.1.1 suggest an overestimated surface drag. Consequently, the strength of the SSO scheme was reduced in the experiments ICON$_{sso-}$ and ICON$_{gwd-}$ (cf. Table 3.2).

Whereas the effect of the non-orographic drag is stronger in the stratosphere (cf. Section 4.2.1), the effect of the adjusted SSO scheme dominates in the troposphere. The two experiments with the adjusted SSO scheme show strongly reduced MSLP RMSEs in all months (cf. Fig. 4.20 and Table A.1). This effect can be attributed to more suitable values for the low level wake drag constant and the critical Froude number. Furthermore, the improved stratospheric winter circulation seems to impact the surface pressure patterns by stratosphere-troposphere coupling. Indicators for this are the error reduction in ICON$_{nogwd-}$ compared to ICON$_{ctl}$ in addition to the improvements of ICON$_{gwd-}$ compared to ICON$_{sso-}$. The polar cap mean RMSE average over the whole period (September - May) is reduced by 2% in ICON$_{nogwd-}$, 29% in ICON$_{sso-}$ and 30% ICON$_{gwd-}$ (cf. Table A.1).

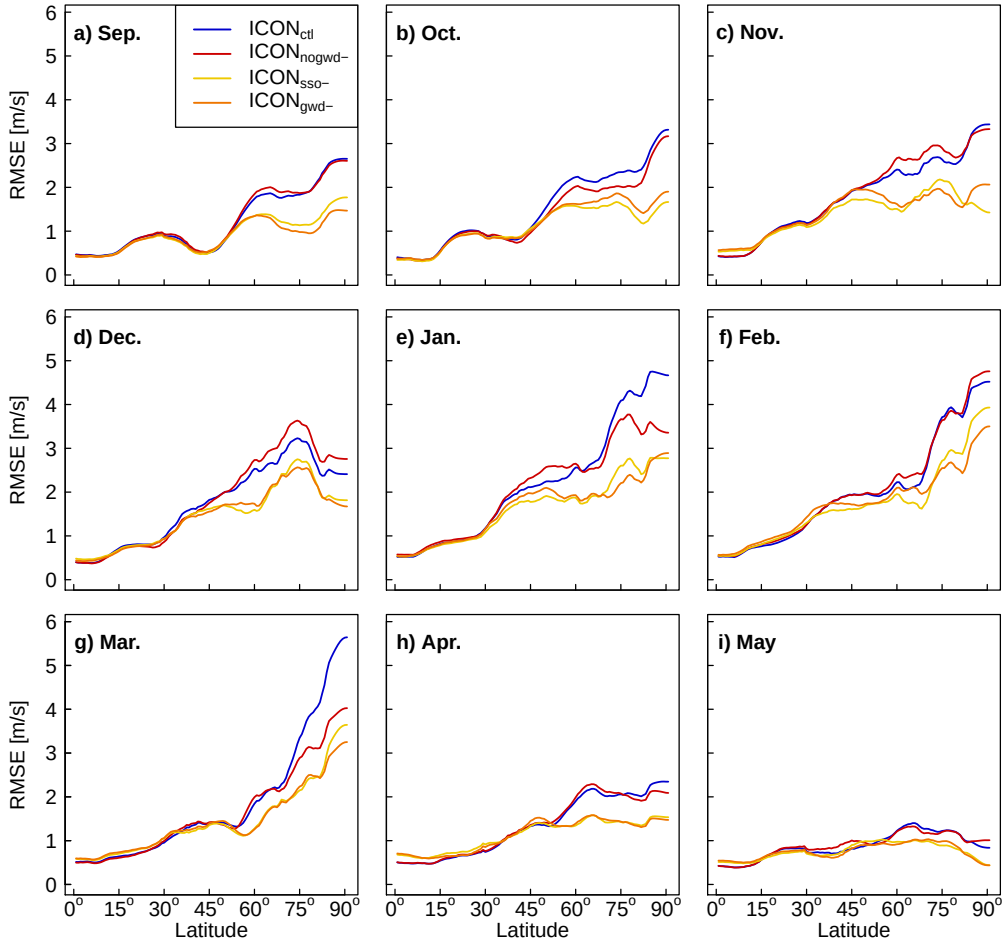

Fig. 4.20.: Zonal mean RMSE of MSLP for the months September until May (Latitude-RMSE cross section). The different experiments are denoted by the colours blue (ICON$_{ctl}$), red (ICON$_{nogwd-}$), yellow (ICON$_{sso-}$) and orange (ICON$_{gwd-}$).

The tropospheric RMSE improvements of the sensitivity experiments are most evident in January and March. The following analysis will focus on the improvements in January, as this is when the positive effect of the improved stratospheric circulation on the MSLP patterns becomes particularly apparent. The downward propagation of stratospheric signals leads to a reduction of the polar cap mean RMSE of the MSLP by 13% in ICON$_{nogwd-}$ (cf. Fig. 4.20 e and Table A.1). Adjusting the SSO scheme produces an error reduction of 37% and the combined effect causes an improvement of 42% in January.

The effect of the different gravity wave drag reductions in January is depicted in Figure 4.21 as a polar stereographic projection. The MSLP differences of the other months are given in Figure A.2 (ICON$_{nogwd-}$), A.3 (ICON$_{sso-}$) and A.4 (ICON$_{gwd-}$) in the appendix. All three sensitivity experiments exhibit significantly reduced MSLP in the Arctic and increased MSLP over the Pacific and Atlantic. This effect is connected to the RMSE reduction from Figure

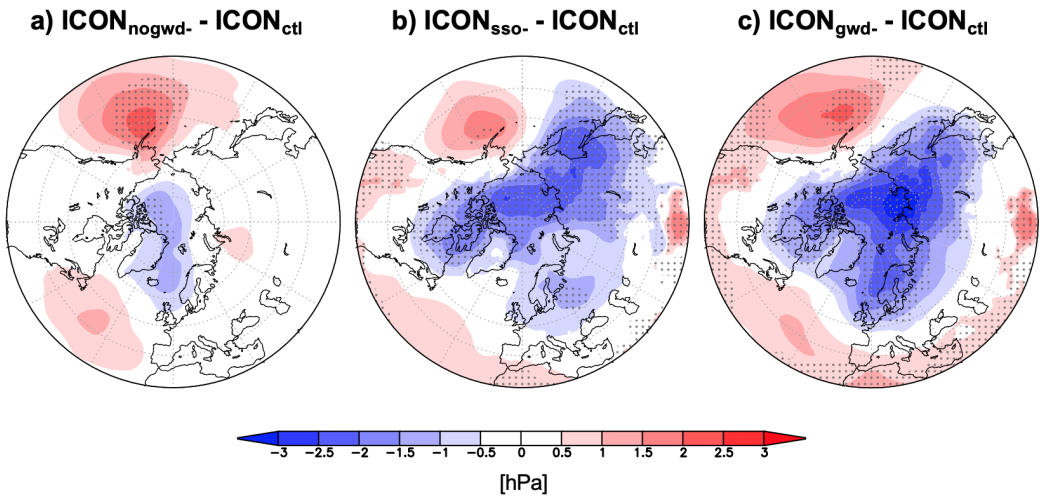

Fig. 4.21.: January mean MSLP difference to ICON$_{ctl}$ for ICON$_{nogwd-}$ (a), ICON$_{sso-}$ (b) and ICON$_{gwd-}$ (c). Stippling indicates statistical significance at the 95% level according to a two-sided Wilcoxon-test.

4.20 e. It is strongest in ICON$_{gwd-}$, followed by ICON$_{sso-}$ and ICON$_{nogwd-}$. Once again, the combined effect seems to be quasi-additive. The described pattern due to the adjusted SSO scheme is also observed in the other months.

Figure 4.22 displays the MSLP bias of the four ICON experiments to ERA-Interim in January. The bias patterns remain constant in all four experiments, but the bias magnitude and significance is reduced in the sensitivity experiments. Largest effects are visible in the central Arctic region in the experiments with adjusted SSO scheme. Due to reduced MSLP, the Arctic bias is small and less significant. Smaller bias reductions are also visible in the mid-latitudes. The direct SSO effect is clearly stronger than the non-orographic gravity wave drag effect via the stratosphere. However, there are significant MSLP biases that remain in all experiments, in particular over North America and Japan. The biases in the other months are weaker (cf. Table A.1), but exhibit a similar structure with high pressure bias in the Arctic and low pressure bias over the Atlantic and Pacific.

All three sensitivity experiments show reduced MSLP biases in the NH. Thereby, ICON$_{gwd-}$ exhibits the largest improvements due to the combined effect of both parameterisations. Taking into account the bias reductions in the stratosphere and troposphere, ICON$_{gwd-}$ is the current optimal setup for seasonal experiments with ICON-NWP.

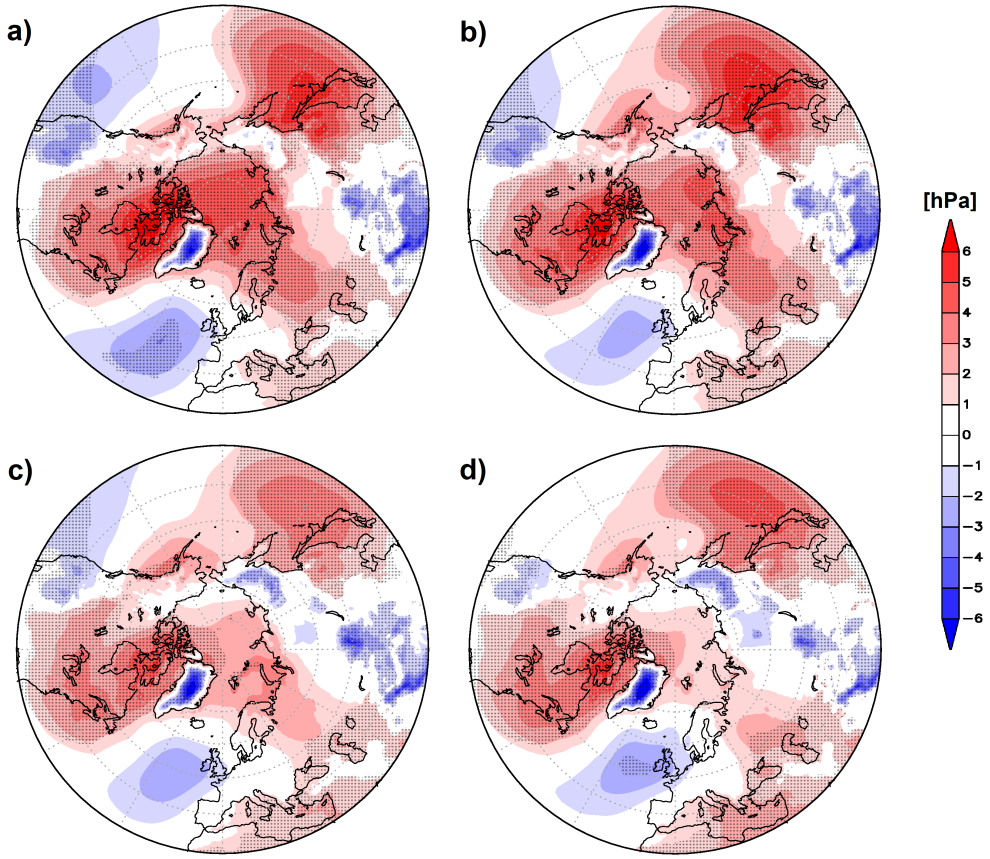

Fig. 4.22.: January mean MSLP bias to ERA-Interim for ICON$_{ctl}$ (a), ICON$_{nogwd-}$ (b), ICON$_{sso-}$ (c) and ICON$_{gwd-}$ (d). Stippling indicates statistical significance at the 95% level according to a two-sided Wilcoxon-test.

4.3 Low latitudinal influence on the stratospheric polar vortex

Section 4.1 demonstrated that the strength of stratospheric polar vortex in winter is underestimated by ICON-NWP. The seasonal control climatology ICON$_{ctl}$ furthermore exhibits a high MSW frequency and a reduced meridional pressure gradient in the troposphere. The stratospheric biases can be reduced by a reduction of the orographic and in particular the non-orographic gravity wave drag (cf. Section 4.2). Furthermore, MSLP biases are strongly reduced by adjusting the SSO scheme. The climatology with the combined new parameterisations, including an overall reduced gravity wave drag and an adjusted SSO surface scheme, is characterised by the largest overall bias reductions (ICON$_{gwd-}$). Therefore in the following, the results for the control experiment ICON$_{ctl}$ and the current optimal setup ICON$_{gwd-}$ are shown and compared to the reanalysis ERA-Interim.

Although stratospheric biases are significantly reduced in ICON$_{gwd-}$, stratospheric westerlies are still simulated significantly too weak in winter (cf. Section 4.2.1). Therefore, in this section, further mechanisms, that influence the stratospheric polar vortex and could contribute to its weakness, are investigated. Figure 4.23 depicts the climatologies and biases of the zonal mean zonal wind as mean over the whole simulation period (September - May) for ERA-Interim and the two simulations ICON$_{ctl}$ and ICON$_{gwd-}$. The strong westerlies in the climatologies reveal the positions of the tropospheric jet and the stratospheric vortex. The underestimated stratospheric westerlies in the high latitudes are clearly visible and highly significant. However, the bias patterns in the lower latitudes have a stronger amplitude, as they are more consistent throughout time. While the bias of the polar vortex is exists in winter only, the bias patterns in the lower latitudes are persistent over the whole simulation period. Figure 4.23 e) exemplifies the effect of a reduced gravity drag (cf. Section 4.2). Due to a strengthening of the polar vortex, high latitudinal biases in the mid an lower stratosphere and the troposphere are significantly reduced. The lower latitudes, however, are not significantly effected by the adjusted parameterisations. This suggests, that there is a further issue in ICON, which is independent of the gravity wave drag parameterisations and related to the stratosphere of the low latitudes.

The tropical stratosphere is directly connected to the QBO (cf. Section 2.2.4), a quasi-periodic oscillation in the mean zonal winds of the equatorial stratosphere, which is known to also have an influence on the stratospheric polar vortex (Holton and Tan, 1980). On average, the stratospheric polar vortex is weaker in the easterly QBO phase. In addition, ENSO (cf. Section 2.3.2), an irregularly periodic variation in winds and sea surface temperatures over the tropical Pacific, is also known to influence stratosphere dynamics, i.e. the warm ENSO phase is connected to a weaker stratospheric polar vortex in the Northern Hemisphere (e.g. Camp and Tung, 2007; Garfinkel and Hartmann, 2007; Free and Seidel, 2009; Manzini, 2009). The following two sections will analyse, how these low latitudinal oscillations are simulated in ICON and how they influence the stratospheric polar vortex.

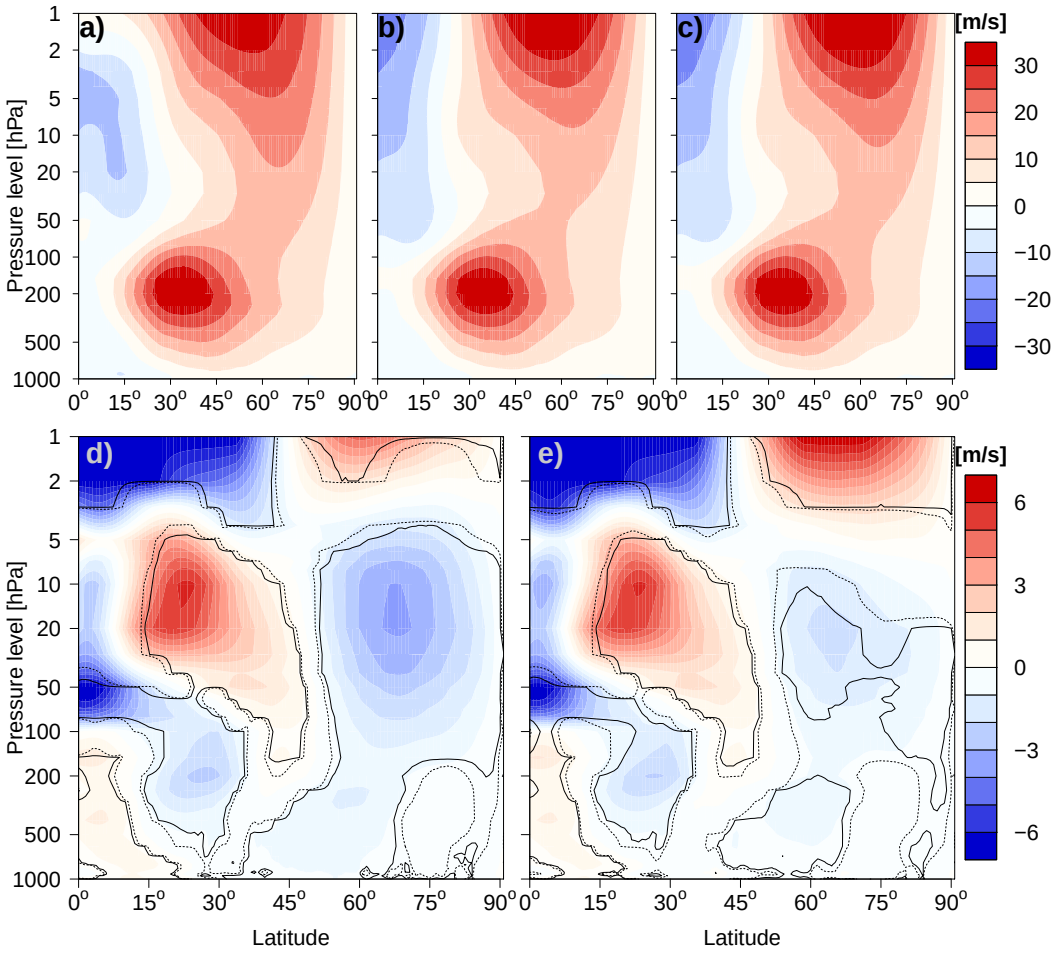

Fig. 4.23.: Time mean (Sep-May) zonal mean zonal wind climatology for ERA-Interim (a), ICON$_{ctl}$ (b) and ICON$_{gwd-}$ (c) as well as the equivalent biases of ICON$_{ctl}$ (d) and ICON$_{gwd-}$ (f) compared to ERA-Interim. Dashed/solid lines in d and f indicate statistical significance at the 95/99% level according to a two-sided Wilcoxon-test.

4.3.1 Quasi-biennial oscillation

The ICON experiments exhibit significant negative zonal wind bias in the equatorial stratosphere (cf. Fig. 4.23). This mean state, however, cannot describe an quasi-oscillatory behaviour as it is known from the QBO (cf. Section 2.2.4). Instead of considering the mean state, the QBO development in each year (September - May) and ensemble member is displayed in Figure 4.24. The zonal mean zonal wind at the Equator and 50 hPa altitude is commonly used to outline the QBO development. The colours of the lines are grouped according to their initial values, so that the initial state is easily retraced.

Common QBO behaviour is visible in ERA-Interim (cf. Fig. 4.24 a). The zonal wind values range between 17 m/s and -28 m/s. A large fraction of years exhibit a phase reversal in

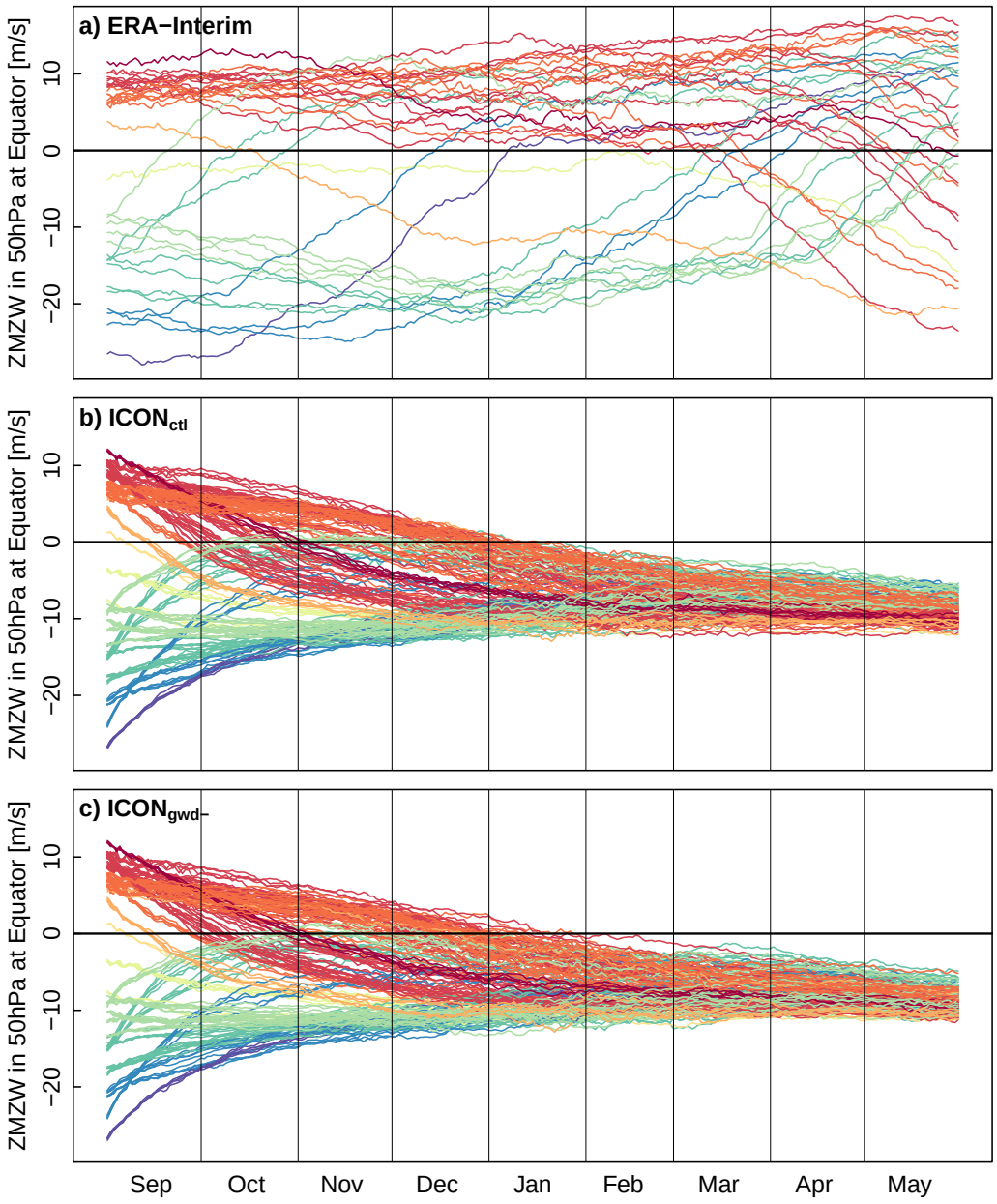

Fig. 4.24.: Zonal mean zonal wind (ZMZW) in 50 hPa at Equator for ERA-Interim (a), ICON$_{ctl}$ (b) and ICON$_{gwd-}$ (c). Each year (and each ensemble member) is represented by one line. The colours of the lines are grouped according to their initial value with red (blue) colors representing westerly (easterly) wind.

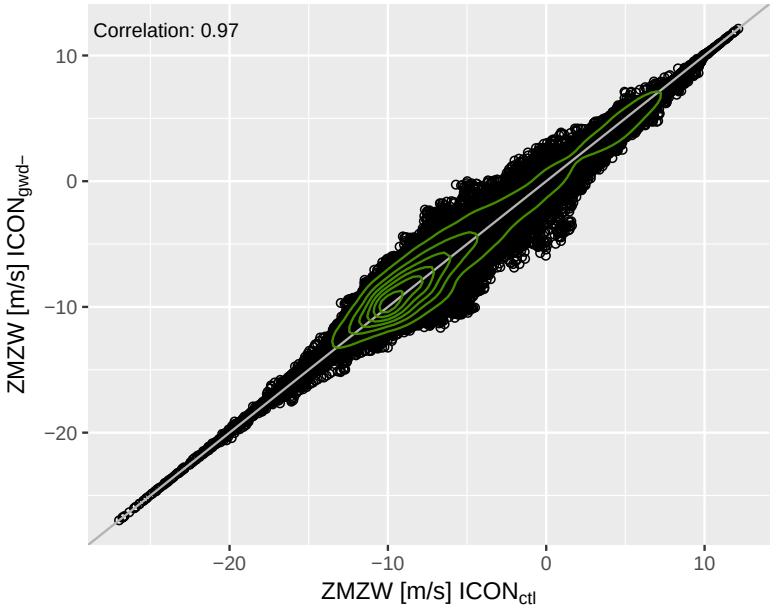

Fig. 4.25.: Scatter plot of zonal mean zonal wind (ZMZW) in 50 hPa at Equator for ICON$_{ctl}$ vs. ICON$_{gwd-}$. The diagonal is given in light grey and the distribution of the data is shown in green contours for a bin width of 0.05.

late spring, a feature common to the QBO (Dunkerton, 1990; Baldwin et al., 2001). As the QBO is not an exactly biennial oscillation, phase reversals in other seasons can also be observed. The easterly phase usually has a higher amplitude, but is shorter lived in 50 hPa. The ICON simulations are initialised with the whole spectrum of QBO phases from the ERA-Interim data. Figures 4.24 b and c clearly illustrate, that ICON does not simulate a QBO. Independent of the initialisation, the zonal mean zonal wind shifts towards weak easterlies. Already by the end of January all runs exhibit easterly winds in the tropical stratosphere. Furthermore, the differences in the gravity wave drag parameterisation do not seem to affect these equatorial zonal winds.

Figure 4.25 further demonstrates that the gravity wave drag parameterisations have no effect on the equatorial zonal wind in the stratosphere. The zonal mean zonal wind values are clearly aligned along the diagonal in the scatter plot. Moreover, the two simulations are highly correlated and the linear regression of the data with a slope of 0.99 and a intercept of -0.12 closely resembles the diagonal. There is a clear single peak in the distribution of the data at -10 m/s, which also proves that ICON does not simulate the QBO and tends to shift towards weak easterly circulation in the equatorial stratosphere.

To investigate how the tendency towards the easterly QBO phase in ICON affects the stratospheric polar vortex, the monthly, zonal mean zonal wind bias patterns are evaluated in a latitude-height cross section for ICON$_{ctl}$ (cf. Fig. 4.26 f-j) and ICON$_{gwd-}$ (cf. Fig. 4.26 k-o). We compare the evolution of these bias patterns with the evolution of the QBO-E composite anomalies from ERA-Interim (cf. Fig. 4.26 a-e). The QBO-E composite is based

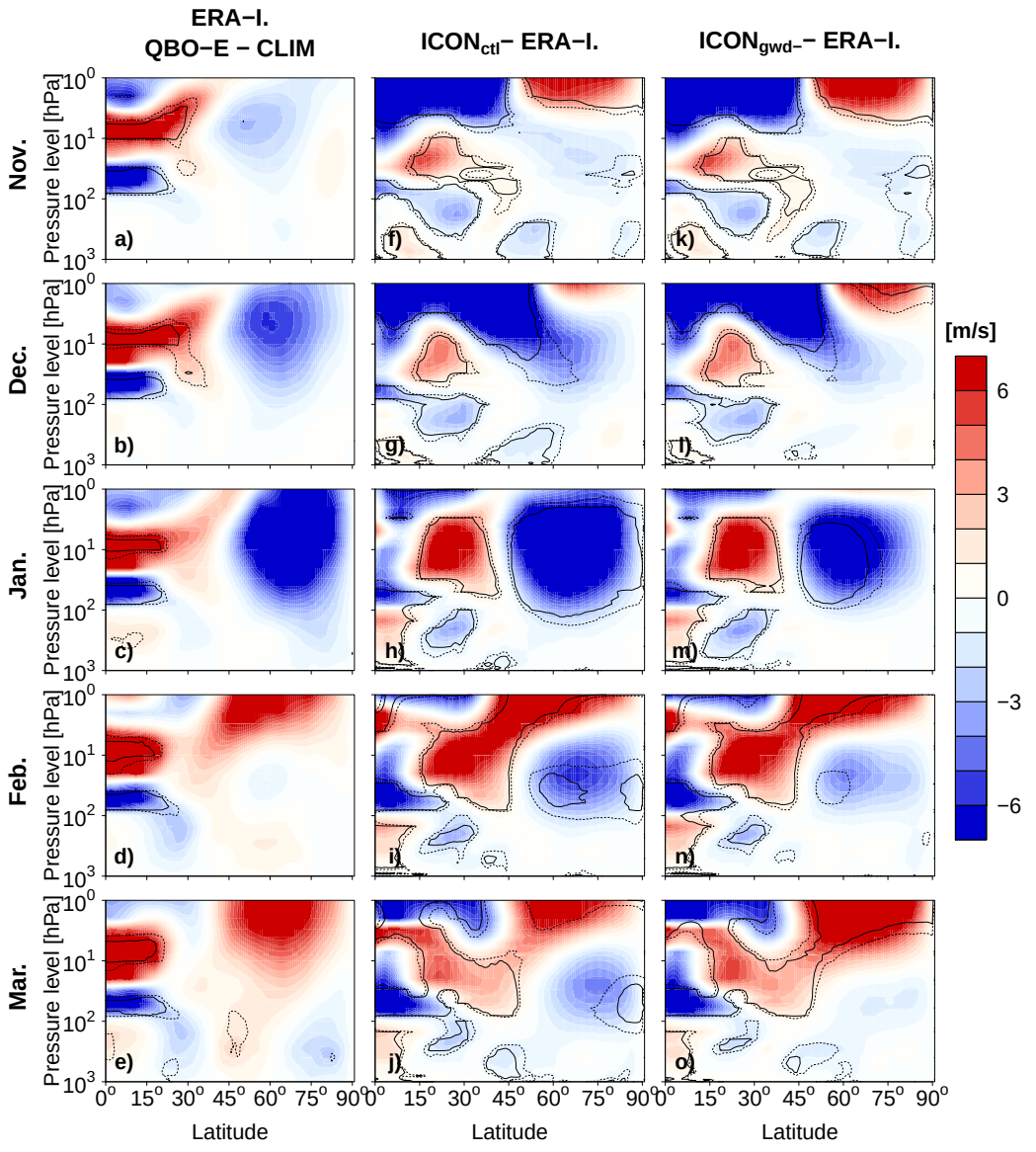

Fig. 4.26.: Monthly, zonal mean zonal wind anomalies of a QBO-E composite compared to the climatology (CLIM) of ERA-Interim (a-e). Bias of monthly, zonal mean zonal wind of ICON$_{ctl}$ (f-j) and ICON$_{gwd-}$ (k-o) compared to ERA-Interim. Monthly means are shown for the months November - March. Dashed/solid lines indicate statistical significance at the 95/99% level according to a two-sided Wilcoxon-test.

on the QBO index, i.e. the equatorial monthly, zonal mean zonal wind in 50 hPa. All months are treated independently and included if the wind is easterly, so that different months can include different years. Which years were included in which monthly composite is outlined in Table A.2 in the appendix. The composite is evaluated against the climatology. The highly significant QBO signal is visible in all months, with negative anomalies at 50 hPa, positive differences at 10 hPa and again negative anomalies at approximately 1 hPa. Due to the high variability of the stratosphere, the extratropical anomalies in ERA-Interim are mostly non-significant. However, there is a clear pattern of large differences: From November to January the stratospheric polar vortex is weakened, followed by a strengthening in the upper stratosphere in February and March. The extratropical negative anomalies move northward and downward in time. The weakening of the stratospheric polar vortex during QBO-E is in accordance with literature (e.g Holton and Tan, 1980). The strongest extratropical QBO-E signal is visible in January.

The biases of the ICON experiments exhibit similar patterns to those visible in QBO-E phase in ERA-interim (cf. Fig. 4.26). In November and December largest negative zonal wind biases are visible in the upper stratosphere of the lower latitudes. In winter, however, these biases move towards the higher latitudes and lead to the significantly underestimated polar vortex in both simulations. The negative polar vortex bias peaks in January, followed by a weakening and downward movement in February and March. This is connected to a vortex strengthening in the upper stratosphere. From January to March the ICON bias patterns strongly resemble the ERA-Interim QBO-E pattern, suggesting that a large part of the remaining bias pattern can be explained by the constant easterly QBO in ICON. The ICON biases and the ERA-Interim QBO-E anomalies in November and December are less similar, as not all ICON runs are shifted towards the QBO-E state yet (cf. Fig. 4.24). Whereas the low latitudinal bias patterns remain unchanged by the gravity wave reduction, the high latitudinal biases are reduced in ICON$_{gwd-}$ (cf. Section 4.2.1). By a reduction of the gravity wave drag, the relationship between easterly QBO phase and a weakened polar vortex, i.e. the Holton-Tan relationship, is weakened. To further reduce biases in the stratospheric polar vortex, an improved circulation in the tropical stratosphere of ICON would be feasible.

4.3.2 El Niño-Southern Oscillation

The scientific question in this section slightly differs the one from the last section, as the quasi-oscillatory behaviour of ENSO is prescribed by the boundary CMIP6 SST data. For this reason, the focus in this section lies on the effect of ENSO on the extratropical atmospheric circulation in ICON compared to ERA-Interim. The theoretical background on ENSO is given in Section 2.3.2. In contrast to ERA-Interim, ICON does not simulate a QBO (cf. Section 4.3.1). The QBO has been recognized to actively modulate the timing of ENSO (Gray et al., 1992). The ENSO effects in ICON are therefore undisturbed by the oscillatory behaviour of the QBO.

The mean effect of warm ENSO events on the temperature of the polar atmosphere is visualised as a composite time-height cross section in Figure 4.27 for ERA-Interim (a),

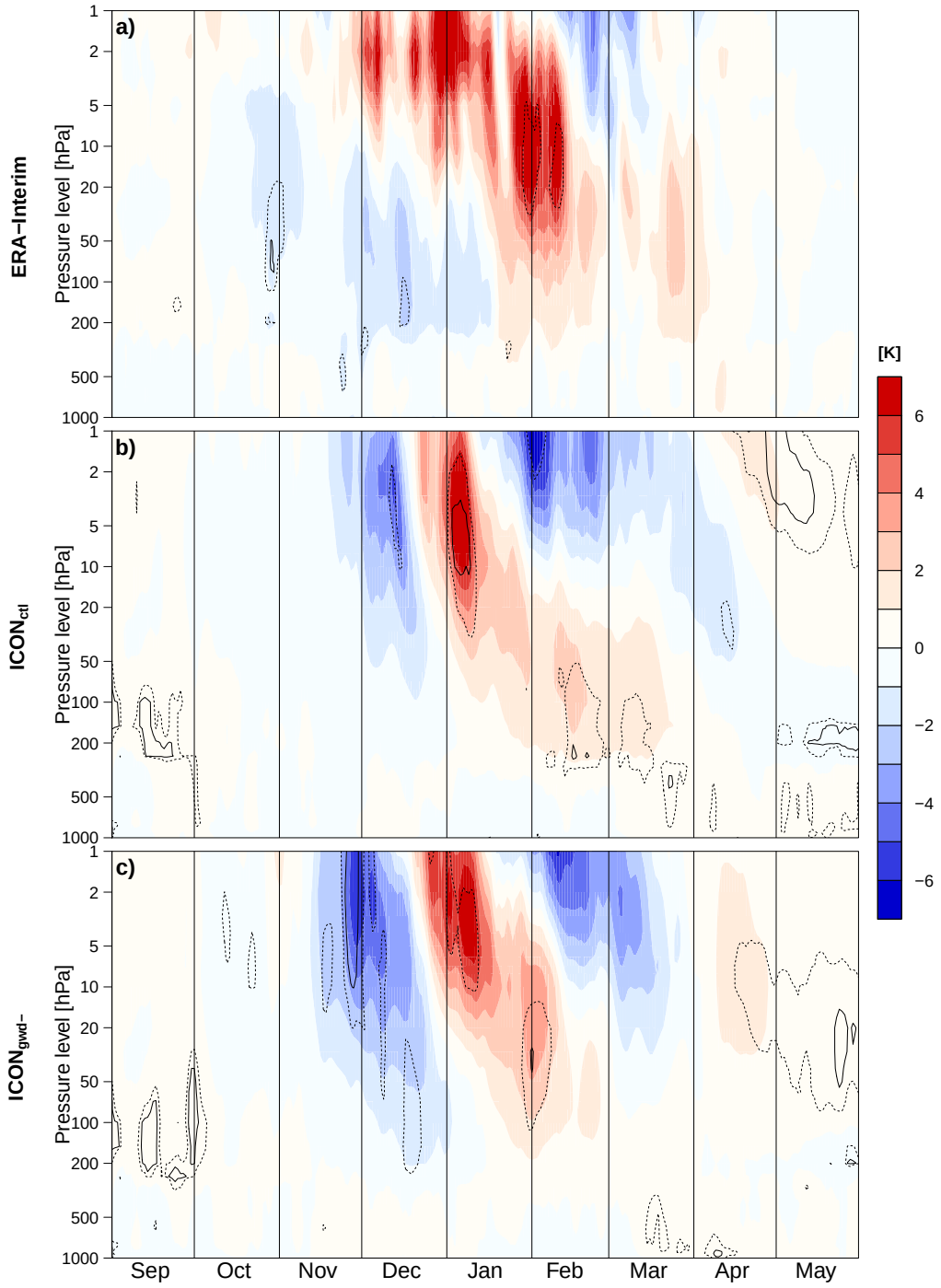

Fig. 4.27.: Time-height cross section of climatological mean temperature anomalies of the wENSO composite for the polar cap mean (65.25° N to 90° N). Composite anomalies (wENSO - climatology) for ERA-Interim (a), ICON$_{ctl}$ (b) and ICON$_{gwd-}$ (c). Dashed/solid lines indicate statistical significance at the 95/99% level according to a two-sided Wilcoxon-test.

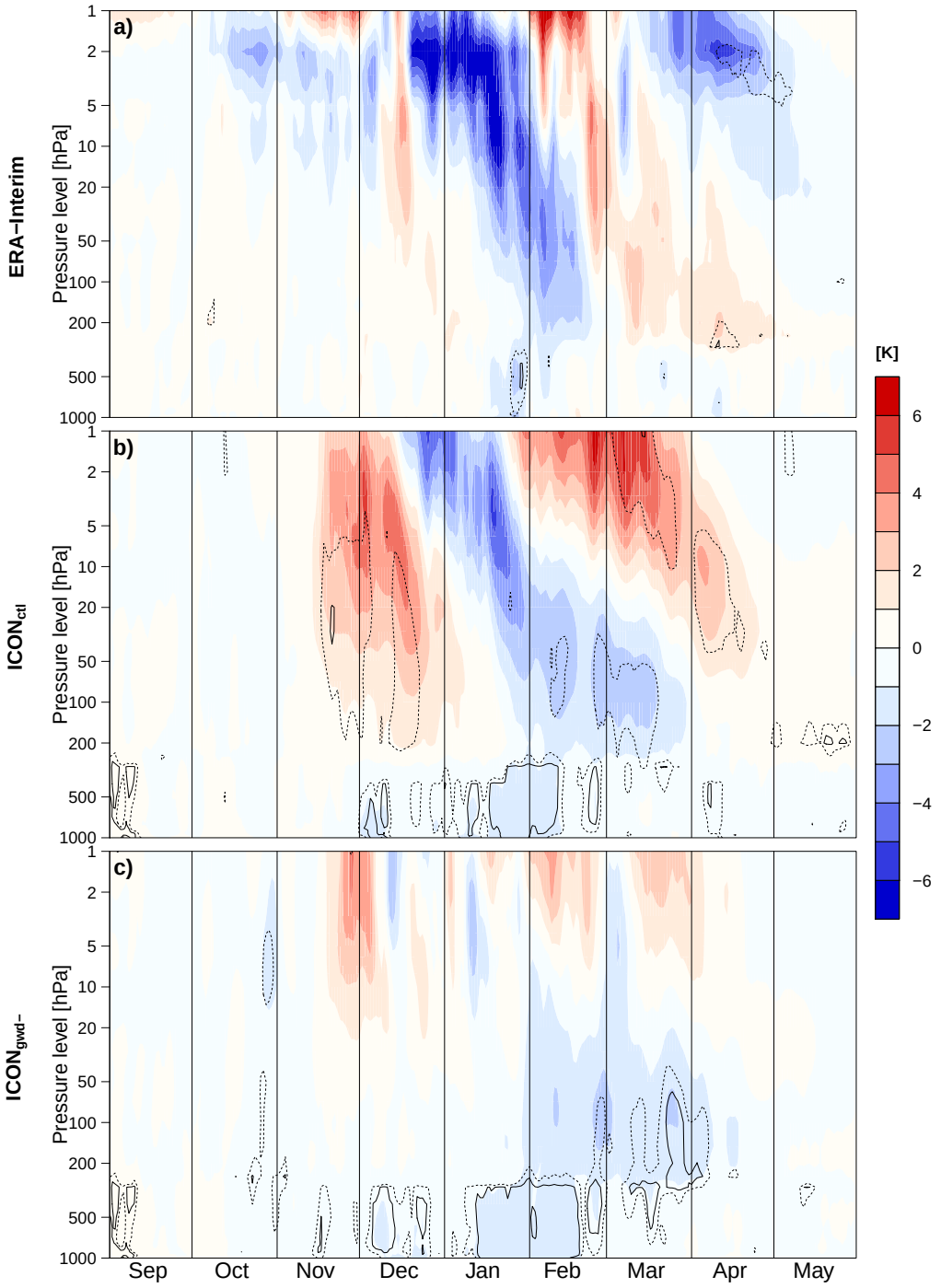

Fig. 4.28.: Time-height cross section of climatological mean temperature anomalies of the cENSO composite for the polar cap mean (65.25° N to 90° N). Composite anomalies (cENSO - climatology) for ERA-Interim (a), ICON$_{ctl}$ (b) and ICON$_{gwd-}$ (c). Dashed/solid lines indicate statistical significance at the 95/99% level according to a two-sided Wilcoxon-test.

ICON$_{ctl}$ (b) and ICON$_{gwd-}$ (c). The method for creating the composites is based on the Niño 3.4 index and is described in Section 3.3.3. In wENSO winters the polar stratosphere is significantly warmer in January and February (cf. Fig. 4.27 a). This anomaly is preceded by a weak, but partly significant cold anomaly in the mid and lower stratosphere in autumn and December. The warm anomaly is connected to a weakened stratospheric polar vortex in late winter and propagates downward in time. The positive anomalies remain in the lower stratosphere until April, however, this signal in spring is not significant. The weakened vortex in warm ENSO phases is in accordance with earlier literature and has been connected to an increase in wave 1 forcing due a deepening of the wintertime Aleutian low via the PNA pattern (Garfinkel and Hartmann, 2008). Both ICON ensemble simulations reproduce this stratospheric reaction to wENSO. The significant stratospheric warm anomaly starts in the upper stratosphere in early January and propagates downward to the lower stratosphere by February. This warm anomaly remains significant in the lower stratosphere and upper troposphere in March in ICON$_{ctl}$, but not in ICON$_{gwd-}$. As in ERA-Interim, the positive anomalies are preceded by negative anomalies in late autumn and December. These are more pronounced and significant in ICON$_{gwd-}$. The fact that reanalysis and model results agree on the basic pattern, reinforces the validity of the stratospheric reaction to the ENSO.

The same composite analysis as above, but for cENSO events is outlined in Figure 4.28. The stratospheric pattern of cENSO events is similar to the wENSO pattern, but with the opposite sign. However, the cooling of the polar stratosphere does not appear to be significant in ERA-Interim. ICON$_{ctl}$ reproduces the basic features of the downward propagating negative anomaly. Statistical significance at the 95% level for this anomaly is given only in February and March. The stratospheric cooling is preceded and followed by significant warming, which is only partly visible in ERA-Interim. ICON$_{gwd-}$ exhibits very little stratospheric anomalies, limited to the lower stratosphere in January and February, a feature that agrees to ERA-Interim in February only. Both ICON experiments exhibit significant cooling in the troposphere, a feature that is to a lesser extent also visible in ERA-Interim. Overall, the stratospheric signals of cENSO are less pronounced. However, they suggest a partly significant cooling of the polar atmosphere in January and February.

To further investigate the potential influence of ENSO on the extratropical troposphere and its potential for improved seasonal prediction, Figures 4.29 and 4.30 depict the MSLP anomalies for wENSO and cENSO composites. The monthly mean polar stereographic projections are shown for ERA-Interim, ICON$_{ctl}$ and ICON$_{gwd-}$ for the months December to March. The composites, however, were constructed with a focus on winter only (cf. Section 3.3.3).

The first column of Figure 4.29 depicts the ERA-Interim MSLP anomaly of the wENSO composite. The most consistent feature in all displayed months is the significant negative MSLP anomaly in the eastern North Pacific, which is related to the positive phase of the PNA (e.g Lau, 1997). In December further significant extratropical anomalies are only visible over Japan. Although anomalies are also visible in the Atlantic-European sector, these are not statistically significant. In January the significant negative MSLP anomaly stretches across the United States into the North Atlantic sector. With positive MSLP anomalies over the Arctic

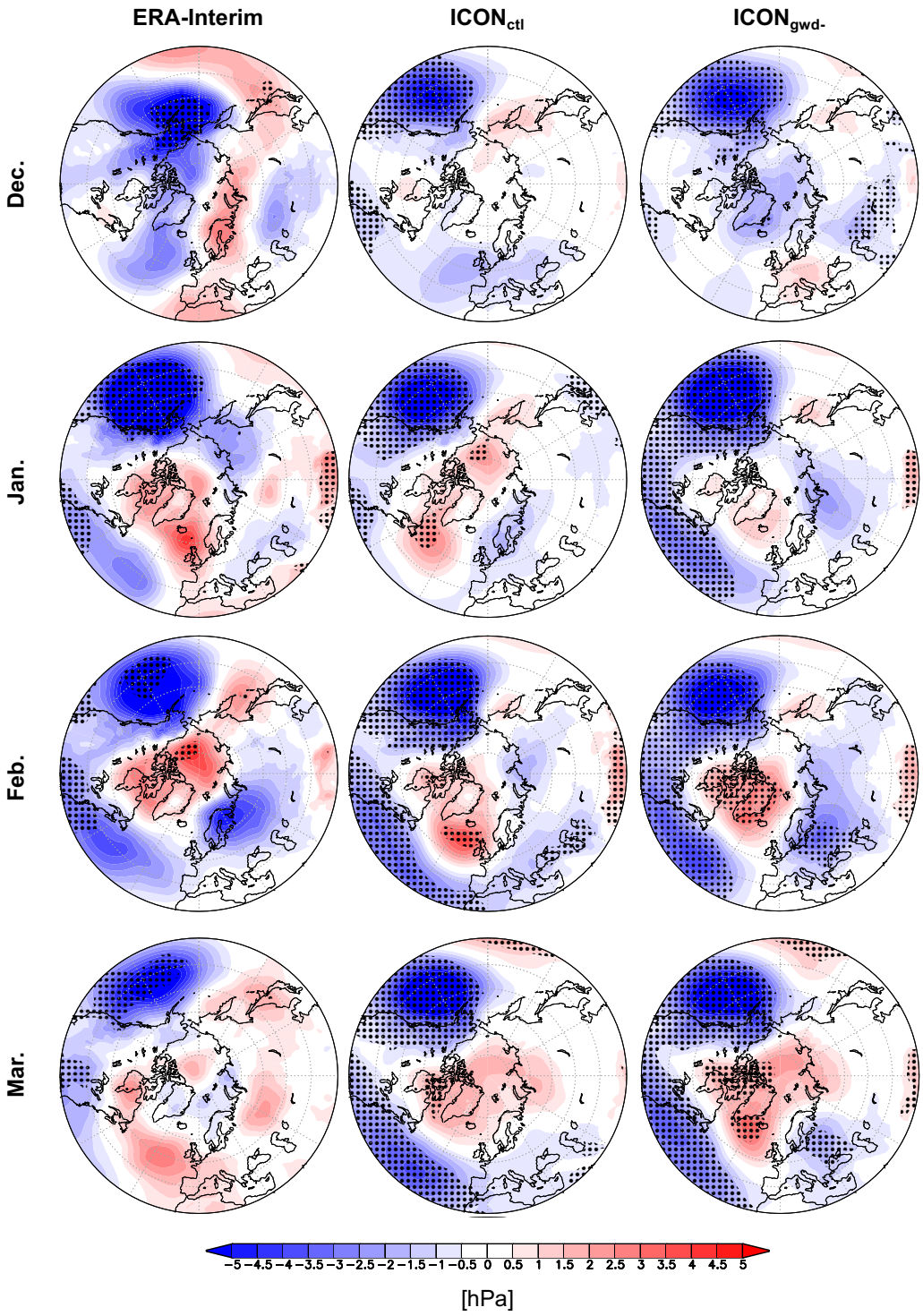

Fig. 4.29.: MSLP wENSO composite anomalies for ERA-Interim (left column), ICON$_{ctl}$ (middle column) and ICON$_{gwd-}$ (right column). The wENSO anomalies are shown for the months December - March. Stippling indicates statistical significance at the 95% level according to a two-sided Wilcoxon-test.

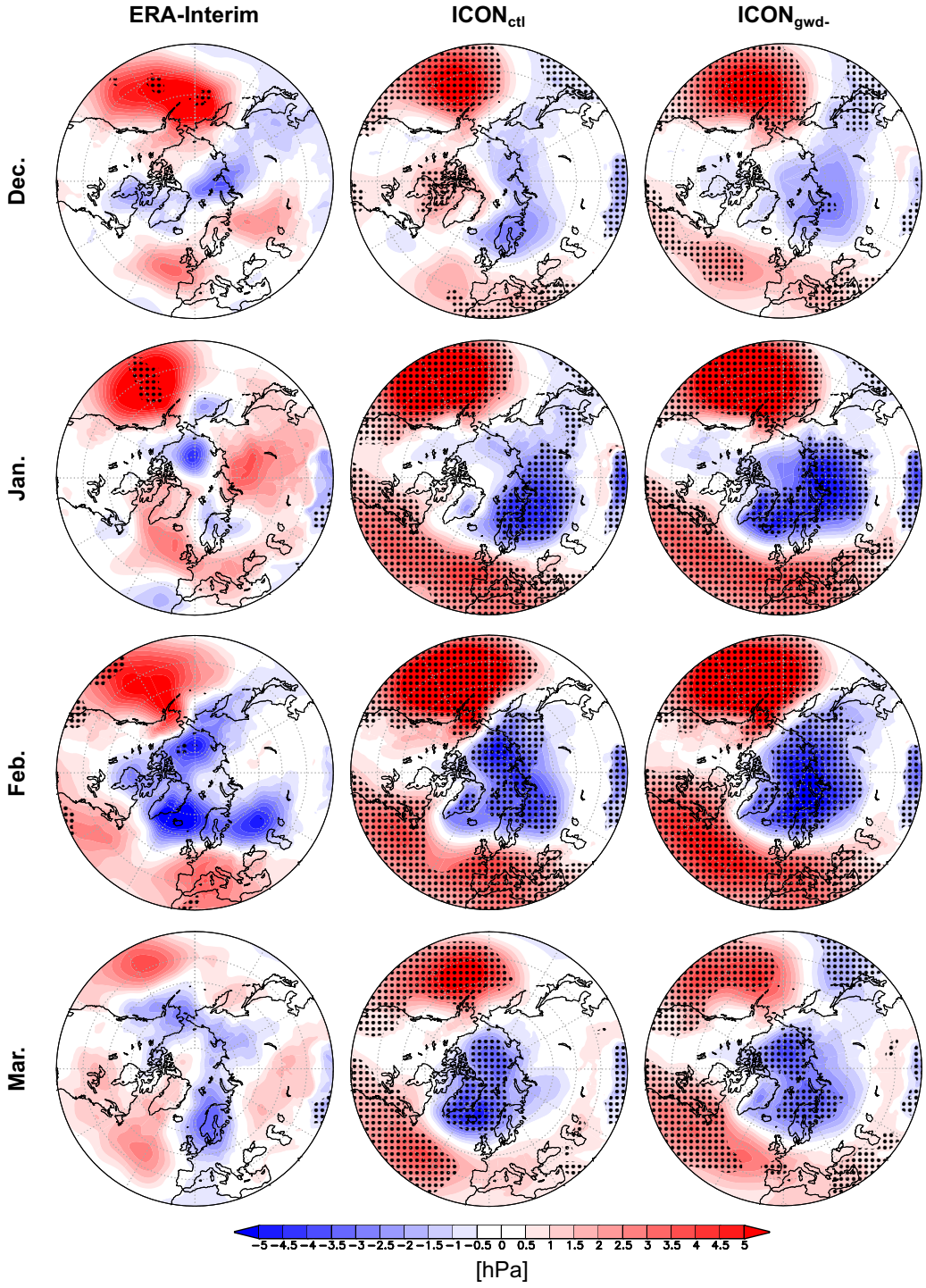

Fig. 4.30.: MSLP cENSO composite anomalies for ERA-Interim (left column), ICON$_{ctl}$ (middle column) and ICON$_{gwd-}$ (right column). The cENSO anomalies are shown for the months December - March. Stippling indicates statistical significance at the 95% level according to a two-sided Wilcoxon-test.

the pattern is starting to resemble the negative phase of the AO. In February this pattern is intensified with significant positive anomalies in the Arctic and negative anomalies across the Atlantic. The wENSO anomalies decrease in March, so that significant differences are only visible in the Pacific and over the eastern United States. The ICON ensemble simulations reproduce the basic MSLP reaction to wENSO. Again, the most consistent pattern is the strong and significant negative anomaly in the Pacific. In December both ICON simulations furthermore agree on a significant MSLP reduction along the east coast of the United States, a signal also visible in the reanalysis, however not significant. As in the reanalysis, in January significant negative anomalies stretch across the United States into the Atlantic region. This is especially pronounced for ICON$_{gwd-}$. In February the negative AO pattern is intensified and in particular ICON$_{gwd-}$ closely resembles the ERA-Interim pattern. The ICON simulations show significant positive MSLP anomalies in the Arctic and significant negative anomalies in the Pacific, across the United States and the Atlantic and in parts of Europe. These results confirm the studies stating that wENSO has significant impact on European weather in late winter. The downward propagating warm polar stratospheric signal seems to strongly contribute to the negative AO pattern in January and February. The negative AO pattern further persists in March in the ICON simulations, a feature only partly visible in the reanalysis.

The MSLP anomaly of the cENSO composite for ERA-Interim is depicted in the first column of Figure 4.30. The Pacific anomaly is again most consistent and significant. Cold ENSO events are connected to the negative phase of the PNA with strong positive MSLP anomalies in the North Pacific region. In December and January this is the only significant extratropical signal. The cENSO signal intensifies in February and strongly resembles the positive phase of the AO: negative anomalies in the Arctic and positive anomalies in the Pacific, Atlantic and western and southern Europe. These anomalies are statistically significant over the Chukchi Sea, the eastern Pacific, the western Atlantic and north-western Africa. These patterns weaken and become non-significant in March. The ICON simulations are once more able to capture the basic MSLP reactions to cENSO. The Pacific anomalies are highly significant in all months. In December there are statistically significant MSLP reductions over Japan and significant MSLP increases over the Mediterranean Sea and western Europe as well as parts of the Atlantic, features that are also partly visible in the reanalysis. The ICON cENSO anomalies in January and February are highly significant and strongly resemble the positive phase of the AO. In particular in February, this pattern is in good agreement with the ERA-Interim results. This pattern also remains in March, but is weakened in its amplitude.

The results in this section clearly support the statement, that ENSO also has a significant on the European weather (Brönnimann, 2007). This accounts for late winter in particular, where wENSO is associated with the negative phase of the AO and cENSO with the positive phase. The signals are strong enough, so that the extreme phases of ENSO could help to improve the skill of seasonal predictability over Europe. The stratospheric pathway plays a larger role for the wENSO anomalies. The ENSO signal seems to be linked to the AO via the PNA. The effect of the adjusted gravity wave drag parameterisations on the ENSO signals is small.

4.4 Arctic-midlatitude linkages

Different studies have connected AA to changing mid-latitude weather patterns (cf. Section 2.3.3). AA has led to strong sea ice loss, which again accelerates AA. The Arctic sea ice extent reaches its minimum in September and peaks in March. Due to climate change and AA, the sea ice extent in all months has strongly declined the last decades, however strongest sea ice reductions are visible in September. Regional patterns of sea ice loss can force anomalous planetary waves (Honda et al., 2009) leading to an increase of planetary wave flux into the stratosphere in high latitudes in autumn and early winter (Jaiser et al., 2012; Jaiser et al., 2013). Due to a weakening of the stratospheric polar vortex through the absorption of upward-propagating wave energy, the stratosphere has been found to steer the AO toward its negative phase in winter (Mori et al., 2014; Kretschmer et al., 2016; Mori et al., 2019). This proposed mechanism links Arctic sea ice in autumn to mid-latitude circulation in winter. Reliable data of the Arctic sea ice extent exists since 1979, the start of the modern satellite era. The monthly sea ice extent in September is outlined in Figure 4.31 for the years 1979 to 2017. This period can be subdivided into two phases with largely differing mean sea ice extent (e.g. Jaiser et al., 2013): An early period (1979-1999) with an average September sea ice extent of nearly 7 million km^2 and a late period (2000-2017) with just over 5 million km^2. Since 1997 no September mean sea ice has exceeded the mean of the early period. To exhibit how these changes affect the atmospheric circulation, in the following, the differences between these two periods will be investigated. Keeping in mind, however, that not only the sea ice extent has changed recently, but also the volume mixing ratios of greenhouse gases as well as oceanic boundary forcing. A sensitivity experiment, which involves sea ice changes only will be presented in the last Section 4.4.3.

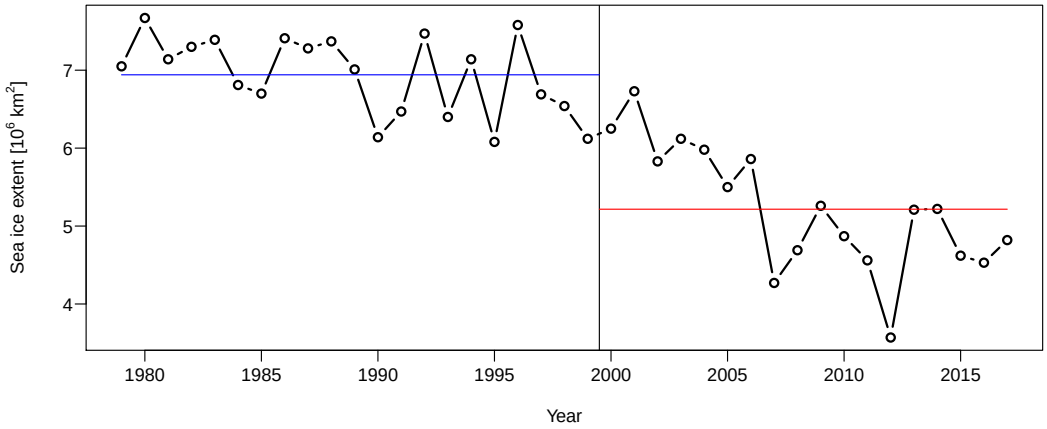

Fig. 4.31.: September sea ice extent from 1979-2017. The blue line denotes the mean sea ice extent from the early period (1979-1999), the red line denotes the mean sea ice extent from the late period (2000-2017). Data from National Snow and Ice Data Center (Fetterer et al., 2017).

4.4.1 Tropospheric processes

The sea ice scheme in ICON accounts for thermodynamic processes only and does not include ice rheology (Mironov et al., 2012). It derives the ice surface temperature and thickness from prescribed sea ice fractions. The scheme is initialised with a ice thickness of 1 meter in September. In areas with mixed cells including sea ice and open water, the thickness is reduced according to the sea ice fraction of the cell. Figure 4.32 shows the derived mean sea ice thickness from September to May for the climatology of ICON$_{ctl}$. The sea ice thickness increases unit April and then slowly decreases in May. The maximum sea ice thickness is simulated north of the Canadian Archipelago with up to 2.15 m in April. Overall, the sea ice scheme produces a realistic distribution of Arctic sea ice thickness (e.g. Laxon et al., 2013). However, initialising with a thickness of 1 m may effect the simulation quality. Day et al. (2014) showed that an initialization including sea ice thickness can help to improve seasonal forecast skill.

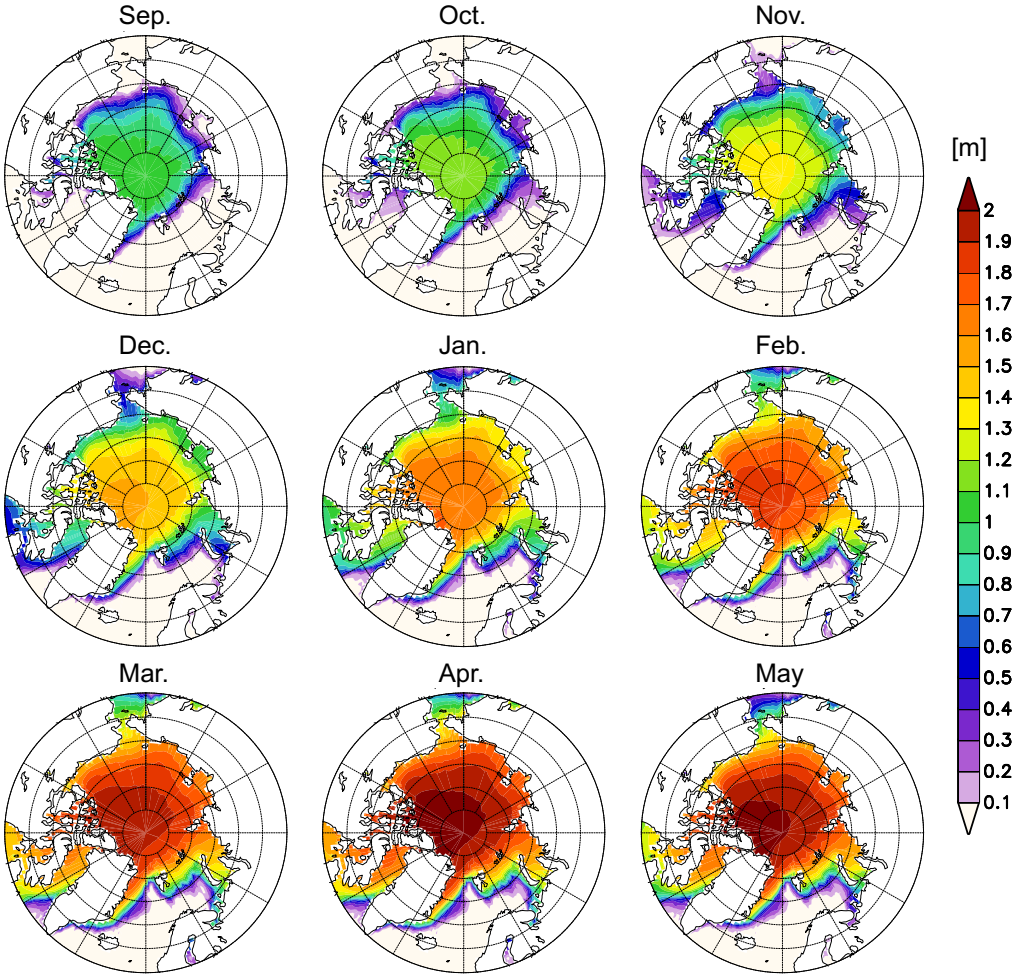

Fig. 4.32.: ICON monthly mean sea ice thickness from the long term and ensemble mean of ICON$_{ctl}$.

The AA can be assessed by visualising the differences between the late (2000-17) and early (1979-2000) period. The seasonal differences of the temperature in 2 m is presented in Figure 4.33 for ERA-Interim, ICON$_{ctl}$ and ICON$_{gwd-}$. The Arctic region in the ERA-Interim reanalysis is dominated by significant warming in the late period. Largest seasonal mean differences are visible in winter, where they amount up to 8 K in the northern Barents Sea. The fact that the Arctic exhibits the largest warming in all seasons exemplifies the AA. Also most lower latitudes are characterised by significant warming due to climate change. However, a strong cooling in the late period is visible over Asia. This cooling pattern is visible in all three winter months with slightly shifted locations. Strongest and significant cooling is present in December and February. The described pattern is referenced to as "warm Arctic-cold-Siberia" (Inoue et al., 2012) or “warm Arctic-cold continents” (Overland et al., 2011). Furthermore, temperatures over North America have remained stable in winter and are partly subject to cooling in spring. With a background of global warming, these cooling patterns can only be explained by changes in the circulation patterns. Different studies have linked these changes partly to AA (e.g. Cohen et al., 2014). This linkage, however, is still largely discussed in the community and other authors argue that the cooling represents a strong articulation of internal atmospheric variability (e.g. Sun et al., 2016, cf. Section 2.3.3).

The control ICON experiment ICON$_{ctl}$ as well as the current optimal setup with reduced gravity wave drag ICON$_{gwd-}$ reproduce the AA (cf. Fig. 4.33 d-i). The 2 m temperature difference patterns of both experiments are much alike in all seasons. The AA in ICON is slightly underestimated in winter and more strongly underestimated in spring. The “warm Arctic-cold continents” pattern is hardly reproduced by the ICON ensembles. There is no Asian cooling pattern and only a weak and non-significant cooling pattern in the northwest of North America. The weaker AA in winter and spring in ICON is consistent with the absent mid-latitude cooling patterns, as the processes that lead to advection of warm air into the Arctic are the same as the processes that lead to advection of cold air into the mid-latitudes (e.g Dahlke and Maturilli, 2017). Cohen et al. (2020) discusses this divergence between the observational evidence and results from modelling studies. Whereas most observational studies argue that AA forces winter cooling across the mid-latitude continents, most modelling experiments do not. Therefore, many modelling studies argue that the observed mid-latitude winter continental cooling pattern is due to natural variability. To further investigate, why the reanalysis shows theses cooling trends, whereas the ICON simulations do not show it, dynamical changes between the two periods will be further assessed in the following. While the monthly mean patterns of the 2 m temperature only slightly differ from each other in each season, this is not the case for the MSLP difference patterns. Hence, the monthly mean MSLP differences are analysed in the following.

Figure 4.34 illustrates the monthly mean autumn MSLP differences between the late and the early period for ERA-Interim, ICON$_{ctl}$ and ICON$_{gwd-}$. The AA in September is connected to a significant pressure reduction in the Arctic and a significant increase in the northern Pacific and in northern Europe. The ICON simulations agree with the reanalysis, ICON$_{gwd-}$ exhibits particularly similar results. The good agreement between reanalysis and simulation results can be explained by the fact that ICON is initialised with ERA-Interim data. The

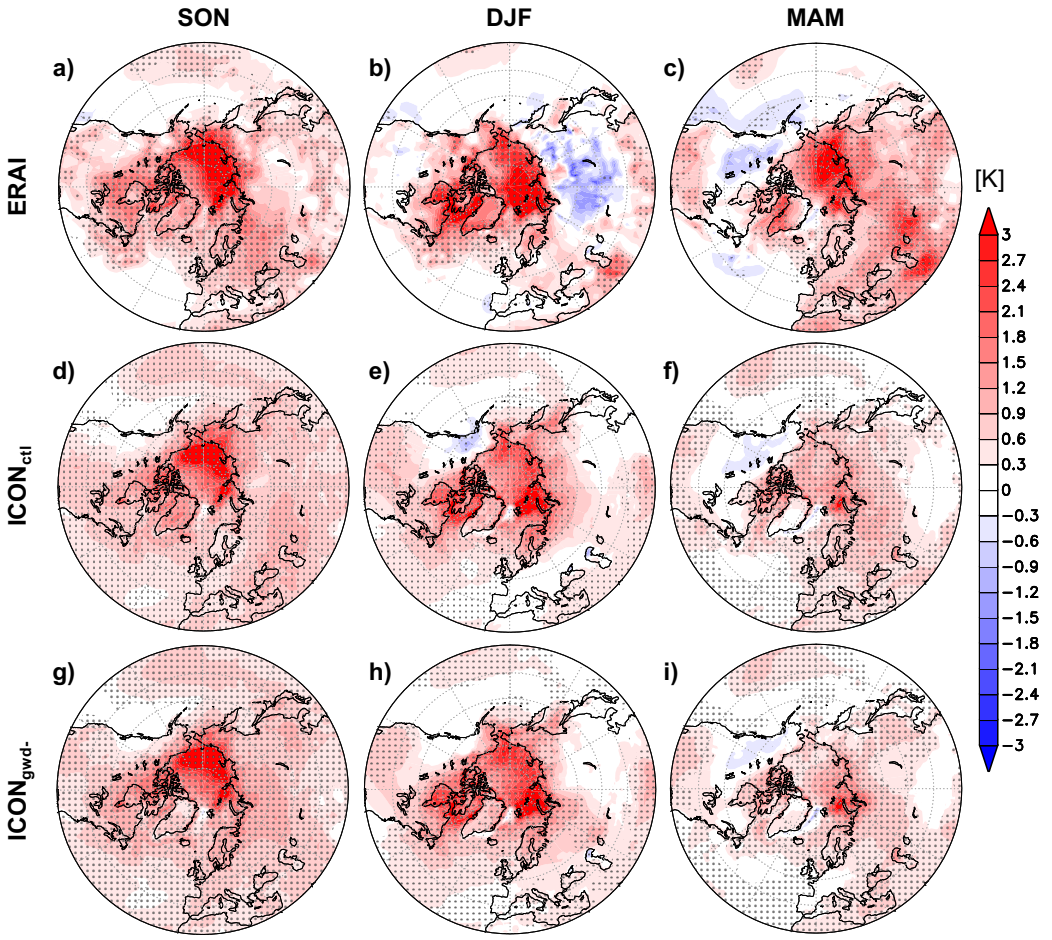

Fig. 4.33.: Late (2000-17) - early (1979-2000) differences in the 2 m temperature for autumn, winter and spring. Seasonal means ERA-Interim (a-c), ICON$_{ctl}$ (d-f) and ICON$_{gwd-}$ (g-i) data. Stippling indicates statistical significance at the 95% level according to a two-sided Wilcoxon-test.

difference pattern in October resembles the negative phase of the AO, significant differences in ERA-Interim are, however, only visible in the Atlantic sector. The ICON simulations do not reproduce this patterns and also differ among each other. November is characterised by a significant MSLP increase in the northern Pacific, across North America and in the North Atlantic. The ICON simulations reproduce this pattern in North America and in the Pacific. In total, autumn is characterised by rather small-scale difference patterns, that vary largely between the different months.

The monthly mean winter MSLP differences between the late and the early period are displayed in Figure 4.35. December is characterised by a significant intensification and shift of the Siberian high pressure system. This intensification and westward expansion of the Siberian high has been linked to an increase in Eurasian snow cover in autumn (Cohen et al., 2012). Declining sea ice in the Barents and Kara Seas acts as moisture source and leads to this snow cover increase in autumn (Wegmann et al., 2015). Thus, the Siberian cooling

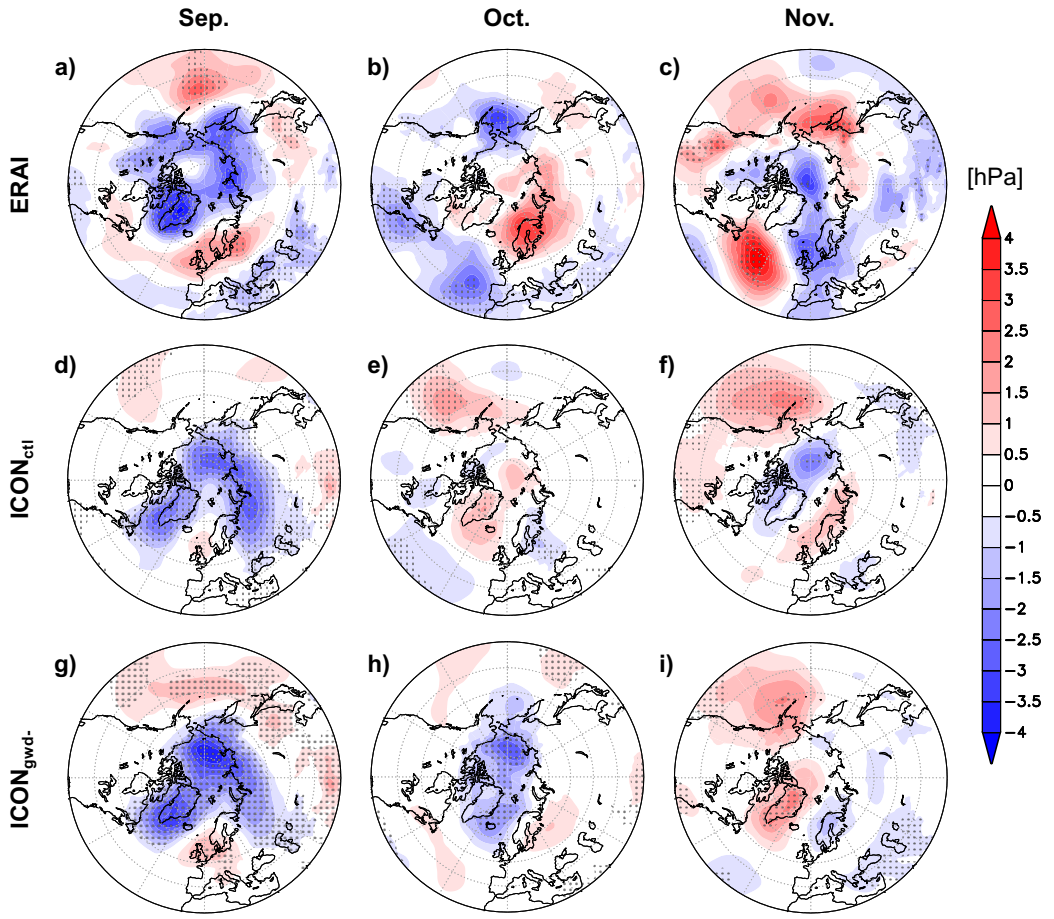

Fig. 4.34.: Late (2000-17) - early (1979-2000) differences in the MSLP for September, October and November. Monthly means of ERA-Interim (a-c), ICON$_{ctl}$ (d-f) and ICON$_{gwd-}$ (g-i) data. Stippling indicates statistical significance at the 95% level according to a two-sided Wilcoxon-test.

pattern in December, which largely contributes to the winter cooling pattern (cf. Fig. 4.33), is induced by the strengthened Siberian high. These mechanisms are not reproduced by ICON. The high pressure pattern in ERA-Interim shifts towards the Ural and Scandinavia in January. Crasemann et al. (2017) demonstrated that the Scandinavian blocking pattern occurs more frequently in December and January for low Arctic sea ice conditions. Whereas ICON$_{ctl}$ does not reproduce this pattern and favours a significant positive AO pattern in January, ICON$_{gwd-}$ reproduces this pattern partly. It shows a significant strengthening and expansion of the Siberian high as well as significantly reduced MSLP over southern Europe in January. The largest differences between the late and the early period in the reanalysis are visible in February: the late period exhibits a significant MSLP increase in the northern Pacific, a partly significant MSLP reduction over Europe and across the Atlantic as well as a pressure increase over the Arctic. The Atlantic part of this pattern closely resembles the negative phase of the NAO. Different studies have connected the increase in the negative

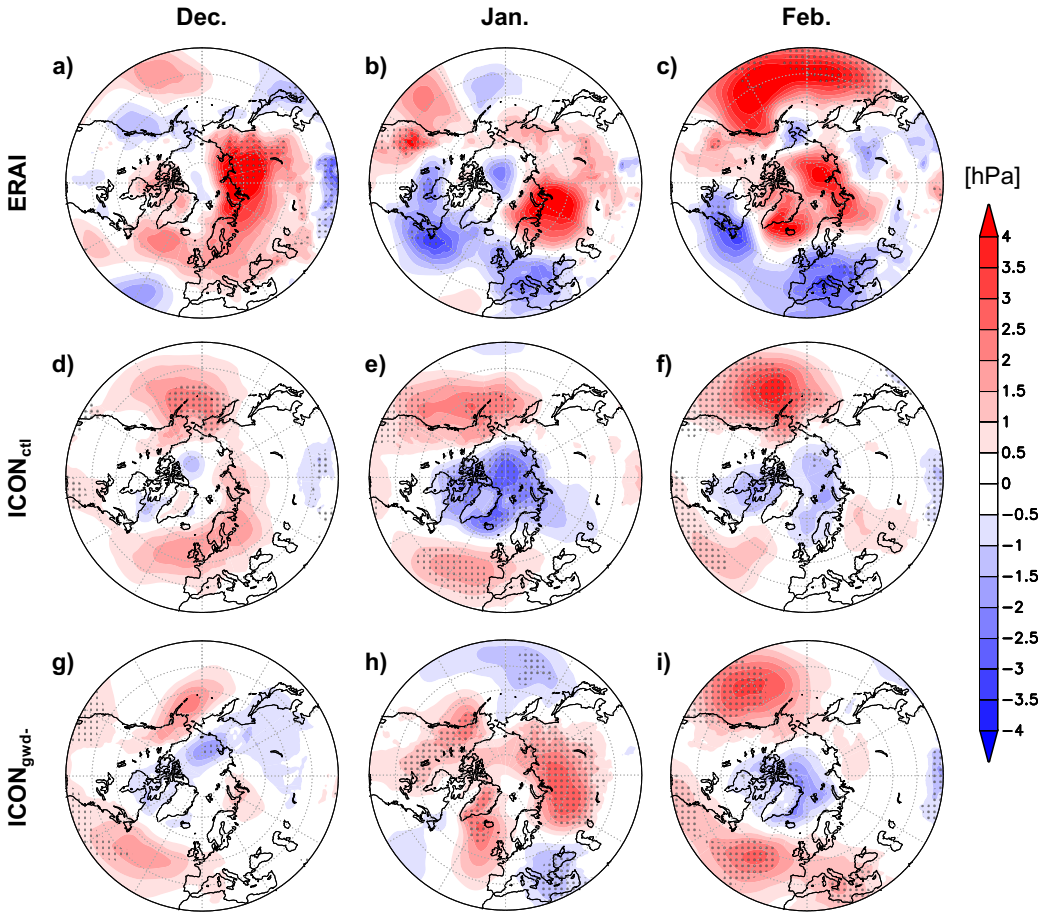

Fig. 4.35.: Late (2000-17) - early (1979-2000) differences in the MSLP for December, January and February. Monthly means of ERA-Interim (a-c), ICON$_{ctl}$ (d-f) and ICON$_{gwd-}$ (g-i) data. Stippling indicates statistical significance at the 95% level according to a two-sided Wilcoxon-test.

NAO frequency in late winter to AA and sea ice loss in autumn (e.g Nakamura et al., 2015; Crasemann et al., 2017). Various studies suggest a stratospheric pathway, in which vertically propagating waves in autumn and early winter interact with the stratospheric polar vortex and weaken it (e.g Nakamura et al., 2016; Jaiser et al., 2016; Romanowsky et al., 2019). These anomalous signals propagate downward into the troposphere and favour a negative phase of the NAO in late winter. The stratospheric pathway will be discussed in more detail in the following Section 4.4.2. The ICON simulation do no reproduce the negative NAO reaction in February and in contrast favour a significant positive AO pattern in late winter. This could be the consequence of an absent stratospheric pathway (cf. Section 4.4.2). The Pacific MSLP increase, however, is simulated realistically.

The ERA-Interim MSLP difference pattern for March resembles the one from February (cf. Fig. 4.36). With increased pressure in the Icelandic region and decreased pressure in the Atlantic, European and Asian region it furthermore still resembles the negative phase of the

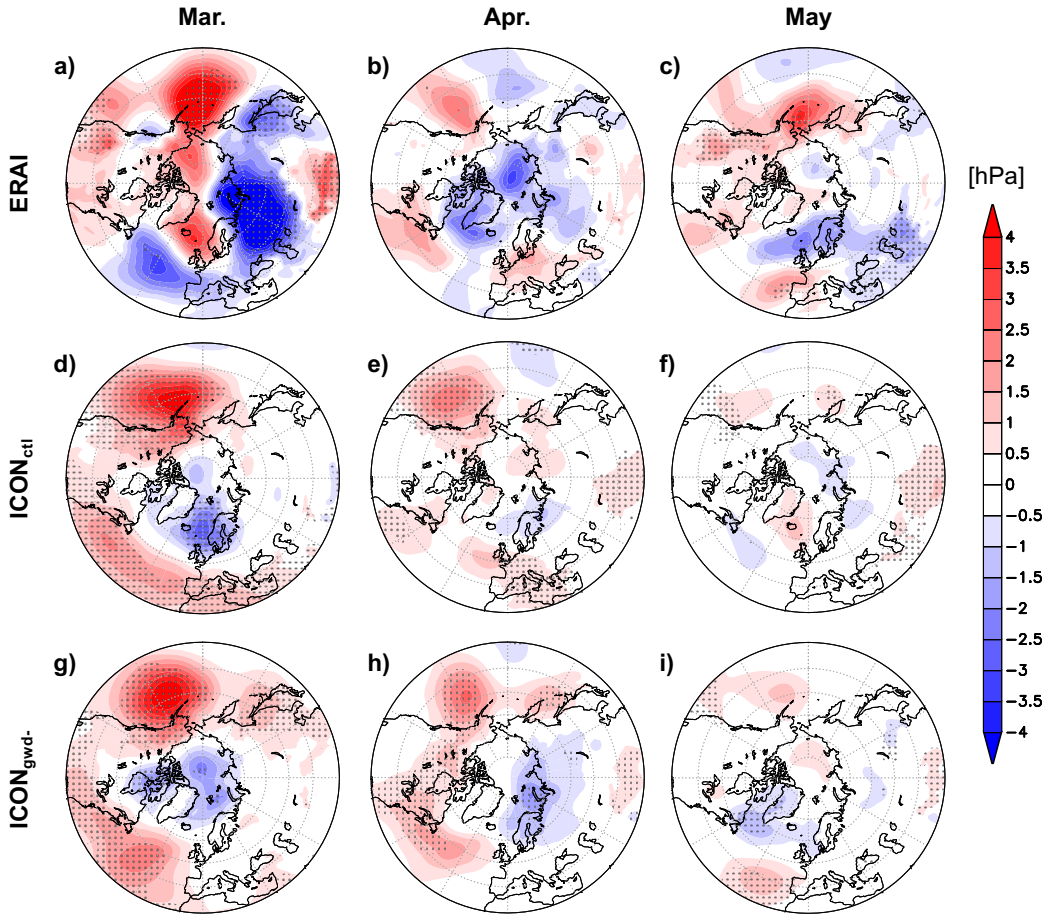

Fig. 4.36.: Late (2000-17) - early (1979-2000) differences in the MSLP for March, April and May. Monthly means of ERA-Interim (a-c), ICON$_{ctl}$ (d-f) and ICON$_{gwd-}$ (g-i) data. Stippling indicates statistical significance at the 95% level according to a two-sided Wilcoxon-test.

NAO. This pattern in early spring is still strongly connected to the stratospheric pathway. As in February, significant positive differences are visible over the northern Pacific and across large parts of North America. The ICON patterns also strongly resemble the ones from February. Both simulation reproduce the Pacific pattern, but fail to reproduce the Atlantic negative NAO pattern. In April there is a shift towards the positive phase of the AO in the late period. However, the difference patterns are a lot weaker and mostly not statistically significant. The ICON simulations reproduce this pattern and exhibit significant differences over the Pacific and Atlantic. The ERA-Interim difference pattern in May is rather chaotic and a significant MSLP increase, which is also reproduced by ICON, is visible along the west coast of North America.

The MSLP patterns showed that there are significant differences between the late and the early period. In ERA-Interim, the early winter is characterised by an increase in Eurasian high pressure systems that have been linked to blocking patterns. In late winter and early

spring a negative NAO pattern is visible. The described patterns have been connected to AA by earlier studies (cf. Section 2.3.3). The ICON simulations demonstrate some of the features, however, fail to reproduce the patterns that have been linked to the stratospheric pathway and favour a positive AO in most months. In the following section the stratospheric pathway will be investigated.

4.4.2 Stratospheric pathway

The stratospheric pathway has been recognised as a important conduit between AA and a negative NAO response, and thus a weakened jet stream, in late winter (Vavrus, 2018). The negative NAO response is a consequence of the downward propagating disturbance of the stratospheric vortex. This downward propagating process will be analysed in the following by illustrating the polar cap mean temperature difference between the late and early period (cf. Jaiser et al., 2016; Romanowsky et al., 2019). Figure 4.37 depicts this for ERA-Interim and the two ICON experiments ICON$_{ctl}$ and ICON$_{gwd-}$.

AA and the negative NAO response have been related to the downward propagating, strongly positive temperature signal, which is visible in ERA-Interim in winter (cf. Fig. 4.37 a). It originates in the upper stratosphere in early winter and is linked to an increase in the vertical propagation of planetary waves (Jaiser et al., 2016). The positive temperature signal becomes statistically significant as it reaches the lower stratosphere in late winter. The increase in the stratospheric polar cap mean temperatures is linked to a decrease in the strength of the polar vortex. As demonstrated by Baldwin and Dunkerton (2001), stratospheric anomalies are able to propagate into the troposphere and influence the AO. AA is clearly visible in the troposphere, where temperatures are significantly higher in the late period. It is particularly pronounced in autumn, concurrent with the maximum sea ice loss. The downward propagating warm signal is preceded and followed by significant cold anomalies in the upper stratosphere. This background stratospheric cooling in the late period can be explained by radiative effects due to changing CO_2, ozone and water vapor (e.g. Goessling and Bathiany, 2016; Yang et al., 2016).

The polar cap mean temperature differences from ICON$_{ctl}$ and ICON$_{gwd-}$ are illustrated in Figures 4.37 b and c. Both simulations exhibit significant tropospheric warming in the polar region. The warming is less pronounced in ICON compared to ERA-Interim. The stratospheric pattern differs largely from the reanalysis pattern. The stratosphere in the late period in ICON$_{ctl}$ is on average colder than in the early period. This cooling pattern is significant in autumn and late spring and can be attributed mainly to the CO_2 difference between the two periods. Winter exhibits no large significant patterns, which demonstrates that there is clearly no stratospheric pathway for Arctic-midlatitude linkages in ICON$_{ctl}$. This also explains why it does not show the negative NAO reaction in late winter (cf. Section 4.4.1). The on average underestimated strength of the stratospheric polar vortex in ICON$_{ctl}$ could inhibit this stratospheric pathway. ICON$_{gwd-}$ exhibits similar patterns in the troposphere as well as in the stratosphere in autumn and in spring. However, it exhibits significant stratospheric signals in early winter: increased stratospheric temperatures in late

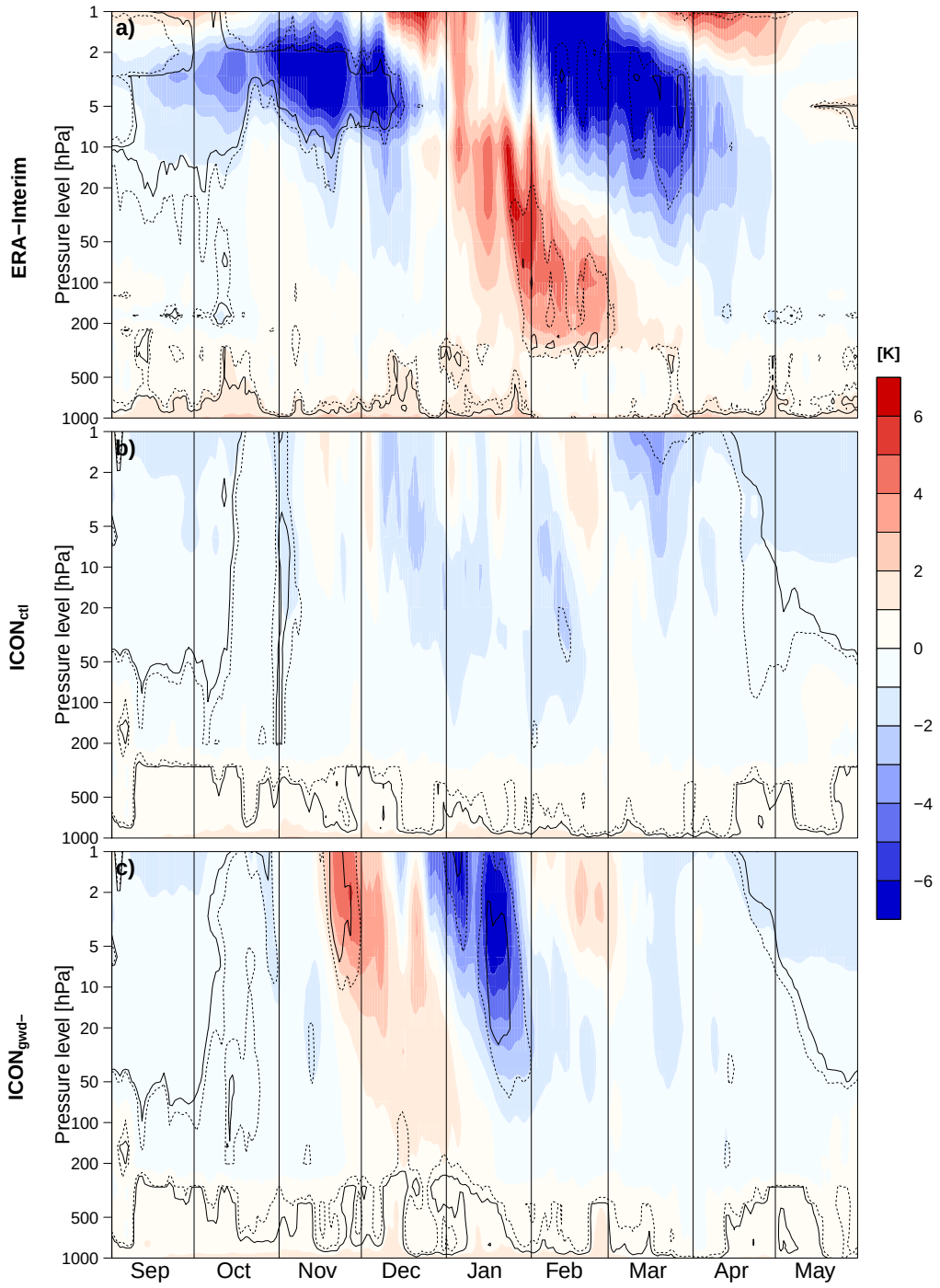

Fig. 4.37.: Time-height cross section of climatological mean temperature differences of the late (2000-17) and early (1979-2000) period for the polar cap mean (65.25° N to 90° N). Dashed/solid lines indicate statistical significance at the 95/99% level according to a two-sided Wilcoxon-test.

November and December and decreased temperatures in January. Although the timing of the anomalies shows an approximate phase shift of 1-2 months compared to ERA-Interim, the knowledge that the reduction of the gravity wave drag and thus the strengthening of the vortex, has an effect on the stratospheric pathway, could help to further improve this behaviour ICON. Hence, further bias reduction in the stratospheric circulation could contribute to a more realistic representation of these linkage mechanisms.

4.4.3 Sea ice sensitivity experiment

The late minus early period approach from the two previous sections has the disadvantage, that it is hard to disentangle the influence of AA from changing SST, volume mixing ratios of greenhouse gases or influences form other regions, such as the Tropics. To isolate the impact of Arctic sea-ice retreat, two sensitivity experiments that only differ in their sea-ice concentrations are performed. Average sea ice concentrations from 1979 to 1983 and 2005 to 2009 are used to simulate the high-ice (HICE) and low-ice conditions (LICE). This approach is based on Nakamura et al. (2015) and Jaiser et al. (2016), who used it to investigate the effects sea ice loss in the atmospheric model AFES (Atmospheric general

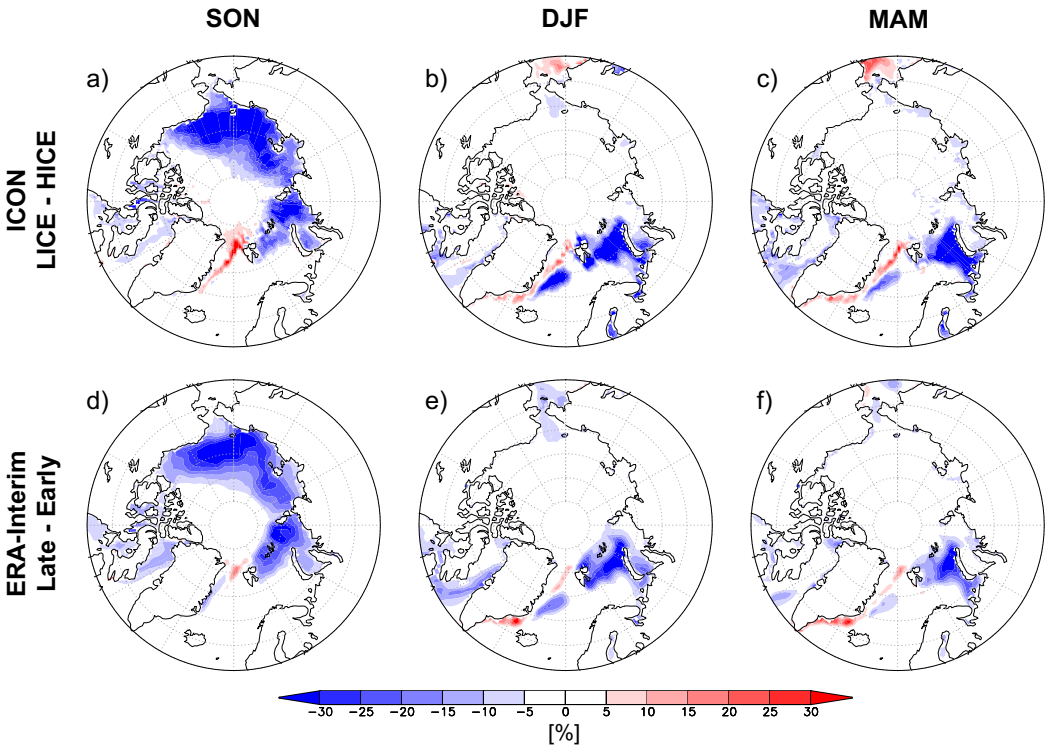

Fig. 4.38.: Seasonal mean sea ice content differences between ICON LICE (2005-2009) and HICE (1979-1983) in a-c and between ERA-Interim late (1979-2000) and early (2000-2017) period in d-f. The sea ice content is given in percent for the seasons autumn (SON), winter (DJF) and spring (MAM).

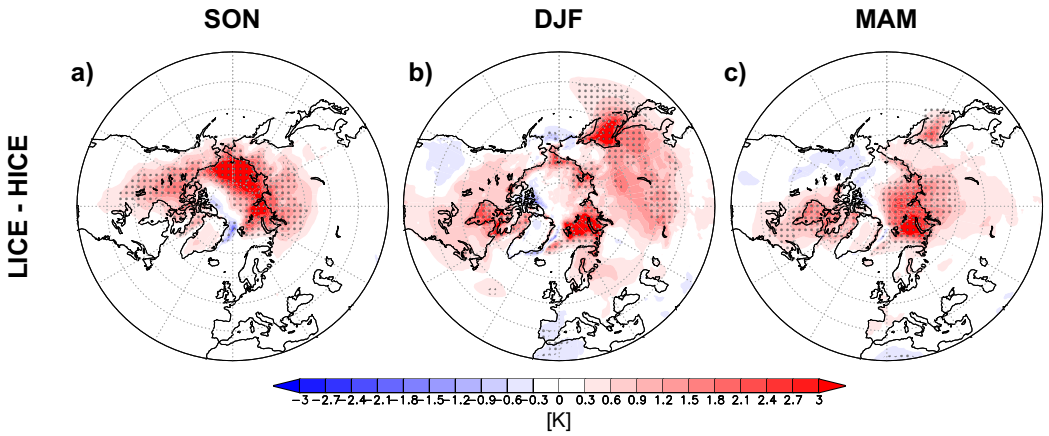

Fig. 4.39.: LICE-HICE differences in the seasonal mean 2 m temperature for autumn, winter and spring. Stippling indicates statistical significance at the 95% level according to a two-sided Wilcoxon-test.

circulation model For the Earth Simulator). Furthermore, Romanowsky et al. (2019) used a the same approach with ECHAM6 (Stevens et al., 2013) and ECHAM6 coupled with the fast interactive ozone chemistry scheme SWIFT (Wohltmann et al., 2017). By adding an additional model to this set of models, the controversy about the model dependence of the reaction to AA is further addressed. Each experiment includes 38 single simulation runs with transient SST forcing from 1979/80 to 2016/17. As prior ICON simulations, each run is initialised with ERA-Interim data on the 1st of September and run for nine months. CMIP6 boundary data is used to create the transient SST and constant sea ice data. The LICE and HICE experiment apply the default setup for the gravity wave drag, as it is used in ICON_{ctl}.

Figure 4.38 depicts the seasonal sea ice loss pattern derived from deducting the HICE (1979-1983) from the LICE (2005-2009) sea ice concentration. It is compared to the sea ice loss pattern derived from deducting the early (2000-2017) from the late (1979-2000) period in ERA-Interim. The comparison of the difference patterns demonstrates, that the difference between the two 5-year averages match the differences between the late and the early period. This accounts for all seasons. As described in Section 4.4, largest sea ice loss in the recent decades has been observed in autumn, where is stretches from the Barents Sea all the way along the Russian Arctic up to the Beaufort Sea. In winter and spring sea ice loss is more regionally confined to the Barents Sea. How this sea ice loss affects the atmospheric circulation in ICON will be discussed in the following.

Figure 4.39 shows the sea ice induced seasonal 2 m temperature differences on a polar stereographic projection. The heating in autumn is confined to the high latitudes. Largest significant temperature increases, with up to 5 K in the Chukchi Sea, are visible in the LICE experiment in the region with strongly reduced sea ice (cf. Fig. 4.38 a). Further significant positive temperature differences are visible in northern North America and Siberia. The small-scale cooling patterns in the northern Greenland Sea are caused by sea ice increase

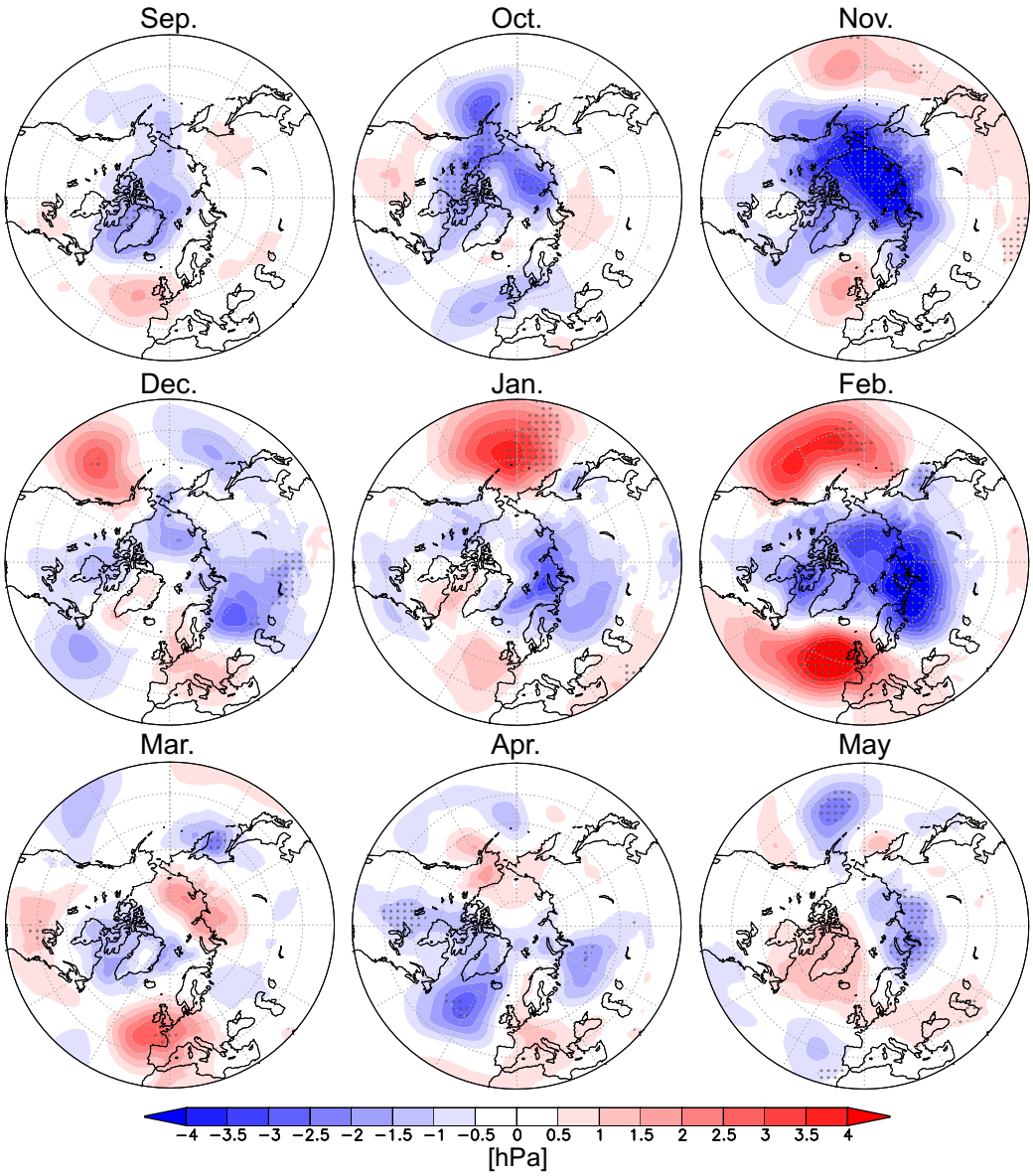

Fig. 4.40.: LICE-HICE differences in the monthly mean MSLP for the months September to May. Stippling indicates statistical significance at the 95% level according to a two-sided Wilcoxon-test.

in the LICE experiment. Dynamically induced temperature differences spread to the mid-latitudes in winter. However, largest differences are still confined to the areas with sea ice loss with up to 9 K in the Barents Sea and up to 4.5 K in the Sea of Okhotsk.In contrast to the ERA-Interim differences between the late and the early period, Asia exhibits significant warming in the LICE experiment (cf. Fig. 4.33 b). The sea ice loss in ICON does not reproduce the "warm Arctic-cold continents" pattern on the Asian side. However, the sea ice differences in ICON produce some continental cooling over the western United States, the Iberian Peninsula and North Africa. In spring, the differences between the two sea ice experiments are weakened and mostly confined to the regions of sea ice loss. The maximum difference is again observed in the Barents Sea with up to 6 K. Although not significant, the negative temperature signal stretching from Alaska into western Canada in autumn is reproduced by the reanalysis and the different ICON experiments (cf. Fig. 4.33 c, f and i).

The monthly mean sea ice induced MSLP differences are depicted in Figure 4.40. In the autumn months significant differences are mainly limited to the Arctic. Sea ice loss induces a significant negative MSLP reduction in the high latitudes in autumn. The resulting difference pattern resembles the positive phase of the AO. The impact of sea ice loss in December is small and significant differences are only visible in the eastern Pacific (positive) and in central Asia (negative). These results disagree with the significant positive MSLP difference over Siberia in the late period in ERA-Interim (cf. Fig. 4.35 a and b). In January and February, ICON reacts to the sea ice reduction with a MSLP pattern strongly resembling the positive phase of the AO. This is particularly pronounced in February. Whereas the pressure increase in the Pacific MSLP is also visible in the late ERA-Interim period, the sea ice induced

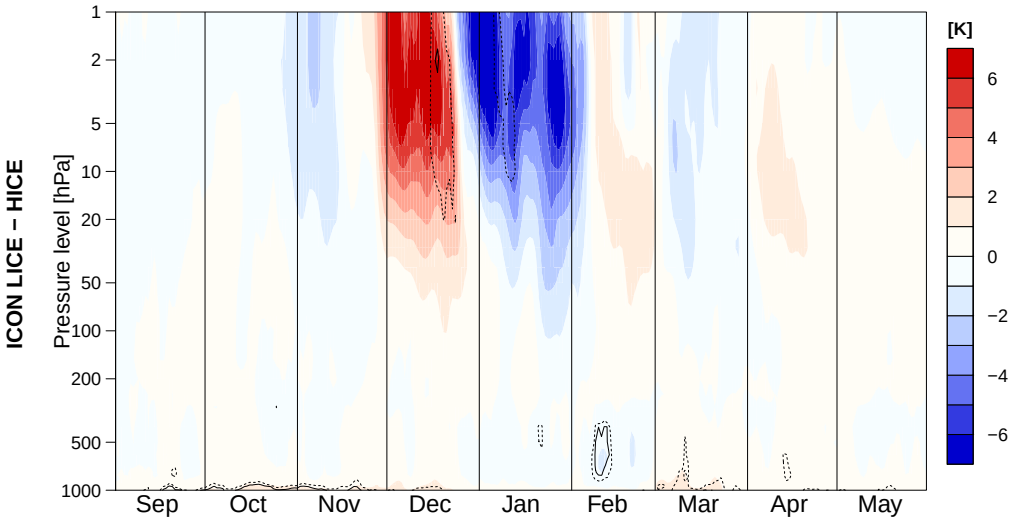

Fig. 4.41.: Time-height cross section of climatological mean temperature differences of the LICE and HICE experiment for the polar cap mean (65.25° N to 90° N). Differences for ERA-Interim (a), ICON$_{ctl}$ (b) and ICON$_{gwd-}$ (c). Dashed/solid lines indicate statistical significance at the 95/99% level according to a two-sided Wilcoxon-test.

NAO pattern strongly disagrees with ERA-Interim. Also the weak difference patterns in spring do not match the ERA-Interim differences between the late and the early period.

To further investigate how stratospheric processes are influenced by the sea ice loss and how they affect the described MSLP differences, Figure 4.41 illustrates the polar cap mean temperature differences between the LICE and HICE simulation. The stratosphere exhibits significant difference patterns in winter only. It is characterised by a significant warming in December and significant cooling in January. Compared to ERA-Interim the signal is approximately 1-2 months phase shifted. As there is no significant stratospheric difference in February, this can explain why the negative NAO reaction is not triggered in the MSLP pattern.

Overall the sea ice induced patterns do not agree very well with the ERA-Interim differences between the late and the early period. Further experiments with ICON showed that small changes in the described setup do not lead to significant improvements. However, a LICE/HICE setup with the improved gravity wave drag parameterisation is planned for the near future. Further experiments with improved ICON setups will help to further distinguish between deficits of the atmospheric model and internal variability of ERA-Interim. A further interpretation of these results is provided in Section 5.

5 Discussion and outlook

Seasonal prediction is a field with large potential influence in different socioeconomic sectors (Vitart et al., 2012), such as agriculture (Ogallo et al., 2000), health (Tompkins et al., 2019) or energy (Clark et al., 2017). The skill of seasonal prediction is largely based on the existence of slow, and predictable, variations in the Earth's boundary conditions of soil moisture, snow cover, sea-ice and sea surface temperatures (SSTs) (cf. Section 1.1). In recent years, the stratosphere also gained increasing attention by the seasonal prediction community (e.g. Domeisen et al., 2020). In particular in Europe, where the skill of seasonal prediction is low, the stratosphere is seen as an important predictor, that could help to increase this skill (Domeisen et al., 2015).

This thesis demonstrated that the stratosphere can play an important role for the future of seasonal predictions for mid-latitudes, as it links slow tropical and Arctic processes, i.e. El Niño-Southern Oscillation (ENSO), quasi-biennial oscillation (QBO) and sea ice variability, to mid-latitude weather patterns. These slow processes exhibit higher predictability than the more chaotic internal variability of synoptic weather patterns in mid-latitudes and therefore could constitute an increased skill in mid-latitude seasonal prediction. A realistic representation of stratospheric dynamics and variability plays a key role for these linkages. On these grounds, the stratospheric circulation as well as the described key processes were investigated with the new ICOsahedral Non-hydrostatic atmosphere model ICON in this thesis. A set of seasonal experiments with ICON in numerical weather prediction (NWP) configuration formed the basis of a thorough analysis of stratospheric processes and gravity wave drag based improvements. The introduction raised four research questions (RQs, cf. Section 1.3). These RQs will now be addressed with the help of the insights from the four sections of Chapter 4. Additionally, further steps towards more reliable seasonal ICON predictions for mid-latitudes will be discussed.

RQ1 Is ICON able to simulate the stratospheric vortex realistically?

This research question is assessed in Section 4.1 by evaluating the seasonal climatology of the control simulation ICON_{ctl}. As ICON-NWP is an atmosphere only model, sea ice content and SSTs are prescribed using CMIP6 data. A sensitivity experiment with ERA-Interim data revealed that the simulation of the stratospheric polar vortex is not sensitive to small changes in the boundary forcing in ICON. Although the basic evolution and variability of the stratospheric vortex is reproduced, ICON underestimates the strength of the vortex in winter. The significant weakening of westerlies is accompanied by strong warming of the polar stratosphere and a strongly overestimated MSW frequency. Largest biases to ERA-Interim are visible in January, when also

the amount of MSWs is largely overestimated. These results are in agreement with Crueger et al. (2018), who found out that stratospheric westerlies are underestimated in the climate configuration of ICON. Furthermore, the findings correspond to the results from Borchert et al. (2019): They state that stratospheric winter westerlies are too weak, even when using an upper-atmosphere extension of ICON. Thus, this study eliminates the model top at 75 km as a potential cause for the stratospheric biases. The stratospheric biases in ICON are connected to tropospheric pressure biases, that strongly resemble the negative phase of the Arctic Oscillation (AO), with positive MSLP bias in the Arctic, and negative pressure bias in the mid and lower latitudes. These pressure patterns are linked to weak and southward shifted polar jet stream. Crueger et al. (2018) found similar MSLP bias patterns in the climate configuration ICON-A.

As ICON is a newly developed atmosphere model, it is constantly being developed and improved. Whereas this thesis is based on ICON-NWP version 2.1.0, the latest DWD release is the version 2.6.0. Although no major changes in the new version concern the stratosphere, it is important to also test the stratospheric behaviour of the new model versions in future. A Git based version control system for the ICON-NWP releases could help to increase usage and testing of newly released ICON versions, by enabling easy and quick access to the newest model versions for licensees.

RQ2 What is the influence of the gravity wave drag parameterisations in ICON?

Small-scale gravity waves are not resolved in ICON and are therefore parameterised. They play an important role for the stratosphere, as their amplitude will grow as the inverse square of the density until they break. They can strongly influence the mean flow by depositing stored momentum and energy from the troposphere. Furthermore they have been proven to strongly interact with resolved waves during major stratospheric warmings (MSWs). However, the gravity wave parameterisations have not been tested in a seasonal setup and are resolution dependent. Section 4.2 demonstrates, how the orographic and non-orographic drag parameterisations influence the stratospheric circulation, in particular in winter. By reducing the drag, which the gravity waves exert on the mean flow, the westerly circulation can be strengthened.

As the control experiment with ICON underestimates the strength of the stratospheric polar vortex in winter, this thesis discussed three sensitivity experiments with reduced gravity wave drag: an experiment with a 20% reduced non-orographic gravity wave drag (ICON$_{nogwd-}$), one with a 20% reduced orographic gravity wave drag and further adjusted sub-grid scale orography (SSO) scheme (ICON$_{sso-}$) and a third experiment that combines the former two adjusted parameterisations to an overall reduced gravity wave drag (ICON$_{gwd-}$). Both gravity wave drag reductions lead to a significant stratospheric bias reduction, which is caused by a strengthening of the stratospheric westerlies. The effect of the non-orographic drag is stronger than the orographic effect. Strongest strengthening of stratospheric westerlies is present in the simulation

combining both parameterisations. The gravity wave drag reductions do not lead to a reduction of the total MSW frequency, however, the monthly distribution of MSWs is more realistic, compared to ERA-Interim. Whereas the adjusted SSO scheme has a strong and significant positive effect on MSLP bias patterns in all months, the reduced non-orographic drag affects the MSLP patterns only via stratosphere-troposphere coupling. Hence, in ICON$_{nogwd-}$ MSLP bias reductions are small and mainly limited to January, where largest stratospheric improvements are present. Furthermore, ICON is able to reproduce realistic patterns of stratosphere-troposphere coupling for weak and strong stratospheric and tropospheric NAM events. A reduction of gravity wave drag leads to intensified stratosphere-troposphere coupling. This especially accounts for a reduction of the non-orographic drag, which is in accordance with the results from Polichtchouk et al. (2018a). The strong and weak NAM composites further demonstrate, that stratosphere and troposphere in ICON and ERA-Interim are strongly coupled during these events. Anomalous stratospheric vortex events are of interest for seasonal predictions, as the troposphere is significantly influenced up to 60 days after the onset of the event. It is furthermore shown, that strong surface NAM anomalies are preceded by stratospheric NAM anomalies by up to 50 days. Taking into account the stratospheric and tropospheric bias reductions as well as the effects on stratosphere-troposphere coupling, the combined experiment ICON$_{gwd-}$ delivers the best results and is suggested as the current optimal setup for seasonal simulations with ICON-NWP in R2B5 resolution. Bearing in mind, that the gravity wave drag is resolution dependent and potentially needs to be adjusted for differing resolutions.

In a further not presented experiment the non-orographic gravity wave drag was reduced by 60%. This strong reduction did not lead to further bias reductions, but larger biases in the upper stratosphere. A strong reduction of the non-orographic gravity wave drag is therefore not recommended. However, this was not tested for the SSO scheme, where a further reduction of the low level wake drag constant and the gravity wave drag constant as well a further increase of the critical Froude number could result in additional bias reductions. The focus of this thesis is on the stratospheric circulation of the Northern Hemisphere, as there is potential for improved seasonal predictions based on an accurate simulation of the highly variable northern polar vortex. Nevertheless, the influence of the gravity wave drag on the circulation of the Southern Hemisphere is of interest for future studies.

RQ3 How do tropical phenomena influence the stratospheric vortex?

Tropical oscillations, such as QBO and ENSO, with high potential predictability on seasonal time scales, can have significant influence on the strength of the stratospheric polar vortex in winter. Therefore, they are able to have an effect on the phase of the NAM and hence mid-latitude weather patterns. Section 4.3 investigates these mechanisms and how they are simulated by ICON.

The quasi-oscillatory behaviour of the QBO is not simulated by ICON. Independent of the QBO phase during initialisation in September, the equatorial stratospheric

zonal wind shifts towards weak easterlies with an approximate strength of 10 m/s. A comparison to the ERA-Interim QBO-E anomalies revealed, that ICON zonal mean zonal wind biases closely resemble these QBO-E anomalies. This accounts in particular for the months January to March, when all single ICON runs are in weak QBO-E phase. This QBO-E phase is connected to a weaker stratospheric polar vortex via the Holton-Tan mechanism (Holton and Tan, 1980). The absent QBO in ICON is therefore identified as a further mechanism causing the weak stratospheric vortex. This could be tested by nudging the tropical stratosphere towards a realistic QBO behaviour. However, at the time of performing this study, this kind of nudging was not implemented in ICON-NWP. For the future of seasonal predictions with ICON, a realistic simulation of the QBO is necessary. The reduced gravity wave drag has no direct effect on the QBO.

The quasi-oscillatory behaviour of ENSO in ICON is prescribed by the boundary SST data. Therefore, in Section 4.3.2 the focus lies on the high-latitudinal reaction of the stratosphere and the troposphere to the extreme phases of ENSO. In late winter, the warm ENSO (wENSO) events are connected to a significant downward propagating signal of warm anomalies in the stratosphere in the ICON experiments and ERA-Interim. This anomaly is connected to a weakening of the stratospheric vortex and is in accordance with literature (e.g. Van Loon and Labitzke, 1987; Manzini et al., 2006). The stratospheric cooling as response to the cold ENSO (cENSO) phase is less pronounced and significant in ICON and ERA-Interim. The ICON experiments exhibit significant polar cooling in the lower stratosphere and the troposphere in late winter and early spring, features that are only partly visible in winter in ERA-Interim. These cold anomalies in the troposphere are connected to a pattern strongly resembling the positive phase of the AO, with significant negative MSLP anomalies in the Arctic and positive anomalies in mid-latitudes. The described strong AO pattern in the cENSO composite is present ERA-Interim, but is more pronounced in the ICON simulations. The wENSO composite, on the other hand, exhibits a MSLP anomaly pattern resembling the negative phase of the AO, which is strongest and most significant in February in the reanalysis and in both ICON simulations. The ICON simulations in particular, suggest a significant effect of wENSO (negative NAO) and cENSO (positive NAO) on European weather in late winter. These results are in accordance with Brönnimann (2007). The stratospheric pathway seems to play a greater role for the wENSO anomalies in reanalysis and ICON. Furthermore, the North Pacific centre of action of the PNA plays a major role in connecting ENSO anomalies to anomalies in the AO. Overall, the agreement on the effects of ENSO between ERA-Interim and the two ICON simulations is large, suggesting a realistic representation of ENSO teleconnections in ICON. The effect of the different ENSO phases is not altered by the adjusted gravity wave drag parameterisations. Additional process based studies of these teleconnection mechanisms could help to further understand linkages between ENSO and mid-latitude weather patterns.

RQ4 Does ICON show a stratospheric pathway for Arctic-midlatitude linkages?

If and how the rapidly warming Arctic affects weather in mid-latitudes is still being widely discussed by the community (e.g Vihma, 2014; Cohen et al., 2020). Vavrus (2018) outlines this discussion by stating that Arctic amplification (AA) may affect weather in mid-latitudes, but controversies remain as to mechanisms and robustness. The large divergence in model consensus when testing whether and/or how AA affects mid-latitude circulation, has amplified this discussion (Cohen et al., 2020). However, the recent focus on the topic of Arctic-midlatitude linkages led to a much richer understanding of the involved mechanism. The stratosphere has been identified as a conduit between surface-based forcing of planetary waves in the Arctic and tropospheric circulation changes in mid latitudes. By absorbing upward-propagating planetary wave energy, the stratospheric polar vortex is weakened and has been found to steer the AO towards its negative phase in late winter, thus, highlighting the important role of stratosphere-troposphere coupling. Seasonal simulations with ICON, including a transient control experiment, a tuned transient experiment with reduced gravity wave drag as well as a sea ice sensitivity experiment, exhibit the opposite signal with difference pattern resembling the positive phase of the AO in late winter. This accounts for the late minus early approach, where sea ice, SSTs and volume mixing ratios of greenhouse gases differ, as well as the sea ice experiment with only differing sea ice. All ICON experiments have in common that they do not show the downward propagating signal of the stratospheric pathway, as it is visible in the ERA-Interim difference between the late and the early period. These results can be interpreted in two ways:

1. As ICON, a large number of models do not simulate the mid-latitude tropospheric circulation response to AA (e.g Smith et al., 2019). Therefore, the accompanying negative AO reaction which is connected to the Siberian cooling pattern is absent. Based on a model study with coupled ocean–atmosphere climate models, Blackport et al. (2019) argue that the influence of Arctic climate change, in particular sea ice loss, on the mid-latitude circulation is very weak compared with internal variability of the winter atmosphere. Furthermore, Blackport and Screen (2020) state, that the linkage between AA and mid-latitude atmospheric circulation is likely in the direction from mid-latitudes to the Arctic: Internal variability in mid-latitude circulation, in particular changes between strong or weak zonal flow, may cause anomalous changes in the strength of AA. The increasing length of the observational record, including the continuous AA, may help for separating between causal relationships and internal variability. These causal relationships, however, can be non-linear and intermittent.

2. The divergence between models and observations is a consequence of model deficits, including misrepresentations of stratospheric processes, as there are modelling studies that simulate a weakened polar vortex and cold mid-latitudes as a reaction to AA and sea ice loss, in particular in the Barents–Kara Seas. These studies have a careful experimental design and a well resolved stratosphere in common (e.g. Screen, 2017; Hoshi et al., 2019). Further sea ice only experiments with the improved gravity wave

drag setup of ICON would be a first step to address this topic. Furthermore, the current ICON setup uses a dynamical GEMS (Global and regional Earth-system Monitoring using Satellite and in-situ data) ozone climatology, including simple coupling between the ozone mixing ratio and the thermal tropopause. Romanowsky et al. (2019) showed, that including interactive stratospheric ozone chemistry in atmospheric model calculations leads to an improvement in tropo-stratospheric interactions. As a result of these improved mechanisms a sea ice induced stratospheric pathway was simulated resulting in a negative NAO. Based on this work, a coupling between ICON and the fast but accurate interactive stratospheric ozone chemistry module SWIFT is planned for the near future. Further studies suggest that the remote impacts of Arctic sea-ice loss can only be properly represented using models that simulate interactions among the ocean, sea ice, land and atmosphere (Deser et al., 2015; Deser et al., 2016; Screen et al., 2018). Although more complicated in the setup, including a longer integration time, a coupled atmosphere-ocean approach could help to further improve the representation of the linkages between the Arctic and mid-latitudes.

Final remarks

Seasonal predictions for the extratropics, in particular for Europe, are still at an early stage. They involve Atmospheric general circulation models either forced by predicted SST or are part of a coupled forecast system. The investigated stratospheric processes, including the effects of the gravity wave drag, are only a small part of such a model system. However, this thesis demonstrates, that a large variety of processes on seasonal time scales involve stratospheric pathways. Consequently, a realistic representation of stratospheric processes is an important step towards the long term goal of reliable seasonal predictions in mid-latitudes. The adjusted gravity wave drag parameterisations thereby contribute to a more realistic stratospheric vortex in ICON. As mentioned earlier, further important steps towards this long term goal are a realistic simulation of the QBO as well as including interactive stratospheric ozone chemistry in ICON. Furthermore, many processes in the Arctic climate system are still poorly represented in climate models. The success of the seasonal prediction of ENSO events has proven, that a strong observational network can provide the basis for improved understanding of the governing mechanisms and an increase in the skill of seasonal predictability. The understanding of Arctic climate processes is strongly limited by a lack of observations in the central Arctic, especially in winter and spring. The current MOSAIC (Multidisciplinary drifting Observatory for the Study of Arctic) expedition will close some of these large gaps in the observations and thus enable an improved representation Arctic processes in atmospheric models. These improvements can further contribute to an enhanced understanding of the underlying processes and effects of rapid Arctic climate change.

Bibliography

Alexeev, V. A., I. Esau, I. V. Polyakov, S. J. Byam, and S. Sorokina (2012). "Vertical structure of recent Arctic warming from observed data and reanalysis products". In: *Climatic Change* 111.2, pp. 215–239. DOI: https://doi.org/10.1007/s10584-011-0192-8 (cit. on p. 3).

Anstey, J. A. and T. G. Shepherd (2014). "High-latitude influence of the quasi-biennial oscillation". In: *Quarterly Journal of the Royal Meteorological Society* 140.678, pp. 1–21. DOI: https://doi.org/10.1002/qj.2132 (cit. on p. 5).

Baldwin, M. P. and T. J. Dunkerton (1999). "Propagation of the Arctic Oscillation from the stratosphere to the troposphere". In: *Journal of Geophysical Research: Atmospheres* 104.D24, pp. 30937–30946. DOI: https://doi.org/10.1029/1999JD900445 (cit. on p. 2).

– (2001). "Stratospheric harbingers of anomalous weather regimes". In: *Science* 294.5542, pp. 581–584. DOI: https://doi.org/10.1126/science.1063315 (cit. on pp. 2, 19, 23, 33, 56, 58, 60, 86).

Baldwin, M. P., L. J. Gray, T. J. Dunkerton, K. Hamilton, P. H. Haynes, et al. (2001). "The quasi-biennial oscillation". In: *Reviews of Geophysics* 39.2, pp. 179–229. DOI: https://doi.org/10.1029/1999RG000073 (cit. on pp. 20, 70).

Baldwin, M. P. and D. W. J. Thompson (2009). "A critical comparison of stratosphere–troposphere coupling indices". In: *Quarterly Journal of the Royal Meteorological Society: A journal of the atmospheric sciences, applied meteorology and physical oceanography* 135.644, pp. 1661–1672. DOI: https://doi.org/10.1002/qj.479 (cit. on pp. 21, 33, 34, 56).

Barnston, A. G., M. K. Tippett, M. L. L'Heureux, S. Li, and D. G. DeWitt (2012). "Skill of real-time seasonal ENSO model predictions during 2002–11: Is our capability increasing?" In: *Bulletin of the American Meteorological Society* 93.5, pp. 631–651. DOI: https://doi.org/10.1175/BAMS-D-11-00111.1 (cit. on p. 23).

Bauer, D. F. (1972). "Constructing confidence sets using rank statistics". In: *Journal of the American Statistical Association* 67.339, pp. 687–690 (cit. on p. 36).

Bauer, P., A. Thorpe, and G. Brunet (2015). "The quiet revolution of numerical weather prediction". In: *Nature* 525.7567, pp. 47–55. DOI: https://doi.org/10.1038/nature14956 (cit. on p. 1).

Bjerknes, V. (1904). "Das Problem der Wettervorhersage, betrachtet vom Standpunkte der Mechanik und der Physik". In: *Meteor. Z.* 21, pp. 1–7 (cit. on p. 1).

Blackport, R. and J. A. Screen (2020). "Insignificant effect of Arctic amplification on the amplitude of midlatitude atmospheric waves". In: *Science advances* 6.8, eaay2880. DOI: https://doi.org/10.1126/sciadv.aay2880 (cit. on p. 97).

Blackport, R., J. A. Screen, K. van der Wiel, and R. Bintanja (2019). "Minimal influence of reduced Arctic sea ice on coincident cold winters in mid-latitudes". In: *Nature Climate Change* 9.9, pp. 697–704. DOI: https://doi.org/10.1038/s41558-019-0551-4 (cit. on pp. 24, 97).

Boer, GJ and K Hamilton (2008). "QBO influence on extratropical predictive skill". In: *Climate dynamics* 31.7-8, pp. 987–1000. DOI: https://doi.org/10.1007/s00382-008-0379-5 (cit. on p. 5).

Bonaventura, L. (2004). "The ICON project: Development of a unified model using triangular geodesic grid". In: *Proceedings of the ECMWF Annual Seminar on Developments in Numerical Methods for Atmospheric and Ocean Modelling, ECMWF, Reading* (cit. on p. 3).

Borchert, S., G. Zhou, M. Baldauf, H. Schmidt, G. Zängl, and D. Reinert (2019). "The upper-atmosphere extension of the ICON general circulation model (version: ua-icon-1.0)". In: *Geoscientific Model Development* 12, pp. 3541–3569. DOI: https://doi.org/10.5194/gmd-12-3541-2019 (cit. on pp. 3, 47, 94).

Brands, S. (2017). "Which ENSO teleconnections are robust to internal atmospheric variability?" In: *Geophysical Research Letters* 44.3, pp. 1483–1493. DOI: https://doi.org/10.1002/2016GL071529 (cit. on pp. 2, 23).

Brewer, A. W. (1949). "Evidence for a world circulation provided by the measurements of helium and water vapour distribution in the stratosphere". In: *Quarterly Journal of the Royal Meteorological Society* 75.326, pp. 351–363. DOI: https://doi.org/10.1002/qj.49707532603 (cit. on p. 16).

Brönnimann, S. (2007). "Impact of El Niño–southern oscillation on European climate". In: *Reviews of Geophysics* 45.3. DOI: https://doi.org/10.1029/2006RG000199 (cit. on pp. 5, 23, 78, 96).

Butchart, N., A. J. Charlton-Perez, I. Cionni, S. C. Hardiman, P. H. Haynes, et al. (2011). "Multimodel climate and variability of the stratosphere". In: *Journal of Geophysical Research: Atmospheres* 116.D5. DOI: https://doi.org/10.1029/2010JD014995 (cit. on p. 4).

Butler, A. H., A. J. Charlton-Perez, D. I. V. Domeisen, C. I. Garfinkel, E. P. Gerber, et al. (2019). "Sub-seasonal Predictability and the Stratosphere". In: *Sub-Seasonal to Seasonal Prediction*. Elsevier, pp. 223–241. DOI: https://doi.org/10.1016/B978-0-12-811714-9.00011-5 (cit. on p. 2).

Butler, A. H., J. P. Sjoberg, D. J. Seidel, and K. H. Rosenlof (2017). *A sudden stratospheric warming compendium*. DOI: https://doi.org/doi:10.5194/essd-9-63-2017 (cit. on p. 19).

Camp, C. D. and K.-K. Tung (2007). "Stratospheric polar warming by ENSO in winter: A statistical study". In: *Geophysical Research Letters* 34.4. DOI: https://doi.org/10.1029/2006GL028521 (cit. on pp. 2, 5, 67).

Charlton-Perez, A. J., M. P. Baldwin, T. Birner, R. X. Black, A. H. Butler, et al. (2013). "On the lack of stratospheric dynamical variability in low-top versions of the CMIP5 models". In: *Journal of Geophysical Research: Atmospheres* 118.6, pp. 2494–2505. DOI: https://doi.org/10.1002/jgrd.50125 (cit. on p. 4).

Charlton, A. J. and L. M. Polvani (2007). "A new look at stratospheric sudden warmings. Part I: Climatology and modeling benchmarks". In: *Journal of Climate* 20.3, pp. 449–469. DOI: https://doi.org/10.1175/JCLI3996.1 (cit. on p. 47).

Charney, J. G. and P. G. Drazin (1961). "Propagation of planetary scale waves from the lower atmosphere to the upper atmosphere". In: *J Geophys Res* 66, pp. 83–109. DOI: https://doi.org/10.1029/JZ066i001p00083 (cit. on p. 18).

Clark, R. T., P. E. Bett, H. E. Thornton, and A. A. Scaife (2017). "Skilful seasonal predictions for the European energy industry". In: *Environmental Research Letters* 12.2, p. 024002. DOI: https://doi.org/10.1088/1748-9326/aa94a7 (cit. on p. 93).

Cohen, J., J. C Furtado, M. A. Barlow, V. A. Alexeev, and J. E. Cherry (2012). "Arctic warming, increasing snow cover and widespread boreal winter cooling". In: *Environmental Research Letters* 7.1, p. 014007. DOI: http://dx.doi.org/10.1088/1748-9326/7/1/014007 (cit. on p. 82).

Cohen, J. and J. Jones (2011). "Tropospheric precursors and stratospheric warmings". In: *Journal of climate* 24.24, pp. 6562–6572. DOI: https://doi.org/10.1175/2011JCLI4160.1 (cit. on p. 47).

Cohen, J., J. A. Screen, J. C. Furtado, M. Barlow, D. Whittleston, et al. (2014). "Recent Arctic amplification and extreme mid-latitude weather". In: *Nature geoscience* 7.9, pp. 627–637. DOI: https://doi.org/10.1038/ngeo2234 (cit. on pp. 3, 23, 24, 81).

Cohen, J., X. Zhang, J. A. Francis, T. Jung, R. Kwok, et al. (2020). "Divergent consensuses on Arctic amplification influence on midlatitude severe winter weather". In: *Nature Climate Change*, pp. 1–10. DOI: https://doi.org/10.1038/s41558-019-0662-y (cit. on pp. 3, 5, 24, 81, 97).

Cohen, J, M. Barlow, P. J. Kushner, and K. Saito (2007). "Stratosphere–troposphere coupling and links with Eurasian land surface variability". In: *Journal of Climate* 20.21, pp. 5335–5343. DOI: https://doi.org/10.1175/2007JCLI1725.1 (cit. on p. 24).

Colucci, Stephen J and Thomas S Ehrmann (2018). "Synoptic–dynamic climatology of the Aleutian high". In: *Journal of the Atmospheric Sciences* 75.4, pp. 1271–1283. DOI: https://doi.org/10.1175/JAS-D-17-0215.1 (cit. on p. 16).

Cowtan, K and R. G. Way (2014). "Coverage bias in the HadCRUT4 temperature series and its impact on recent temperature trends". In: *Quarterly Journal of the Royal Meteorological Society* 140.683, pp. 1935–1944. DOI: https://doi.org/10.1002/qj.2297 (cit. on p. 3).

Crasemann, B., D. Handorf, R. Jaiser, K. Dethloff, T. Nakamura, J. Ukita, and K. Yamazaki (2017). "Can preferred atmospheric circulation patterns over the North-Atlantic-Eurasian region be associated with arctic sea ice loss?" In: *Polar Science* 14, pp. 9–20. DOI: https://doi.org/10.1016/j.polar.2017.09.002 (cit. on pp. 24, 83, 84).

Crueger, T., M. A. Giorgetta, R. Brokopf, M. Esch, S. Fiedler, et al. (2018). "ICON-A, The Atmosphere Component of the ICON Earth System Model: II. Model Evaluation". In: *Journal of Advances in Modeling Earth Systems* 10.7, pp. 1638–1662. DOI: https://doi.org/10.1029/2017MS001233 (cit. on pp. 3, 94).

Dahlke, S. and M. Maturilli (2017). "Contribution of atmospheric advection to the amplified winter warming in the Arctic North Atlantic region". In: *Advances in Meteorology* 2017. DOI: https://doi.org/10.1155/2017/4928620 (cit. on p. 81).

Day, J. J., E. Hawkins, and S. Tietsche (2014). "Will Arctic sea ice thickness initialization improve seasonal forecast skill?" In: *Geophysical Research Letters* 41.21, pp. 7566–7575. DOI: https://doi.org/10.1002/2014GL061694 (cit. on p. 80).

Dee, D. P., S. M. Uppala, A. J. Simmons, P. Berrisford, P. Poli, et al. (2011). "The ERA-Interim reanalysis: Configuration and performance of the data assimilation system". In: *Quarterly Journal of the royal meteorological society* 137.656, pp. 553–597. DOI: https://doi.org/10.1002/qj.828 (cit. on p. 32).

Deser, C., L. Sun, R. A. Tomas, and J. Screen (2016). "Does ocean coupling matter for the northern extratropical response to projected Arctic sea ice loss?" In: *Geophysical Research Letters* 43.5, pp. 2149–2157. DOI: https://doi.org/10.1002/2016GL067792 (cit. on p. 98).

Deser, C., R. A. Tomas, and L. Sun (2015). "The role of ocean–atmosphere coupling in the zonal-mean atmospheric response to Arctic sea ice loss". In: *Journal of Climate* 28.6, pp. 2168–2186. DOI: https://doi.org/10.1175/JCLI-D-14-00325.1 (cit. on p. 98).

Dethloff, K., D. Handorf, R. Jaiser, A. Rinke, and P. Klinghammer (2019). "Dynamical mechanisms of Arctic amplification". In: *Annals of the New York Academy of Sciences* 1436.1, pp. 184–194. DOI: https://doi.org/10.1111/nyas.13698 (cit. on p. 23).

Doblas-Reyes, F. J. (2010). "Seasonal prediction over Europe". In: *Proceedings of the ECMWF Seminar on Predictability in the European and Atlantic regions*. Vol. 6 (cit. on p. 2).

Doblas-Reyes, F. J., J. García-Serrano, F. Lienert, A. P. Biescas, and L. R. L. Rodrigues (2013). "Seasonal climate predictability and forecasting: status and prospects". In: *Wiley Interdisciplinary Reviews: Climate Change* 4.4, pp. 245–268. DOI: https://doi.org/10.1002/wcc.217 (cit. on p. 1).

Dobson, G. M. B. (1956). "Origin and distribution of the polyatomic molecules in the atmosphere". In: *Proceedings of the Royal Society of London. Series A. Mathematical and Physical Sciences* 236.1205, pp. 187–193. DOI: https://doi.org/10.1098/rspa.1956.0127 (cit. on p. 16).

Domeisen, D. I. V., A. H. Butler, A. J. Charlton-Perez, B. Ayarzagüena, M. P. Baldwin, et al. (2020). "The role of the stratosphere in subseasonal to seasonal prediction: 2. Predictability arising from stratosphere-troposphere coupling". In: *Journal of Geophysical Research: Atmospheres* 125.2, e2019JD030923. DOI: https://doi.org/10.1029/2019JD030923 (cit. on pp. 4, 93).

Domeisen, D. I. V., A. H. Butler, K. Fröhlich, M. Bittner, W. A Müller, and J. Baehr (2015). "Seasonal predictability over Europe arising from El Niño and stratospheric variability in the MPI-ESM seasonal prediction system". In: *Journal of Climate* 28.1, pp. 256–271. DOI: https://doi.org/10.1175/JCLI-D-14-00207.1 (cit. on pp. 2, 93).

Dunkerton, T. J. (1990). "Annual variation of deseasonalized mean flow acceleration in the equatorial lower stratosphere". In: *Journal of the Meteorological Society of Japan. Ser. II* 68.4, pp. 499–508. DOI: https://doi.org/10.2151/jmsj1965.68.4_499 (cit. on p. 70).

Durack, P. J. and K. E. Taylor (2018). *PCMDI AMIP SST and sea-ice boundary conditions version 1.1.4*. DOI: 10.22033/ESGF/input4MIPs.2204 (cit. on p. 31).

Enfield, D. B. and A. M. Mestas-Nuñez (1999). "Multiscale variabilities in global sea surface temperatures and their relationships with tropospheric climate patterns". In: *Journal of Climate* 12.9, pp. 2719–2733. DOI: https://doi.org/10.1175/1520-0442(1999)012<2719:MVIGSS>2.0.CO;2 (cit. on p. 2).

Etling, D. (2008). *Theoretische Meteorologie: Eine Einführung*. Springer-Verlag (cit. on pp. 12, 18).

Fetterer, F., K. Knowles, W. N. Meier, M. Savoie, and A. K. Windnagel (2017). *Sea Ice Index, Version 3. updated daily [accessed: July 2020]*. DOI: https://doi.org/10.7265/N5K072F8 (cit. on p. 79).

Francis, J. A. (2017). "Why are Arctic linkages to extreme weather still up in the air?" In: *Bulletin of the American Meteorological Society* 98.12, pp. 2551–2557. DOI: https://doi.org/10.1175/BAMS-D-17-0006.1 (cit. on p. 5).

Francis, J. A. and S. J. Vavrus (2012). "Evidence linking Arctic amplification to extreme weather in mid-latitudes". In: *Geophysical research letters* 39.6. DOI: https://doi.org/10.1029/2012GL051000 (cit. on p. 3).

Free, M. and D. J. Seidel (2009). "Observed El Niño–Southern Oscillation temperature signal in the stratosphere". In: *Journal of Geophysical Research: Atmospheres* 114.D23. DOI: https://doi.org/10.1029/2009JD012420 (cit. on pp. 2, 5, 23, 67).

Fritts, D. C. and M. J. Alexander (2003). "Gravity wave dynamics and effects in the middle atmosphere". In: *Reviews of geophysics* 41.1. DOI: https://doi.org/10.1029/2001RG000106 (cit. on p. 4).

Garfinkel, C. I. and D. L. Hartmann (2008). "Different ENSO teleconnections and their effects on the stratospheric polar vortex". In: *Journal of Geophysical Research: Atmospheres* 113.D18. DOI: https://doi.org/10.1029/2008JD009920 (cit. on p. 75).

– (2007). "Effects of the El Niño–Southern Oscillation and the quasi-biennial oscillation on polar temperatures in the stratosphere". In: *Journal of Geophysical Research: Atmospheres* 112.D19. DOI: https://doi.org/10.1029/2007JD008481 (cit. on pp. 2, 5, 23, 67).

Gassmann, A. and H.-J. Herzog (2008). "Towards a consistent numerical compressible nonhydrostatic model using generalized Hamiltonian tools". In: *Quarterly Journal of the Royal Meteorological Society* 134.635, pp. 1597–1613. DOI: https://doi.org/10.1002/qj.297 (cit. on p. 27).

Giorgetta, M. A., R. Brokopf, T. Crueger, M. Esch, S. Fiedler, et al. (2018). "ICON-A, the Atmosphere Component of the ICON Earth System Model: I. Model Description". In: *Journal of Advances in Modeling Earth Systems* 10.7, pp. 1613–1637. DOI: https://doi.org/10.1029/2017MS001242 (cit. on pp. 3, 25).

Goessling, H. F. and S. Bathiany (2016). "Why CO2 cools the middle atmosphere–a consolidating model perspective". In: *Earth System Dynamics* 7.3, pp. 697–715. DOI: https://doi.org/10.5194/esd-7-697-2016 (cit. on p. 86).

Gray, W. M., J. D. Sheaffer, and J. A. Knaff (1992). "Influence of the stratospheric QBO on ENSO variability". In: *Journal of the Meteorological Society of Japan. Ser. II* 70.5, pp. 975–995. DOI: https://doi.org/10.2151/jmsj1965.70.5_975 (cit. on p. 72).

Hastings, D. A., P. K. Dunbar, G. M. Elphingstone, M. Bootz, H. Murakami, et al. (1999). "The Global Land One-kilometer Base Elevation (GLOBE) Digital Elevation Model". In: *Version* 1.325, pp. 80305–3328 (cit. on p. 30).

Hesselberg, T. (1926). "Die Gesetze der ausgeglichenen atmosphärischen Bewegungen". In: *Beiträge zur Physik der freien Atmosphäre* 12, pp. 141–160 (cit. on p. 27).

Hollander, M., D. A. Wolfe, and E. Chicken (2013). *Nonparametric statistical methods*. Vol. 751. John Wiley & Sons (cit. on p. 36).

Holton, J. R. (2004). *An introduction to dynamic meteorology, fourth edition*. Elsevier (cit. on pp. 12, 14).

– (1983). "The influence of gravity wave breaking on the general circulation of the middle atmosphere". In: *Journal of the Atmospheric Sciences* 40.10, pp. 2497–2507. DOI: https://doi.org/10.1175/1520-0469(1983)040%3C2497:TIOGWB%3E2.0.CO;2 (cit. on p. 19).

Holton, J. R. and H.-C. Tan (1980). "The influence of the equatorial quasi-biennial oscillation on the global circulation at 50 mb". In: *Journal of the Atmospheric Sciences* 37.10, pp. 2200–2208. DOI: https://doi.org/10.1175/1520-0469(1980)037%3C2200:TIOTEQ%3E2.0.CO;2 (cit. on pp. 5, 20, 67, 72, 96).

Honda, M., J. Inoue, and S. Yamane (2009). "Influence of low Arctic sea-ice minima on anomalously cold Eurasian winters". In: *Geophysical Research Letters* 36.8. DOI: https://doi.org/10.1029/2008GL037079 (cit. on pp. 24, 79).

Honda, M. and H. Nakamura (2001). "Interannual seesaw between the Aleutian and Icelandic lows. Part II: Its significance in the interannual variability over the wintertime Northern Hemisphere". In: *Journal of Climate* 14.24, pp. 4512–4529. DOI: https://doi.org/10.1175/1520-0442(2001)014%3C4512:ISBTAA%3E2.0.CO;2 (cit. on p. 22).

Horel, J. D. and J. M. Wallace (1981). "Planetary-scale atmospheric phenomena associated with the Southern Oscillation". In: *Monthly Weather Review* 109.4, pp. 813–829. DOI: https://doi.org/10.1175/1520-0493(1981)109%3C0813:PSAPAW%3E2.0.CO;2 (cit. on p. 22).

Hoshi, K., J. Ukita, M. Honda, T. Nakamura, K. Yamazaki, Y. Miyoshi, and R. Jaiser (2019). "Weak stratospheric polar vortex events modulated by the Arctic sea-ice loss". In: *Journal of Geophysical Research: Atmospheres* 124.2, pp. 858–869. DOI: https://doi.org/10.1029/2018JD029222 (cit. on p. 97).

Ineson, S. and A. A. Scaife (2009). "The role of the stratosphere in the European climate response to El Niño". In: *Nature Geoscience* 2.1, pp. 32–36. DOI: https://doi.org/10.1038/ngeo381 (cit. on pp. 5, 23).

Inoue, J., M. E. Hori, and K. Takaya (2012). "The role of Barents Sea ice in the wintertime cyclone track and emergence of a warm-Arctic cold-Siberian anomaly". In: *Journal of Climate* 25.7, pp. 2561–2568. DOI: https://doi.org/10.1175/JCLI-D-11-00449.1 (cit. on p. 81).

Jaiser, R., K. Dethloff, and D. Handorf (2013). "Stratospheric response to Arctic sea ice retreat and associated planetary wave propagation changes". In: *Tellus A: Dynamic Meteorology and Oceanography* 65.1, p. 19375. DOI: https://doi.org/10.3402/tellusa.v65i0.19375 (cit. on p. 79).

Jaiser, R., K. Dethloff, D. Handorf, A. Rinke, and J. Cohen (2012). "Impact of sea ice cover changes on the Northern Hemisphere atmospheric winter circulation". In: *Tellus A: Dynamic Meteorology and Oceanography* 64.1, p. 11595. DOI: https://doi.org/10.3402/tellusa.v64i0.11595 (cit. on pp. 24, 79).

Jaiser, R., T. Nakamura, D. Handorf, K. Dethloff, J. Ukita, and K. Yamazaki (2016). "Atmospheric winter response to Arctic sea ice changes in reanalysis data and model simulations". In: *Journal of Geophysical Research: Atmospheres* 121.13, pp. 7564–7577. DOI: https://doi.org/10.1002/2015JD024679 (cit. on pp. 3, 24, 84, 86, 88).

Kim, B.-M., S.-W. Son, S.-K. Min, J.-H. Jeong, S.-J. Kim, et al. (2014). "Weakening of the stratospheric polar vortex by Arctic sea-ice loss". In: *Nature communications* 5.1, pp. 1–8. DOI: https://doi.org/10.1038/ncomms5646 (cit. on pp. 3, 24).

Kopp, G. and J. L. Lean (2011). "A new, lower value of total solar irradiance: Evidence and climate significance". In: *Geophysical Research Letters* 38.1. DOI: https://doi.org/10.1029/2010GL045777 (cit. on p. 9).

Kretschmer, M., D. Coumou, J. F. Donges, and J. Runge (2016). "Using causal effect networks to analyze different Arctic drivers of midlatitude winter circulation". In: *Journal of Climate* 29.11, pp. 4069–4081. DOI: https://doi.org/10.1175/JCLI-D-15-0654.1 (cit. on pp. 24, 79).

Krueger, A. J. and R. A. Minzner (1976). "A mid-latitude ozone model for the 1976 US Standard Atmosphere". In: *Journal of Geophysical Research* 81.24, pp. 4477–4481. DOI: https://doi.org/10.1029/JC081i024p04477 (cit. on p. 13).

Labitzke, K. (2013). *Die Stratosphäre: Phänomene, Geschichte, Relevanz*. Springer-Verlag (cit. on p. 19).

– (1981). "Stratospheric-mesospheric midwinter disturbances: A summary of observed characteristics". In: *Journal of Geophysical Research: Oceans* 86.C10, pp. 9665–9678. DOI: https://doi.org/10.1029/JC086iC10p09665 (cit. on p. 34).

– (1987). "Sunspots, the QBO, and the stratospheric temperature in the north polar region". In: *Geophysical Research Letters* 14.5, pp. 535–537. DOI: https://doi.org/10.1029/GL014i005p00535 (cit. on p. 5).

Latif, M., D. Anderson, T. Barnett, M. Cane, R. Kleeman, et al. (1998). "A review of the predictability and prediction of ENSO". In: *Journal of Geophysical Research: Oceans* 103.C7, pp. 14375–14393. DOI: https://doi.org/10.1029/97JC03413 (cit. on p. 2).

Lau, N.-C. (1997). "Interactions between global SST anomalies and the midlatitude atmospheric circulation". In: *Bulletin of the American Meteorological Society* 78.1, pp. 21–34. DOI: https://doi.org/10.1175/1520-0477(1997)078%3C0021:IBGSAA%3E2.0.CO;2 (cit. on p. 75).

Laxon, S. W., K. A. Giles, A. L. Ridout, D. J. Wingham, R. Willatt, et al. (2013). "CryoSat-2 estimates of Arctic sea ice thickness and volume". In: *Geophysical Research Letters* 40.4, pp. 732–737. DOI: https://doi.org/10.1002/grl.50193 (cit. on p. 80).

Lee, S. H., A. J. Charlton-Perez, J. C. Furtado, and S. J. Woolnough (2019). "Abrupt stratospheric vortex weakening associated with North Atlantic anticyclonic wave breaking". In: *Journal of Geophysical Research: Atmospheres* 124.15, pp. 8563–8575. DOI: https://doi.org/10.1029/2019JD030940 (cit. on p. 24).

Leuenberger, D., M. Koller, O. Fuhrer, and C. Schär (2010). "A generalization of the SLEVE vertical coordinate". In: *Monthly weather review* 138.9, pp. 3683–3689. DOI: https://doi.org/10.1175/2010MWR3307.1 (cit. on p. 27).

Limpasuvan, V., J. H. Richter, Y. J. Orsolini, F. Stordal, and O.-K. Kvissel (2012). "The roles of planetary and gravity waves during a major stratospheric sudden warming as characterized in WACCM". In: *Journal of atmospheric and solar-terrestrial physics* 78, pp. 84–98. DOI: https://doi.org/10.1016/j.jastp.2011.03.004 (cit. on p. 19).

Lorenz, E. N. (1975). "Climate Predictability". In: *The Physical Basis of Climate and Climate Modelling: Report of the International Study Conference in Stockholm, 29 July-10 August 1974* 16, pp. 132–136 (cit. on p. 1).

Lott, F. and M. J. Miller (1997). "A new subgrid-scale orographic drag parametrization: Its formulation and testing". In: *Quarterly Journal of the Royal Meteorological Society* 123.537, pp. 101–127. DOI: https://doi.org/10.1002/qj.49712353704 (cit. on p. 29).

Mann, M. E., R. S. Bradley, and M. K. Hughes (2000). *Long-term variability in the El Nino Southern Oscillation and associated teleconnections*. DOI: https://doi.org/10.1017/CBO9780511573125.011 (cit. on p. 2).

Mann, M. E. and J. Park (1994). "Global-scale modes of surface temperature variability on interannual to century timescales". In: *Journal of Geophysical Research: Atmospheres* 99.D12, pp. 25819–25833. DOI: https://doi.org/10.1029/94JD02396 (cit. on p. 2).

Manzini, E. (2009). "ENSO and the stratosphere". In: *Nature Geoscience* 2.11, pp. 749–750. DOI: https://doi.org/10.1038/ngeo677 (cit. on pp. 2, 5, 23, 67).

Manzini, E., M. A. Giorgetta, M. Esch, L. Kornblueh, and E. Roeckner (2006). "The influence of sea surface temperatures on the northern winter stratosphere: Ensemble simulations with the MAECHAM5 model". In: *Journal of climate* 19.16, pp. 3863–3881. DOI: https://doi.org/10.1175/JCLI3826.1 (cit. on pp. 23, 96).

Matsuno, T. (1971). "A dynamical model of the stratospheric sudden warming". In: *Journal of the Atmospheric Sciences* 28.8, pp. 1479–1494. DOI: https://doi.org/10.1175/1520-0469(1971)028%3C1479:ADMOTS%3E2.0.CO;2 (cit. on p. 19).

Meinshausen, M., E. Vogel, A. Nauels, K. Lorbacher, N. Meinshausen, et al. (2017). "Historical greenhouse gas concentrations for climate modelling (CMIP6)". In: *Geoscientific Model Development* 10, pp. 2057–2116. DOI: https://doi.org/10.5194/gmd-10-2057-2017 (cit. on p. 31).

Mironov, D., B. Ritter, J.-P. Schulz, M. Buchhold, M. Lange, and E. MacHulskaya (2012). "Parameterisation of sea and lake ice in numerical weather prediction models of the German Weather Service". In: *Tellus A: Dynamic Meteorology and Oceanography* 64.1, p. 17330. DOI: https://doi.org/10.3402/tellusa.v64i0.17330 (cit. on pp. 29, 80).

Mohanakumar, K. (2008). *Stratosphere troposphere interactions: an introduction*. Springer Science & Business Media (cit. on p. 16).

Mori, M., Y. Kosaka, M. Watanabe, H. Nakamura, and M. Kimoto (2019). "A reconciled estimate of the influence of Arctic sea-ice loss on recent Eurasian cooling". In: *Nature Climate Change* 9.2, pp. 123–129. DOI: https://doi.org/10.1038/s41558-018-0379-3 (cit. on p. 79).

Mori, M., M. Watanabe, H. Shiogama, J. Inoue, and M. Kimoto (2014). "Robust Arctic sea-ice influence on the frequent Eurasian cold winters in past decades". In: *Nature Geoscience* 7.12, pp. 869–873. DOI: https://doi.org/10.1038/ngeo2277 (cit. on pp. 24, 79).

Nakamura, T., K. Yamazaki, K. Iwamoto, M. Honda, Y. Miyoshi, Y. Ogawa, and J. Ukita (2015). "A negative phase shift of the winter AO/NAO due to the recent Arctic sea-ice reduction in late autumn". In: *Journal of Geophysical Research: Atmospheres* 120.8, pp. 3209–3227. DOI: https://doi.org/10.1002/2014JD022848 (cit. on pp. 84, 88).

Nakamura, T., K. Yamazaki, K. Iwamoto, M. Honda, Y. Miyoshi, et al. (2016). "The stratospheric pathway for Arctic impacts on midlatitude climate". In: *Geophysical Research Letters* 43.7, pp. 3494–3501. DOI: https://doi.org/10.1002/2016GL068330 (cit. on pp. 3, 84).

Ogallo, L. A., M. S. Boulahya, and T. Keane (2000). "Applications of seasonal to interannual climate prediction in agricultural planning and operations". In: *Agricultural and Forest Meteorology* 103.1-2, pp. 159–166. DOI: https://doi.org/10.1016/S0168-1923(00)00109-X (cit. on p. 93).

Ogawa, F., N. Keenlyside, Y. Gao, T. Koenigk, S. Yang, et al. (2018). "Evaluating impacts of recent Arctic sea ice loss on the northern hemisphere winter climate change". In: *Geophysical Research Letters* 45.7, pp. 3255–3263. DOI: https://doi.org/10.1002/2017GL076502 (cit. on p. 24).

Orr, A., P. Bechtold, J. Scinocca, M. Ern, and M. Janiskova (2010). "Improved middle atmosphere climate and forecasts in the ECMWF model through a nonorographic gravity wave drag parameterization". In: *Journal of Climate* 23.22, pp. 5905–5926. DOI: https://doi.org/10.1175/2010JCLI3490.1 (cit. on p. 30).

Overland, J. E., K. Dethloff, J. A. Francis, R. J. Hall, E. Hanna, et al. (2016). "Nonlinear response of mid-latitude weather to the changing Arctic". In: *Nature Climate Change* 6.11, pp. 992–999. DOI: https://doi.org/10.1038/nclimate3121 (cit. on p. 3).

Overland, J. E., J. A. Francis, R. Hall, E. Hanna, S.-J. Kim, and T. Vihma (2015). "The melting Arctic and midlatitude weather patterns: Are they connected?" In: *Journal of Climate* 28.20, pp. 7917–7932. DOI: https://doi.org/10.1175/JCLI-D-14-00822.1 (cit. on p. 5).

Overland, J. E., K. R. Wood, and M. Wang (2011). "Warm Arctic—cold continents: climate impacts of the newly open Arctic Sea". In: *Polar Research* 30.1, p. 15787. DOI: https://doi.org/10.3402/polar.v30i0.15787 (cit. on pp. 24, 81).

Palmer, T. N. and D. L. T. Anderson (1994). "The prospects for seasonal forecasting—A review paper". In: *Quarterly Journal of the Royal Meteorological Society* 120.518, pp. 755–793. DOI: https://doi.org/10.1002/qj.49712051802 (cit. on pp. 1, 2).

Palmer, T. N., G. J. Shutts, R. Hagedorn, F. J. Doblas-Reyes, T. Jung, and M. Leutbecher (2005). "Representing model uncertainty in weather and climate prediction". In: *Annu. Rev. Earth Planet. Sci.* 33, pp. 163–193. DOI: https://doi.org/10.1146/annurev.earth.33.092203.122552 (cit. on p. 1).

Pinto, J. G., M. Reyers, and U. Ulbrich (2011). "The variable link between PNA and NAO in observations and in multi-century CGCM simulations". In: *Climate dynamics* 36.1-2, pp. 337–354. DOI: https://doi.org/10.1007/s00382-010-0770-x (cit. on p. 22).

Polichtchouk, I., T. G. Shepherd, and N. J. Byrne (2018a). "Impact of Parametrized Nonorographic Gravity Wave Drag on Stratosphere-Troposphere Coupling in the Northern and Southern Hemispheres". In: *Geophysical Research Letters* 45.16, pp. 8612–8618. DOI: https://doi.org/10.1029/2018GL078981 (cit. on pp. 56, 58, 63, 95).

Polichtchouk, I., T. G. Shepherd, R. J. Hogan, and P. Bechtold (2018b). "Sensitivity of the brewer–Dobson circulation and polar vortex variability to parameterized nonorographic gravity wave drag in a high-resolution atmospheric model". In: *Journal of the Atmospheric Sciences* 75.5, pp. 1525–1543. DOI: https://doi.org/10.1175/JAS-D-17-0304.1 (cit. on pp. 4, 30, 48, 55).

Randel, W. J. (2004). "Wider connections for El Niño". In: *Nature* 431.7011, pp. 920–921. DOI: https://doi.org/10.1038/431920a (cit. on p. 23).

Reinert, D., F. Prill, H. Frank, M. Denhard, and G. Zängl (2018). "Database reference manual for ICON and ICON-EPS". In: *Version* 1.4, p. 35 (cit. on pp. 25, 26).

Rieger, D., M. Bangert, I. Bischoff-Gauss, J. Förstner, K. Lundgren, et al. (2015). "ICON–ART 1.0 – a new online-coupled model system from the global to regional scale". In: *Geoscientific Model Development* 8.6, pp. 1659–1676. DOI: https://doi.org/10.5194/gmd-8-1659-2015 (cit. on p. 25).

Romanowsky, E., D. Handorf, R. Jaiser, I. Wohltmann, W. Dorn, et al. (2019). "The role of stratospheric ozone for Arctic-midlatitude linkages". In: *Scientific reports* 9.1, pp. 1–7. DOI: https://doi.org/10.1038/s41598-019-43823-1 (cit. on pp. 3, 84, 86, 89, 98).

Scinocca, J. F. (2003). "An accurate spectral nonorographic gravity wave drag parameterization for general circulation models". In: *Journal of the atmospheric sciences* 60.4, pp. 667–682. DOI: https://doi.org/10.1175/1520-0469(2003)060<0667:AASNGW>2.0.CO;2 (cit. on p. 30).

Screen, J. A. (2017). "Simulated atmospheric response to regional and pan-Arctic sea ice loss". In: *Journal of Climate* 30.11, pp. 3945–3962. DOI: https://doi.org/10.1175/JCLI-D-16-0197.1 (cit. on p. 97).

Screen, J. A., C. Deser, D. M. Smith, X. Zhang, R. Blackport, et al. (2018). "Consistency and discrepancy in the atmospheric response to Arctic sea-ice loss across climate models". In: *Nature Geoscience* 11.3, pp. 155–163. DOI: https://doi.org/10.1038/s41561-018-0059-y (cit. on pp. 24, 98).

Screen, J. A. and I. Simmonds (2010). "The central role of diminishing sea ice in recent Arctic temperature amplification". In: *Nature* 464.7293, pp. 1334–1337. DOI: https://doi.org/10.1038/nature09051 (cit. on p. 2).

Serreze, M. C., A. P. Barrett, J. C. Stroeve, D. N. Kindig, and M. M. Holland (2009). "The emergence of surface-based Arctic amplification". In: *The Cryosphere* 3.1, p. 11. DOI: https://doi.org/10.5194/tc-3-11-2009 (cit. on p. 3).

Serreze, M. C. and R. G. Barry (2011). "Processes and impacts of Arctic amplification: A research synthesis". In: *Global and planetary change* 77.1-2, pp. 85–96. DOI: https://doi.org/10.1016/j.gloplacha.2011.03.004 (cit. on p. 23).

Seviour, W. J. M., L. J. Gray, and D. M. Mitchell (2016). "Stratospheric polar vortex splits and displacements in the high-top CMIP5 climate models". In: *Journal of Geophysical Research: Atmospheres* 121.4, pp. 1400–1413. DOI: https://doi.org/10.1002/2015JD024178 (cit. on p. 4).

Sigmond, M., J. F. Scinocca, V. V. Kharin, and T. G. Shepherd (2013). "Enhanced seasonal forecast skill following stratospheric sudden warmings". In: *Nature Geoscience* 6.2, p. 98. DOI: https://doi.org/10.1038/ngeo1698 (cit. on p. 47).

Smith, D. M., N. J. Dunstone, A. A. Scaife, E. K. Fiedler, D. Copsey, and S. C. Hardiman (2017). "Atmospheric response to Arctic and Antarctic sea ice: The importance of ocean–atmosphere coupling and the background state". In: *Journal of Climate* 30.12, pp. 4547–4565. DOI: https://doi.org/10.1175/JCLI-D-16-0564.1 (cit. on p. 24).

Smith, D. M., J. A. Screen, C. Deser, J. Cohen, J. C. Fyfe, et al. (2019). "The Polar Amplification Model Intercomparison Project (PAMIP) contribution to CMIP6: Investigating the causes and consequences of polar amplification". In: *Geoscientific Model Development* 12.3, pp. 1139–1164. DOI: https://doi.org/10.5194/gmd-12-1139-2019 (cit. on p. 97).

Song, J., C. Li, W. Zhou, and J. Pan (2009). "The linkage between the Pacific-North American teleconnection pattern and the North Atlantic Oscillation". In: *Advances in Atmospheric Sciences* 26.2, pp. 229–239. DOI: https://doi.org/10.1007/s00376-009-0229-3 (cit. on p. 22).

Stephens, G. L., D. O'Brien, P. J. Webster, P. Pilewski, S. Kato, and J. Li (2015). "The albedo of Earth". In: *Reviews of geophysics* 53.1, pp. 141–163. DOI: https://doi.org/10.1002/2014RG000449 (cit. on p. 9).

Stevens, B., M. Giorgetta, M. Esch, T. Mauritsen, T. Crueger, et al. (2013). "Atmospheric component of the MPI-M Earth system model: ECHAM6". In: *Journal of Advances in Modeling Earth Systems* 5.2, pp. 146–172. DOI: https://doi.org/10.1002/jame.20015 (cit. on p. 89).

Sun, L., J. Perlwitz, and M. Hoerling (2016). "What caused the recent "Warm Arctic, Cold Continents" trend pattern in winter temperatures?" In: *Geophysical Research Letters* 43.10, pp. 5345–5352. DOI: https://doi.org/10.1002/2016GL069024 (cit. on p. 81).

Tang, Y., R.-H. Zhang, T. Liu, W. Duan, D. Yang, et al. (2018). "Progress in ENSO prediction and predictability study". In: *National Science Review* 5.6, pp. 826–839. DOI: https://doi.org/10.1093/nsr/nwy105 (cit. on p. 2).

Taylor, K. E., D. Williamson, and F. Zwiers (2000). *The sea surface temperature and sea-ice concentration boundary conditions for AMIP II simulations*. Program for Climate Model Diagnosis and Intercomparison, Lawrence Livermore National Laboratory, University of California (cit. on p. 31).

Thompson, D. W. J. and J. M. Wallace (1998). "The Arctic Oscillation signature in the wintertime geopotential height and temperature fields". In: *Geophysical research letters* 25.9, pp. 1297–1300. DOI: https://doi.org/10.1029/98GL00950 (cit. on p. 21).

Tompkins, A. M., R. Lowe, H. Nissan, N. Martiny, P. Roucou, M. C. Thomson, and T. Nakazawa (2019). "Predicting climate impacts on health at sub-seasonal to seasonal timescales". In: *Sub-Seasonal to Seasonal Prediction*. Elsevier, pp. 455–477. DOI: https://doi.org/10.1016/B978-0-12-811714-9.00022-X (cit. on p. 93).

Trenberth, K. E. and J. M. Caron (2001). "Estimates of meridional atmosphere and ocean heat transports". In: *Journal of Climate* 14.16, pp. 3433–3443. DOI: https://doi.org/10.1175/1520-0442(2001)014%3C3433:EOMAAO%3E2.0.CO;2 (cit. on p. 10).

Trenberth, K. E. and D. J. Shea (1987). "On the evolution of the Southern Oscillation". In: *Monthly Weather Review* 115.12, pp. 3078–3096. DOI: https://doi.org/10.1175/1520-0493(1987)115<3078:OTEOTS>2.0.CO;2 (cit. on p. 2).

US Standard Atmosphere (1976). "National oceanic and atmospheric administration". In: *National Aeronautics and Space Administration, United States Air Force, Washington, DC* (cit. on p. 13).

Van Loon, H. and K. Labitzke (1987). "The Southern Oscillation. Part V: The anomalies in the lower stratosphere of the Northern Hemisphere in winter and a comparison with the quasi-biennial oscillation". In: *Monthly weather review* 115.2, pp. 357–369. DOI: https://doi.org/10.1175/1520-0493(1987)115%3C0357:TSOPVT%3E2.0.CO;2 (cit. on p. 96).

Vavrus, S. J. (2018). "The influence of Arctic amplification on mid-latitude weather and climate". In: *Current Climate Change Reports* 4.3, pp. 238–249. DOI: https://doi.org/10.1007/s40641-018-0105-2 (cit. on pp. 23, 86, 97).

Vihma, T. (2014). "Effects of Arctic sea ice decline on weather and climate: A review". In: *Surveys in Geophysics* 35.5, pp. 1175–1214. DOI: https://doi.org/10.1007/s10712-014-9284-0 (cit. on p. 97).

Vitart, F., A. W. Robertson, and D. L. T. Anderson (2012). "Subseasonal to Seasonal Prediction Project: Bridging the gap between weather and climate". In: *Bulletin of the World Meteorological Organization* 61.2, p. 23 (cit. on p. 93).

Von Storch, H. and F. W. Zwiers (2001). *Statistical analysis in climate research*. Cambridge university press (cit. on p. 34).

Warner, C. D. and M. E. McIntyre (1996). "On the propagation and dissipation of gravity wave spectra through a realistic middle atmosphere". In: *Journal of the atmospheric sciences* 53.22, pp. 3213–3235. DOI: https://doi.org/10.1175/1520-0469(1996)053<3213:OTPADO>2.0.CO;2 (cit. on p. 30).

Wegmann, M., Y. Orsolini, M. Vázquez, L. Gimeno, R. Nieto, et al. (2015). "Arctic moisture source for Eurasian snow cover variations in autumn". In: *Environmental Research Letters* 10.5, p. 054015. DOI: http://dx.doi.org/10.1088/1748-9326/10/5/054015 (cit. on pp. 24, 82).

Wendisch, M., M. Brückner, J. P. Burrows, S. Crewell, K. Dethloff, et al. (2017). "Understanding causes and effects of rapid warming in the Arctic". In: *Eos* 98. DOI: https://doi.org/10.1029/2017EO064803 (cit. on p. 23).

Wohltmann, I., R. Lehmann, and M. Rex (2017). "Update of the Polar SWIFT model for polar stratospheric ozone loss (Polar SWIFT version 2)". In: *Geoscientific Model Development* 10, pp. 2671–2689. DOI: https://doi.org/10.5194/gmd-10-2671-2017 (cit. on p. 89).

World Meteorological Organization (1975). *The Physical Basis of Climate and Climate Modelling: Report of the International Study Conference in Stockholm, 29 July-10 August 1974*. WMO (cit. on p. 1).

Yang, Y., R.-C. Ren, and M. Cai (2016). "Towards a physical understanding of stratospheric cooling under global warming through a process-based decomposition method". In: *Climate Dynamics* 47.12, pp. 3767–3782. DOI: https://doi.org/10.1007/s00382-016-3040-8 (cit. on p. 86).

Zängl, G., D. Reinert, P. Rípodas, and M. Baldauf (2015). "The ICON (ICOsahedral Non-hydrostatic) modelling framework of DWD and MPI-M: Description of the non-hydrostatic dynamical core". In: *Quarterly Journal of the Royal Meteorological Society* 141.687, pp. 563–579. DOI: https://doi.org/10.1002/qj.2378 (cit. on pp. 3, 25).

Appendix

A

A.1 Reconstructed second EOF patterns

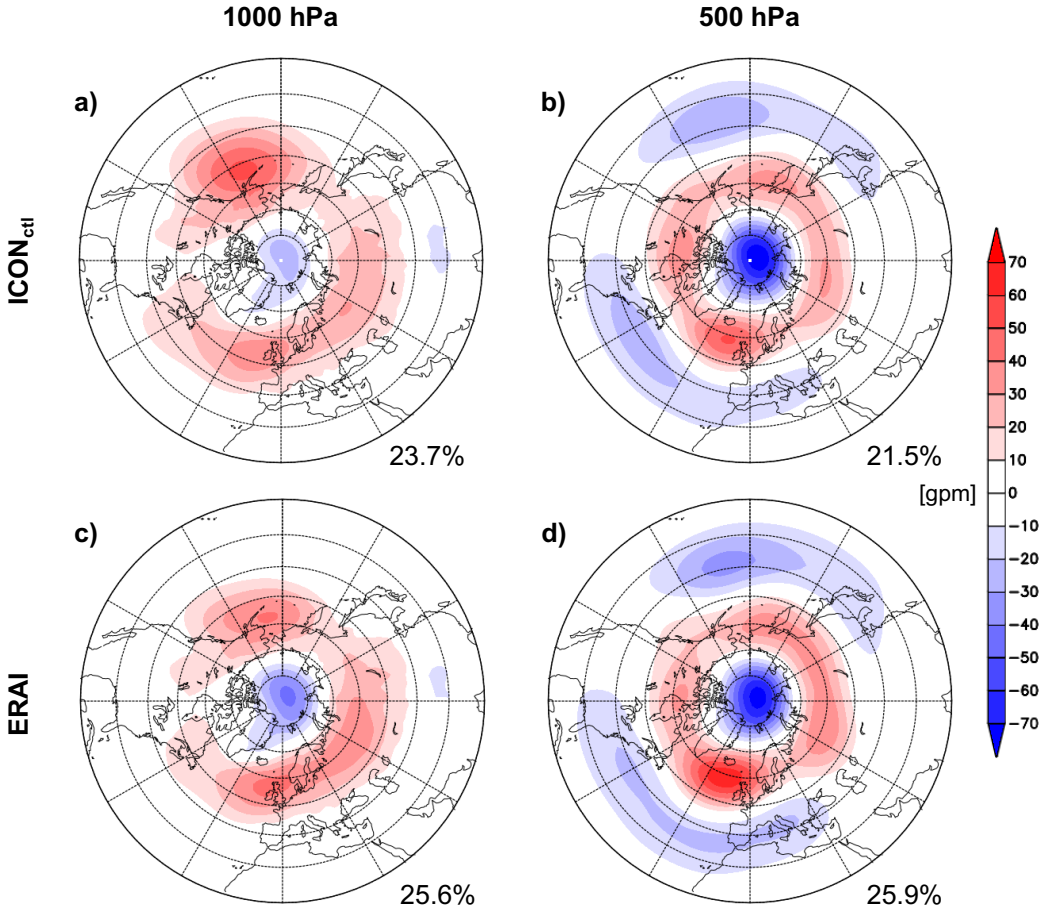

Fig. A.1.: Reconstructed second EOF patterns of daily zonally-averaged 1000 hPa (a,c) and 500 hPa (b,d) geopotential height during October-April 1979/80-2016/17 period on a polar stereographic projection showing values north of 20° N. Patterns of ICON$_{ctl}$ ensemble in a) and b), patterns of ERA-Interim reanalysis in c) and d). The explained variance is given in the bottom right corner of the respective figure.

A.2 Monthly RMSEs and MSWs

Tab. A.1.: Polar cap mean (65.25°N - 90°N) RMSE of mean sea level pressure and zonal wind in 10 hPa and amount of MSWs per decade. Numbers in brackets indicate the relative monthly occurrence in %. Total in the last column denotes the 9-month average RMSE and the total amount of MSWs per decade.

	Exp.	Sep.	Oct.	Nov.	Dec.	Jan.	Feb.	Mar	Apr.	May	Tot.
RMSE MSLP [hPa]	ctl	1.93	2.34	2.61	2.87	3.66	3.20	3.15	2.08	1.22	2.56
	nogwd-	1.99	2.07	2.83	3.22	3.20	3.27	2.70	2.10	1.17	2.50
	sso-	1.25	1.52	1.92	2.37	2.32	2.41	2.17	1.45	0.89	1.81
	gwd-	1.09	1.71	1.81	2.30	2.13	2.37	2.16	1.46	0.94	1.78
RMSE u10hPa [m/s]	ctl	0.60	3.60	2.24	4.55	10.91	5.39	2.82	1.31	1.22	3.63
	nogwd-	0.61	2.65	2.26	3.65	7.21	5.05	2.75	1.66	1.11	2.99
	sso-	0.59	3.10	3.06	4.28	8.65	4.10	2.15	1.93	1.13	3.23
	gwd-	0.68	2.42	2.06	3.76	6.73	4.87	3.32	1.60	1.04	2.94
MSWs/decade (rel. monthly occurrence in %)	ctl	-	-	0.16	1.63	4.00	1.84	1.21	-	-	8.84
		-	-	(2)	(18)	(45)	(21)	(14)	-	-	
	nogwd-	-	-	0.52	1.84	2.68	2.53	1.31	-	-	8.89
		-	-	(6)	(21)	(30)	(28)	(15)	-	-	
	sso-	-	-	0.63	1.10	3.37	2.05	2.21	-	-	8.26
		-	-	(8)	(13)	(41)	(25)	(13)	-	-	
	gwd-	-	-	0.68	1.84	3.37	2.21	1.00	-	-	9.11
		-	-	(8)	(20)	(37)	(24)	(11)	-	-	
	ERA-I.	-	-	-	1.05	1.58	2.10	0.79	-	-	5.53
		-	-	-	(19)	(29)	(38)	(14)	-	-	

A.3 MSLP effect of gravity wave drag parameterisations

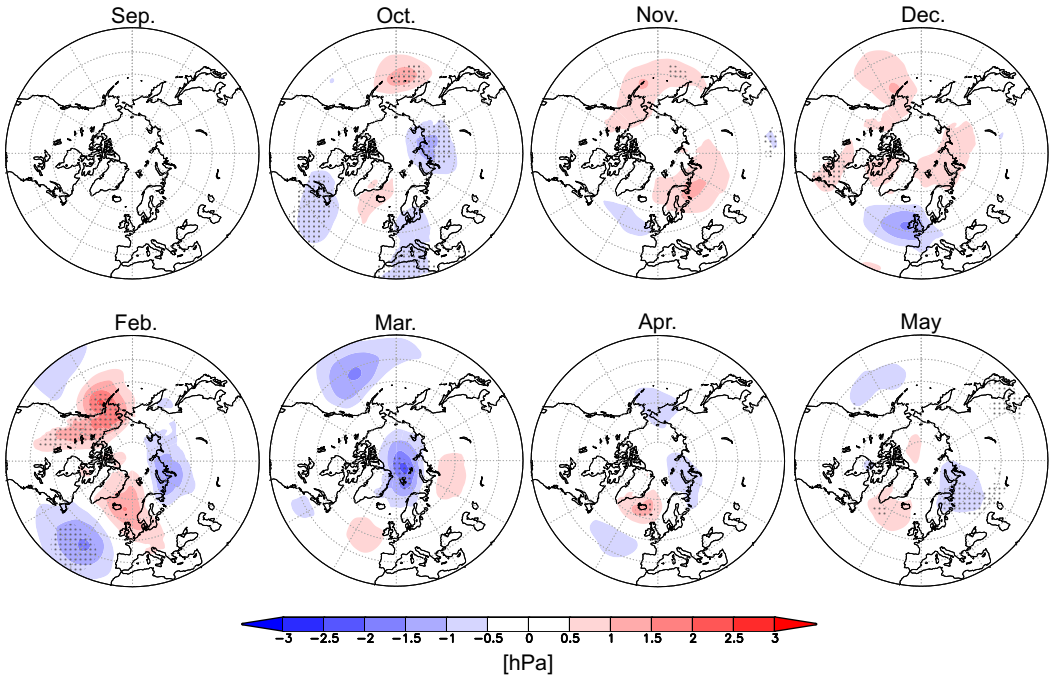

Fig. A.2.: Monthly mean MSLP difference between ICON$_{nogwd_}$ and ICON$_{ctl}$. Stippling indicates statistical significance at the 95% level according to a two-sided Wilcoxon-Mann-Whitney U-test. The January difference is given in Figure 4.21.

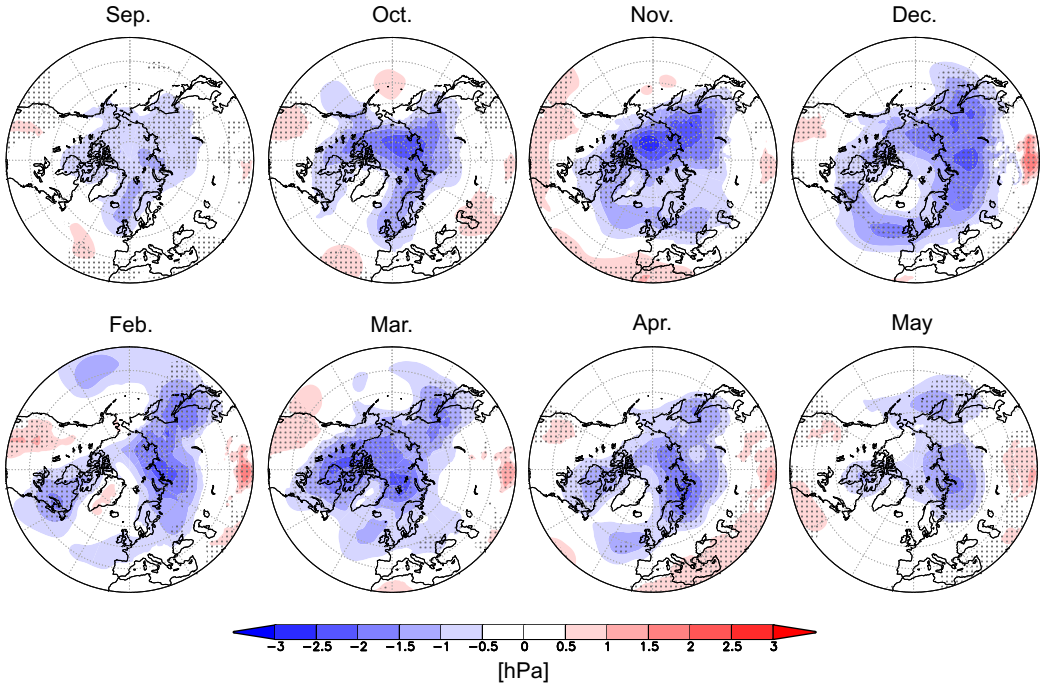

Fig. A.3.: Monthly mean MSLP difference between ICON$_{sso-}$ and ICON$_{ctl}$. Stippling indicates statistical significance at the 95% level according to a two-sided Wilcoxon-Mann-Whitney U-test. The January difference is given in Figure 4.21.

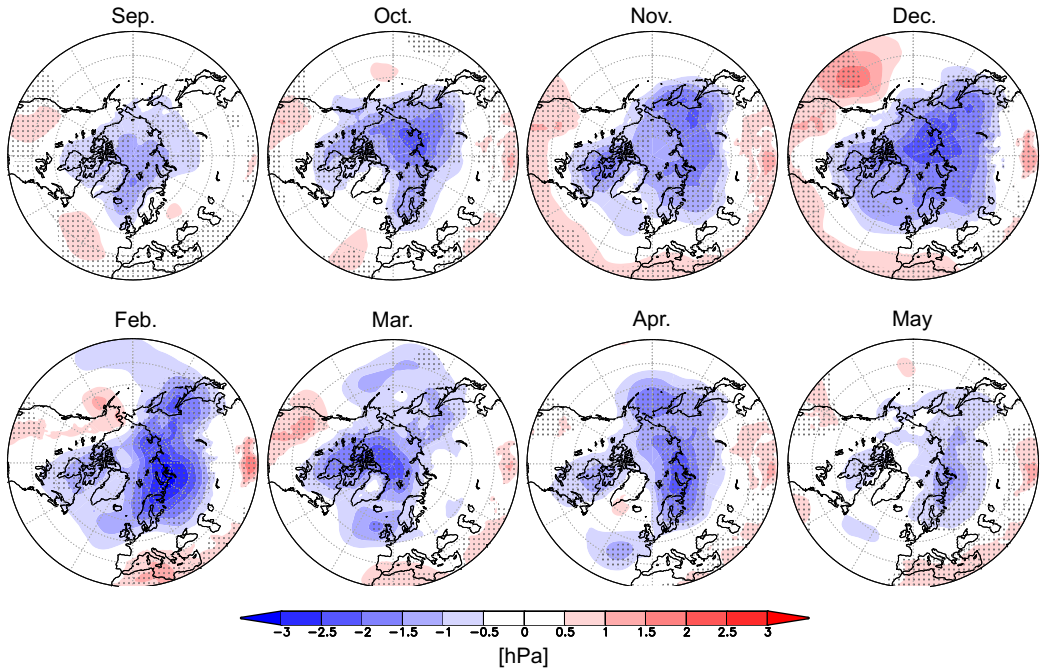

Fig. A.4.: Monthly mean MSLP difference between ICON$_{gwd-}$ and ICON$_{ctl}$. Stippling indicates statistical significance at the 95% level according to a two-sided Wilcoxon-Mann-Whitney U-test. The January difference is given in Figure 4.21.

A.4 QBO-E months

Tab. A.2.: Years that have been grouped into QBO-E phase according to the ERA-Interim equatorial zonal, monthly mean zonal wind in 50 hPa. the years are shown for the months November - March.

Nov.	Dec.	Jan.	Feb.	Mar.
1979	1979	1980	1980	1980
1981	1981	1982	1982	1982
1984	1984	1985	1985	1985
1989	1989	1990	1990	1990
1991	1991	1992	1997	1992
1992	1994	1997	1999	1997
1994	1996	1999	2002	1999
1996	1998	2002	2004	2004
1998	2001	2004	2006	2006
2001	2003	2006	2008	2008
2003	2005	2008	2013	2010
2005	2007	2013	2015	2013
2007	2012	2015		2015
2012	2014			
2014				

Acknowledgement

I am thankful to the Alfred Wegener Institute for funding me and giving me the opportunity to write this thesis. I am very grateful to Prof. Markus Rex for his supervision. A huge thank you goes to Dr. Dörthe Handorf and Dr. Ralf Jaiser. They never got tired of supervising me in the day-to-day business and this work would not have been possible without them. Furthermore, their support and correction remarks in the final phase of this PhD were greatly appreciated. I want to warmly thank Prof. Klaus Dethloff for all the very fruitful discussions in his office as well as his ongoing support. A big thank you goes to Sabine Erxleben for her technical support. I also wish to thank the whole section "atmospheric physics" for the good discussions and the welcome distraction during the seminars, lunch and coffee breaks as well as the after work activities. Katrin Müller was a great help in the final phase of this thesis, her correction remarks are on point and she never stopped encouraging me. Thank you! I also want to thank Dr. Marion Maturilli for giving me the great opportunity to work in Ny-Ålesund. I am moreover grateful to Dr. Günther Zängl and his colleagues from the DWD for the welcome advise on the setup of the ICON simulations. I gratefully acknowledge the support by the project POLEX funded by Helmholtz Association of German Research Centers (grant number: HRSF-0036).

Furthermore, I want to thank my family for supporting me throughout the whole time. Special thanks goes to my mother for her advise concerning the English language. I am very grateful to all my friends for being there for me when I needed distraction and cheering up, in particular I want to thank Sonja, Emil, Kerstin and Sina. Special thoughts go to my late brother Max.

Erklärung

Die vorliegende Arbeit wurde an keiner anderen Hochschule eingereicht. Sie wurde selbständig und ausschließlich mit den angegebenen Mitteln angefertigt.

Potsdam, den 19. August 2020

Raphael H. Köhler